SIMULATING STRESS DRIVEN STRUCTURAL EVOLUTION IN SOLID

by

ZHEN LIU

A dissertation submitted to the Graduate Faculty in Engineering in partial fulfillment of the requirements for the degree of Doctor of Philosophy, The City University of New York

2009 (year degree awarded)

This manuscript has been read and accepted for the
Graduate Faculty in Engineering in satisfaction of the
dissertation requirement for the degree of Doctor of Philosophy.

	Honghui Yu
Date	Chair of Examining Committee [**required signature**]
	Mumtaz K. Kassir
Date	Executive Officer [**required signature]**

[typed name] Benjamin Liaw

[typed name] Jackie Jie Li

[typed name] Robert V. Kukta

[typed name] Feridun Delale
Supervision Committee

THE CITY UNIVERSITY OF NEW YORK

Abstract

SIMULATING STRESS DRIVEN STRUCTURAL EVOLUTION IN SOLID

by

Zhen Liu

Adviser: Professor Honghui Yu

In this dissertation, a variational approach, which can incorporate a wide range of thermodynamic forces and mass transport mechanisms, has been applied to study stress induced structural evolution. The approach combines driving forces, kinetic laws and the free energy variations associated with virtual structural change. A program with an embedded stress field solver, using Boundary Element Method (BEM), is developed. By using the program developed, thin film morphology evolution in elastically stressed solid due to surface diffusion and/or evaporation/condensation is simulated first. The similarity and difference between surface diffusion and evaporation-condensation induced surface grooving and the effect of the mobility ratio of two processes are explored. Special attention is paid on the effect of the initial profile of the surface. Simulations show that if the initial surface contains many sharp cracks or notches, the surface may take longer time to develop deep cusps and break into islands than the relatively flatter initial surfaces. In the second part of this work, stress relaxation due to grain boundary diffusion is considered. A set of stress relaxation processes are simulated under different surface and grain boundary energy ratio to explore the effect of surface profile on stress relaxation. It is found that when the stress relaxation is limited by the rate of surface diffusion, the dihedral angle

at the surface-grain boundary junction plays a significant role. In addition, the simulation result on stress relaxation process that is limited by grain boundary diffusion is used to determine the grain boundary diffusivity by being compared with the experimental results. Finally, the numerical scheme is extended to 3D axi-symmetric model to study the evolution of a cylinder under stress by surface diffusion. Under a periodic perturbation, it is found that the stressed fiber is not always stable even its perturbation wavelength is smaller than its circumference. It can still stay stable, or develop grooves first then approach to a steady state shape, or develop cusps and break into particles. These two critical stresses that are corresponding to initial stability and the transition from steady state to unstable state are estimated by using numerical simulation.

Acknowledgement

I would like to take this opportunity to express my acknowledgement to the people that have supported me, in many forms, during my life at CUNY.

First and foremost, I would like to say thank you to my advisor, Professor Honghui Yu, a fantastic mentor and friend, for his guidance, encouragement, patience and inspiration. Without your help, both in study and in life, I could not have had that much achievement. It's my pleasure to have the other members in my dissertation committee, Professor Feridun Delale, Professor Jackie Li, Professor Benjamin Liaw and Professor Robert V. Kukta (Stone Brook University), who provided me very helpful and valuable suggestions. In addition, I would express my gratitude to Professor Rui Huang (University of Texas, Austin), who provided experimental data and useful comments.

Thanks my colleagues, Ercan Sevkat, Ping Zhao, Yang Cao, Kai Gu, Huapei Wan, Mazen Diab, Peng Sun. Their thoughtful comments and good cheer have been greatly appreciated. Also, my thanks are extended to faculty members in University of Science and technology of China (USTC). Special thanks to Professor Zhihua Feng and Fanrang Kong.

I would thank all my family, especially my parents and parents-in-law, for their never-ending love, encouragement and support. I would thank my friends, Wei Liu, Bo Song, Chunlei Chen, Sanyuan Li, Hanxiang He, Chunyang Zheng, Deqiang Chen, Song Zhang. You always relax and refresh me in this long journey.

Thanks also go to my two little, Alan and Jerry. You are making my life more and more brilliant and amazing. Last but certainly not least, I would express my special thanks to my unique Zhen He for her affection, inspiration, and support throughout my life.

Table of Contents

Lists of Figures

Chapter 1

1 Introduction

1.1 Background and Previous works

1.1.1 Structural Evolution in Solid

In recently years, there is a growing interest in micro-structural evolution of solid caused by mass transport mechanisms, mainly driven by the development in micro- and nano-technologies. Since in a small device, a little change of structure can greatly influence its mechanical and/or electrical performance and reliability, it is therefore necessary to understand, and be able to model, these processes at an appropriate level of sophistication. For a bulk material, an overall knowledge of the structure, such as the grain size distribution and pore volume fraction, is often adequate. For a film or a line, where the grain size is comparable to the film thickness and line width, an overall knowledge of structure is inadequate; for example, in sub-micro aluminum interconnects, the electro-migration damage relates to structural detail [1].

Why does the structure evolve? In non-equilibrium structure, the solid evolves to reduce the total free energy of the system, which may include surface tension, grain boundary tension, chemical energy, elastic energy and electrostatic energy etc. How does the structure evolve? In solid, there are many different kinetic processes to reduce the total free energy in the system, including diffusion, creep, dislocation and reaction etc. Thus, it is the combination of *thermodynamics* and *kinetics* that determines the path and the final state in solid. For example,

as shown in Figure 1-1 [11], when a polycrystalline fiber is heated for some time, grains change shape and may evolve to one of two equilibrium configurations: isolated spheres or truncated spheres that remain connected. Figure 1-2 illustrates the morphological change of a zirconia fiber made by Miller and Lange [2].

To which configuration do the grains evolve? How long does this evolution take? It will be determined by both thermodynamic and kinetics. Among all the methodologies to model these processes, including, molecular dynamics [3-5], phase field method [6-9], and continuum based model [10-12], the last one has the advantage of reaching practical engineering size a relatively small computational cost.

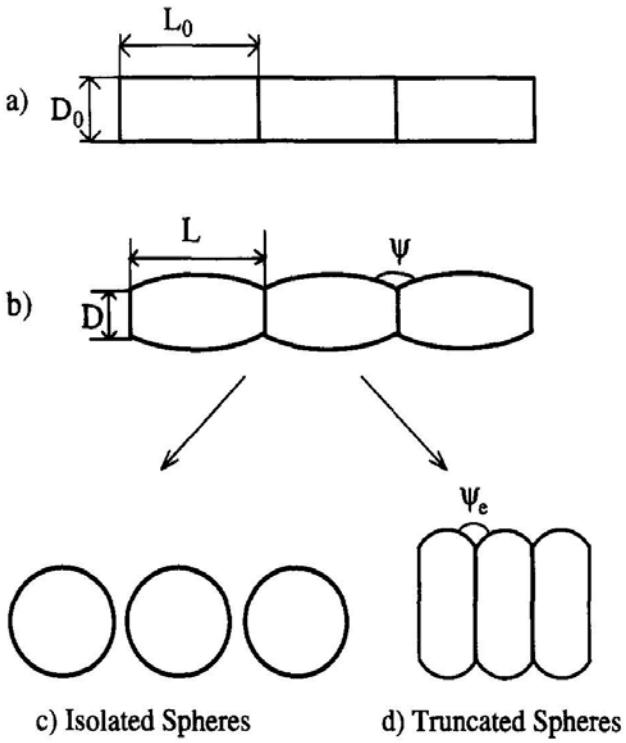

Figure 1-1: (a) The initial array of cylinder-shaped grains. (b) An array of barrel-shaped grains approximates an intermediate, nonequilibrium state. (c) Grains pinch off and spheroidize, approaching an equilibrium state, a row of isolated spheres. (d) The array shrinks as atoms diffuse out from the grain boundaries and plate onto the free surfaces, approaching another equilibrium state, a touching array of truncated spheres. Suo [11].

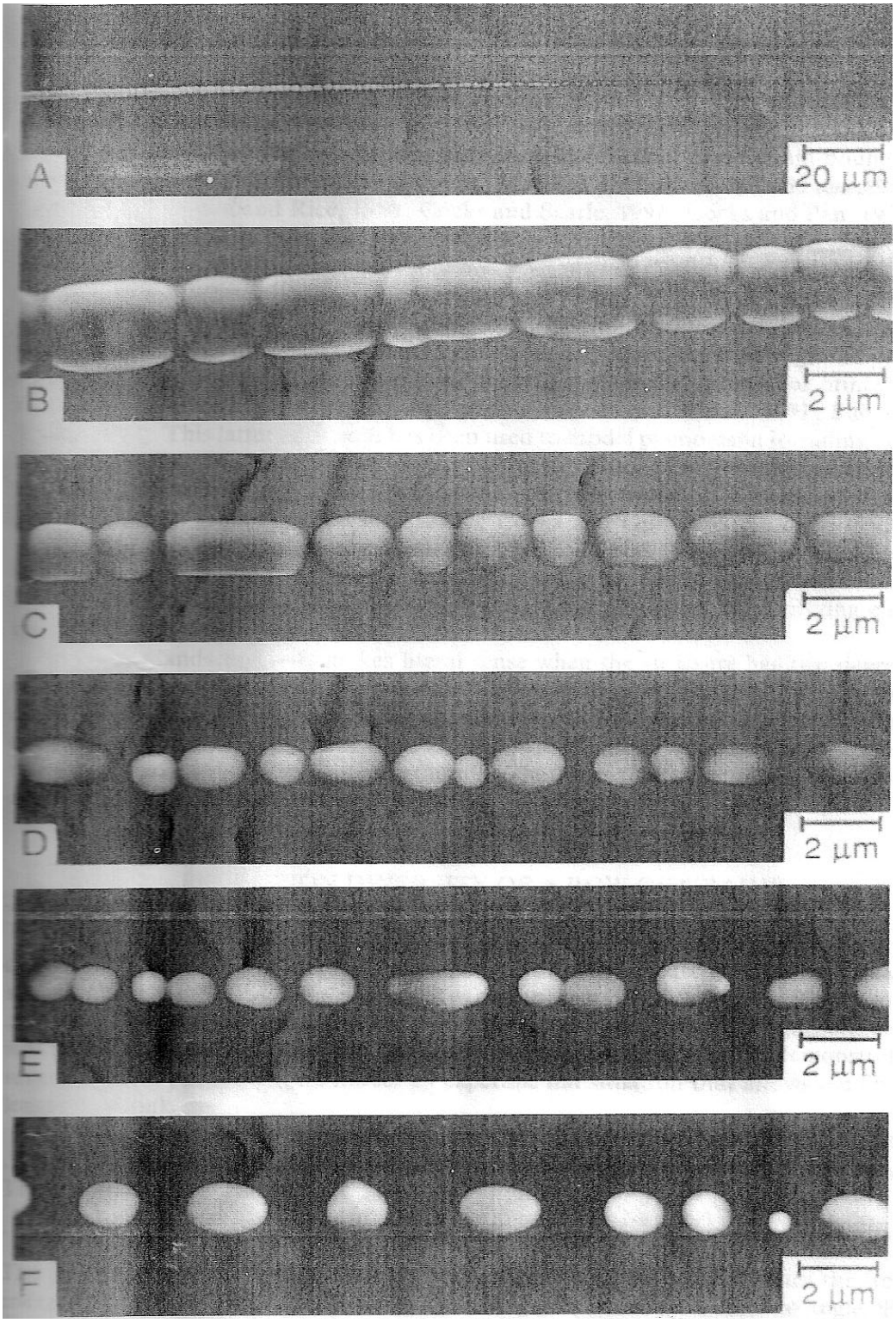

Figure 1-2: A fiber, drawn from a solution, was placed on a sapphire plate and heated for some time. (A) The fiber diameter is large at one end and small at the other. (B, C) Grains with large diameters remain connected. (D, E, F) Grains with small diameters break into particles. Miller and Lange [2]

Most models of capillarity-driven solid-state processes originate from the work of Herring [13]. For a wide range of applications, a macroscopically non-equilibrium structure may be divided into elements, each being in an equilibrium state. The free energy of an element is a function of the local state variables such as composition, temperature and stress. The total free energy of the structure is summed over all the elements. Herring defined the chemical potential of an element as the increase of the total free energy associated with the addition of one atom to the element. For the non-equilibrium structure, the chemical potential differs from one element to another. Herring assumed that the chemical potential gradient drives mass flux according to an empirical kinetic law. Together with mass conservation, such ideas lead to partial differential equations, quite analogous to the heat transfer problem.

An alternative, global view regards evolution as a means to release the total free energy. The global analysis of this kind of problem has been described by Sun et al. [14]. A non-equilibrium structure is described, often approximately, with a set of generalized coordinates. For a structure described with one degree of freedom, the free energy is a function of the generalized coordinate, represented by a curve in a plane spanned by the free energy and the coordinate. A minimum free energy point on the curve represents an equilibrium state. Thermodynamics requires that the state of the non-equilibrium structure descends on the curve toward equilibrium. Consequently, thermodynamics alone determines both the evolution path and the final state. Kinetics is restricted to the role of determining the rate of travel along the path toward the equilibrium state.

The variational principle is a global version of Herring's non-equilibrium thermodynamics. Such variational principles have been used in modeling diverse non-equilibrium phenomena in materials. Again, the free energy may include interfacial, elastic, electrostatic, and chemical energy. The rate processes may include diffusion, creep, grain-boundary motion, and surface or

interface reactions. Material phenomena include creep void growth [15-17], creep crack growth [18, 19], super-plasticity [20], interface diffusion in composites [21] and solid-state sintering [22, 23]. These authors formulated the variational principles by assembling local quantities such as chemical potentials and relating these to the boundary conditions through the principle of virtual power. Alternatively, one may formulate the variational principles from a global definition of the driving forces [24, 25]. This latter approach has been used to model phenomena including void shape instability [26], dislocation climb [27], wrinkling of oxide scales on high temperature alloys [28], ferroelectric domain evolution [29], grain growth [30, 31], and solid-state sintering [32]. Bower and Freund [33] have formulated a general class of variational principles for analyzing electro-migration in deformable solids.

A finite element method (FEM), based on this variational approach, for motions of microscopic surfaces of thin film, driven by multiple energetic forces, via concomitant rate processes, has been developed [34]. In the work, such a method for interface migration driven by interface tension and chemical energy difference between phases has been presented. A widely used kinetic law: the velocity of the interface is proportional to the driving pressure (i.e. the free energy reduction associated with the interface moving per unit distance) has been adopted. The method has been extended by including mass diffusion [35]. The computer program can simulate grain boundary migration, solid surface motion via evaporation-condensation surface diffusion, and their combination. The method can be viewed as a numerical implementation of a classical theory discussed by Herring [13]. The theory assumes that the free energy of the system is the surface energy summed over all surface and grain boundary areas. To reduce this free energy, the solid changes shape by mass diffusion on the interface. This global energetic statement, however, is insufficient to determine the shape history,

because infinitely many shape histories would each reduce the free energy. To complete the theory, Herring defined a driving force by the amount of free energy decrease associated with per unit volume of matter moving per unit distance on the interface. This definition prescribes a local quantity, the driving force, at every point on the solid surface. He then assumed a kinetic law that, at every point on the surface, the mass flux is proportional to the driving force. The formal procedure, incidentally, follows that of irreversible thermodynamics [36]. Other forms of energy (e.g. elastic energy, work done by an external force) can be readily added to the free energy.

1.1.2 Stressed Thin Solid Film

One of the most common cracks in thin film is due to the residual stress. Figure 1-3 [37]

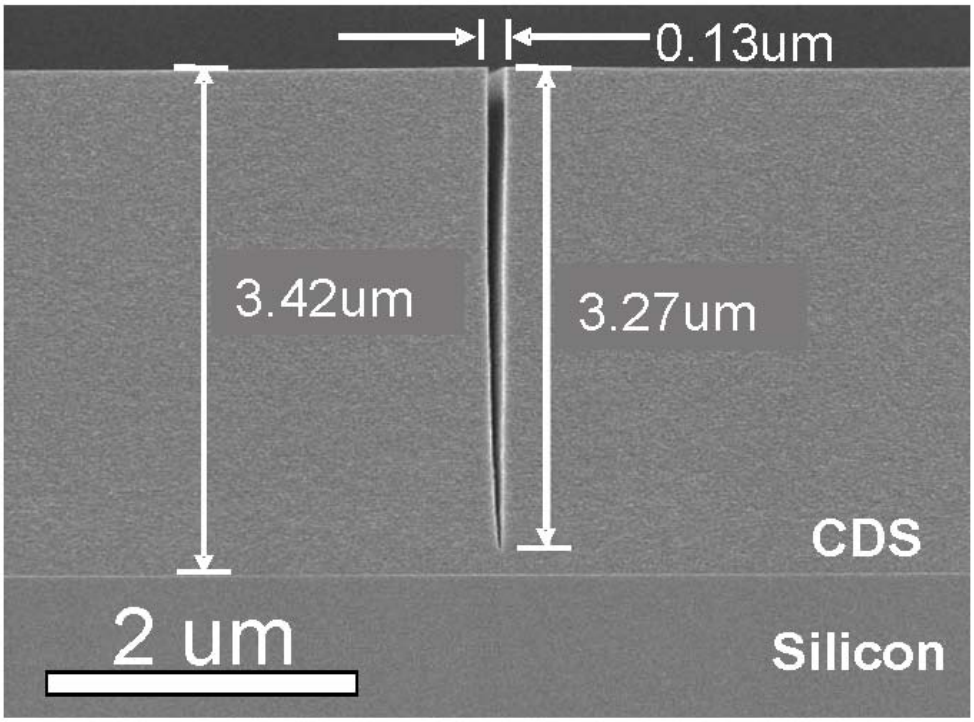

Figure 1-3: The typical scanning cross-section electron micrograph of a carbon-doped-silicate (CDS) channel crack due to the tensile residual stress. Tsui [37]

show the typical scanning electron micrograph of a channel crack due to the tensile residual stress in carbon-doped-silicate (CDS). Thin film is usually under large residual stress. The stress is mainly generated by its growth process or lattice mismatch between thin film and its substrate and has a key effect on the properties, morphology and behavior of the thin film. A surface under stress is unstable if mass can be exchanged and transported along the surface. Asaro and Tiller [38] and others [39-44] showed theoretically that a flat surface under a stress can evolve to a wavy shape by surface diffusion. The phenomenon of surface roughening has been observed in a growing number of experiments [45-47]. Some other experiments involving controlled annealing have been used to test the characteristic length and time scales, as well as other features predicted in the theoretical models [48-51] further showed that the wavy surface can evolve to form a sharp crack front. The process was observed by Jesson *et al.* on a surface of a strained epitaxial film [52].

A surface can also change its morphology by surface reaction, either by deposition or erosion. Srolovitz [40] showed that a stressed surface is unstable due to evaporation-condensation. Hillig and Charles [53] studied the crack nucleation from an elliptical notch due to stress-dependant surface reaction. By using a linear kinetic law, the crack nucleation process for polycrystalline materials, in which grain boundaries cause surfaces to form grooves and further nucleate crack has been simulated [54]. The stability of a solid surface under small and/or large perturbations has been studied by adopting a nonlinear kinetic law in which the mobility depends on the applied stress [55, 56]. The evolution and crack nucleation from a smooth notch on a stressed solid surface has been studied also [57]. Kukta and Kouris [58] modeled and studied strained epitaxial deposits (islands) grown on a substrate and found that the resulting morphology depends largely on the rate of deposition relative to surface mobility. Besides surface diffusion

and reaction, many other mechanisms such as cracking and/or delamination [59-62], dislocation [63, 64] and diffusional creeps [65-68] can be involved in structural evolution and stress relaxation process of thin film.

Since stress can significantly affect surface evolution, studying and then trying to control the stress become a more important technology challenge recently. In this dissertation, a numerical approach based on the variational principle mentioned above has been developed to study the effects of mobilities and initial profile on stressed thin film morphology evolution due to surface diffusion and evaporation/condensation [69]. For problems with evolving boundary, one big challenge in solving stress field by using FEM is mesh regeneration and refinement, especially in problems involving singular point such as crack tip [70]. Since computational time is always an issue in the simulation of micro-structure evolution, in this work, Boundary Element Method (BEM) is used to solve stress field. BEM only requires discretization of surface instead of volume, thus it has fewer degrees of freedom at the same degrees of accuracy. Elements in BEM can be easily generated and adjusted when surface profile changes, costing much less computation time for re-meshing than in FEM. Another advantage of BEM over FEM is when analyzing problems with stress concentrations. BEM can easily and accurately deal with the problems involving formation of crack or cusp at much less computational cost than FEM.

Another issue in thin solid film is stress relaxation. Many studies have been done on the stress relaxation of the thin film with free surface. A model coupling surface diffusion and steady-state grain boundary diffusion had been developed by Thouless [68,70,71] for polycrystalline thin film. He made an assumption that thin film can slide freely on its substrate. This assumption induces that the diffusion flux is taken as a linear function of position along grain boundary. Genin *et al*. [72-74] studied the effect of grain boundary grooving and surface

evolution under the same assumption. Gao and his collaborators [75] developed a crack-like grain boundary diffusion wedges model in which no sliding and diffusion are allowed at the film/substrate interface and surface diffusion and grain-boundary grooving are neglected (Figure 1-4). Zhang and Gao [76] then relaxed some restrictions in [75] to study coupled grain-boundary and surface diffusion but still neglected the effect of surface slope on the normal stress and chemical potential along the grain boundary. Huang *et al.* [77] developed a kinetic model for stress relaxation in unpassivated and passivated thin films based on coupling of grain-boundary diffusion with surface and interface diffusion, respectively. For unpassivated thin films, the model differs from Thouless's model [71] in that the transient behavior of grain-boundary diffusion is explicitly considered, and differs from Gao *et al.* [75, 76] in that an approximation was made in calculating the normal stress at the grain boundary. And they compared the model with their experimental results [78]. Several other experiments [79, 80] observed the coupling of interface diffusion and grain boundary diffusion as a stress relaxation mechanism in passivated Cu film.

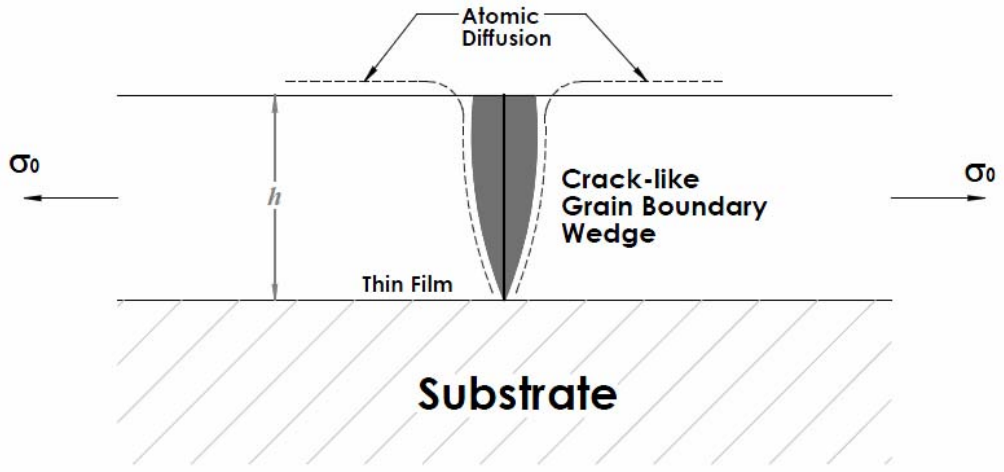

Figure 1-4: The geometry of a crack-like grain-boundary wedge of a thin film.

Although some of these works have grain boundary groove, all of them did not consider the effect of surface profile on the normal stress along grain boundary. This point is taken account in this dissertation [81]. The schematics is the similar as [69], another mass transport mechanism, grain boundary diffusion, is included in the morphology evolution and stress relaxation processes.

1.1.3 Surface Evolution of Fiber

A fiber can change its shape by surface diffusion. Under external perturbation, it may become unstable and break into particles fiber. Figure 1-5 [124] illustrates a fiber reinforcements with a wire-like morphology features becomes unstable with respect to surface energy. The reason is same as the Rayleigh Instability for fluid—to minimize the total surface energy. Mullins and Nichols [82, 83] obtained same threshold condition for solid cylinder rods under annealing: to minimize the surface energy, a small perturbation may grow and break the cylinder when the perturbation wavelength λ is greater than the cylinder circumference $2\pi R$,

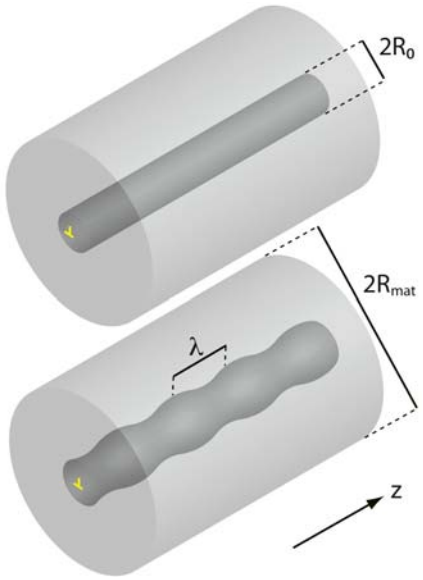

Figure 1-5: A fiber reinforcements with a wire-like morphology features becomes unstable with respect to surface energy [124]

where R is the radius of the unperturbed. They also got the similar result for cylinder voids in solids [84]. The spheroidization by surface diffusion of a solid rod or pore channel of circular cross-section is of particular interest because of the relationship between high temperature stability and reinforcing phases of cylindrical shape, and it has been studied extensively [85-87 and more]. Most of these linear theoretical analyses of surface evolution with small perturbations obtained that the critical perturbation wavelength $\lambda_m = 2\sqrt{2}\pi R$ which gives the maximum groove growth rate when the dominant mechanism is surface diffusion. However, some experimental observations [87-89] showed that the observed average wavelength at which spheroidization occurs doesn't correspond to λ_m when the perturbation had large amplitude. These observations indicated that it is difficult to predict instability in the nonlinear regime from the linear analyses. Choy et al [90] performed a non-linear analysis by using finite difference method to investigate the role of initial conditions where the wavelength and amplitude vary with position. Yu and Suo [91] set up an axi-symmetric model to study the transient separation process of pore-grain boundary by using finite element method based on a weak statement.

When a fiber is stressed, it becomes more unstable. Instabilities exist even the wavelength of the fiber is smaller than the circumference to relax the elastic energy. Colin et al [92, 93] introduced a linear analysis of the morphology instabilities of stressed pore channel. Their calculations showed that the critical wavelength of stressed cylinder is shifted toward shorter values as the stress increases. Similar study had been performed on stressed, solid cylinder whisker by Kirill *et al* [94]. They found that the presence of elastic strains can excite non-axisymmetric modes, which, under certain conditions, are preferred and can give rise to helical surfaces. In these works, the dominant mechanism of morphological evolution is focused on

surface diffusion. Besides, Colin [95] introduced another linear instability analysis, volume diffusion approach, on stressed solid cylinder in a matrix.

To study the non-linear evolution process of cylinder solid with large amplitude perturbation under stress, a numerical scheme is set up to simulate the morphology evolution of stressed fiber and focus on mass transport process on axi-symmetric surface.

1.2 Summary of Dissertation Research

In this dissertation, a variational approach, which incorporates a wide range of thermodynamic forces and mass transport mechanisms, has been applied to study stress induced structural evolution. The heart of the approach is a variational principle that defines various thermodynamic driving forces using an integral form. On one hand, it can reproduce the differential equations of Herring [13] and Mullin [82]; and on the other hand, it forms the basis for Finite Element Method (FEM), which does not require the calculation of surface curvature and chemical potential. The method has much weaker requirement on the smoothness of surface and thus it is applicable to surfaces with any shape and/or surface energy anisotropy. The elastic stress field is solved by using Boundary Element Method (BEM) which only requires discretization of surface instead of volume, thus it has fewer degrees of freedom at the same degrees of accuracy. And it makes refine and re-mesh processes much easier when the surface profile changes by mass transportation. These advantages can save much computation times comparing to using FEM to solve the stress field.

On the basis of the numerical scheme, a computer program has been created to study the effects of mobilities and initial profile on stressed thin film morphology evolution due to surface diffusion and evaporation/condensation [69]. A well-known problem, the surface instability and

morphology evolution of a residually stressed thin film is simulated to verify the program code firstly. The similarity and difference between the surface grooves induced by surface diffusion and evaporation/condensation, the effect of the mobility ratio of two processes when they are concurrent, and the dependence of surface kinetic pathway on its initial profile then are studied. .It is found that the grooves induced by surface diffusion and evaporation/condensation have different surface features: when two processes are concurrent but surface diffusion process is dominant, increasing the mobility of evaporation/condensation increases the time and groove depth needed to form surface cusps; an initially cracked surface could approach a flat surface first, then after a long slowly evolving period, it gradually develops sharp tips on the surface again. Simulations show that excessive surface area, due to small cracks, notches or other surface defects, could significantly delay the development of surface instability. By simply adding a term, grain-boundary diffusion into the previous scheme, another two dimensional case, stress relaxation of thin film due to coupled surface and grain-boundary diffusion, has been studied [81]. Different from the previously published works, this study also explores the effects of mobility ratio of the two processes and the dihedral angle at the surface-grain boundary triple junction. The ranges of mobility ratio, in which the stress relaxation process is limited by either surface diffusion or grain boundary diffusion, are determined. It is found that, when the stress relaxation is limited by the rate of surface diffusion, the dihedral angle at the surface-grain boundary junction plays a significant role. A scheme of applying the simulation results to determine material constants is also presented. As an example, the activation energy and diffusivity of grain boundary diffusion in Cu are obtained by comparing the numerical simulation with a set of published experimental data. The third part of our work is to extend the numerical scheme further more to an axisymmetric three dimensional case to study the

microstructure evolution of stressed fiber due to surface diffusion [96]. The corresponding BEM which is used to solve the stress field is also adopted the axisymmetric model. From the simulating results, it is found that, under a periodic perturbation, the stressed fiber is not always stable even its perturbation wavelength is smaller than its circumference (Rayleigh instability). It can still stay stable, or develop grooves then approach to a steady state shape, or develop cusps and break into particles. Our simulation will roughly obtain these two stress threshold conditions corresponding to different fiber wavelengths.

1.3 Thesis Outline

In the next chapter the global view of structural evolution in solid, the weak statement, will be reviewed and formulated. Then the numerical scheme including FEM, based on the variational principle, and some details of BEM, used to calculate stress field, will be introduced. In Chapter 3, the morphology evolution of a residually stressed thin film is simulated. In this simulation, two mass transportation mechanisms, surface diffusion and evaporation-condensation, are considered and the dependence of surface kinetic pathway on its initial profile is discussed. Afterwards, the stress relaxation of thin film due to coupled surface and grain-boundary diffusion is studied and simulated. This study focus on the effects of surface profile on stress relaxation by comparing the results of simulations under different surface-grain-boundary energy ratio and fit the experimental results by the simulation results and determine the surface and grain boundary diffusivities. Finally, simulation of microstructure evolution of stressed fiber due to surface diffusion is presented in Chapter 5. Two stress thresholds corresponding to different fiber wavelengths.of surface evolution are roughly obtained.

Chapter 2

2 Formulation of Weak Statement

Imagine two concomitant processes on a solid surface: the solid matter can relocate on the surface by diffusion, and exchange with the surrounding vapor by evaporation-condensation. This chapter summarizes Suo's work [11] to formulate weak statement of these two processes, respectively, and then combine them together.

2.1 Formulation of Evaporation-Condensation

Considere a solid particle in contact with its vapor, atoms either condense from the vapor, or evaporate from the solid, both causing the interface (the surface of the solid) to move. Imagine a situation in which atoms diffuse rapidly in the vapor, but react slowly on the interface, so that the vapor maintains a uniform chemical potential (composition and pressure, etc.). Assume the amount of vapor is very large compared to the mass exchange due to evaporation and condensation so that the vapor keeps its chemical potential constant at all times.

2.1.1 Free Energy, Virtual Motion and Kinetic Law

Assume total free energy of the solid is G. In different cases, free energy can include different terms, such as surface energy, grain boundary energy, strain energy, chemical potential difference between atoms in solid and in vapor, electric energy etc.. First, let's only include

surface tension (i.e. the free energy per area of the interface), which may depend on crystalline orientation, and the difference in the free energy density of two phase (i.e. the free energy increase associated with the condensation of unit volume of the solid). More terms of free energy will be specified when certain cases are discussed later. Let γ be the surface tension and g the fee energy density difference. The introduction of the solid particle into the vapor changes the free energy of the entire system by

$$G = \int \gamma dA + gV \tag{2.1}$$

where A is the interface area, V the volume of the solid particle. Since the assumption that the particle is immersed in a large mass of the vapor is adopted, g keeps constant as the reaction proceeds.

Thermodynamics requires that the surface evolve to decrease the free energy. The surface tension is positive and therefore strives to decrease the surface area. When the solid surface is concave, such as a dent on a flat surface, γ tends to condensation. When the solid surface is convex, such as a hillock on the surface, γ favors vaporization. The free energy density difference between two phases, g, can be either positive or negative. When $g > 0$, it favors vaporization and reduces the particle volume. When $g < 0$, it favors condensation and increases the particle volume. Generally, both γ and g affect surface motion. However, infinitely many ways of surface motion can decrease the free energy. To determine the actual surface motion, kinetic processes must be specified.

Figure 2-1 illustrates a single crystal particle immersed in a large mass of vapor phase and the motion of the interface by mass exchange between the solid and vapor. The solid-vapor interface is the closed surface in three-dimensions. Imagine that the interface undergoes a virtual motion: interface moves in its normal direction as atoms are added to, or removed from, the solid;

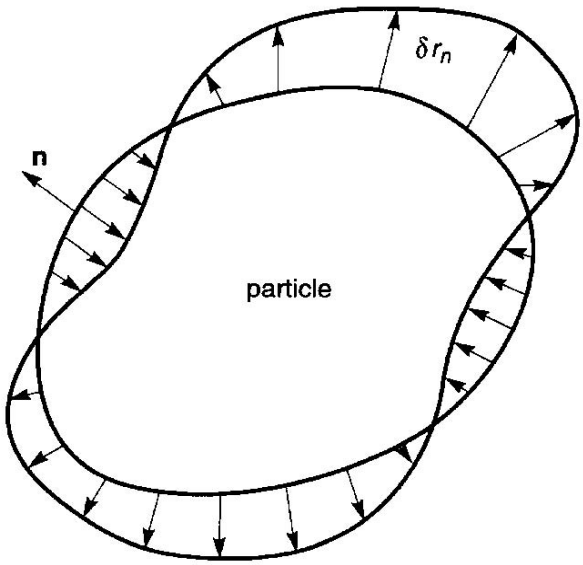

Figure 2-1: A single particle is immersed in a large mass of a vapor. The interface undergoes a distribution of virtual motion. The magnitude of the motion, δr_n, should be infinitesimal and may vary over the interface. Suo [11]

this small movement doesn't need to obey any kinetic law; and the amount of the motion, which is represented by the magnitude of the interface displacement, δr_n, is infinitesimal and varies arbitrarily on the interface. Associated with the virtual motion, the total free energy of the system varies by δG. Define a thermodynamic force, p, as the free energy reduction associated with a unit volume of matter deposited to the solid surface from the vapor, namely,

$$\int p \delta r_n dA = -\delta G \tag{2.2}$$

The integral extends over the interface area. The thermodynamic force, p, has a unit of pressure (force/area or energy/volume), and has been called driving pressure and/or driving stress. Although the explicit expressions for p are unnecessary in this approach, it will be simply listed for completeness and comparison.

A linear kinetic law will be adopted. Let v_n be the actual velocity of the interface in the direction normal to the interface (i.e., the volume of atoms added to the particle per area per time). When a structure is not far from equilibrium, namely, when the free energy reduction per atom crossing an interface is small compared with the average thermal energy per atom, the actual velocity, v_n, is proportional to the driving pressure, p [82,97,98]. Namely,

$$v_n = mp \tag{2.3}$$

where m is the mobility of the interface. In this case, atoms in the two phases exchange at the interface by evaporation and condensation, Mullins [14] showed that $m = p_0\Omega^2(2\pi M)^{-1/2}(KT)^{-3/2}$, where p_0 is the vapor pressure in equilibrium with the flat solid surface, Ω the atomic volume, M the mass per atom, k Boltzmann's constant and T the absolute temperature. Nonlinear kinetic relation has been presented by Loge and Suo [31].

2.1.2 Differential Equations

The differential equations of the surface motion listed here are followed by Ref. [11]. The following assumptions need to be adopted in this approach: the surface tension is isotropic and consequently the solid-vapor interface is smooth in three dimensions at a given time. In three dimensions, a surface has two principal curvatures, which are taken to be positive for a convex surface and negative for a concave surface. Denote the radii of these two curvatures R_1 and R_2. Namely, the sum of the principal curvatures is

$$K = \frac{1}{R_1} + \frac{1}{R_2} \tag{2.4}$$

Associated with the virtual motion, δr_n, the interface area varies by

$$\delta A = \int K \delta r_n dA \tag{2.5}$$

And the particle volume varies by

$$\delta V = \int \delta r_n dA \tag{2.6}$$

The integrals extend over the interface area.

When the surface tension is isotropic, the free energy in equation (2.1) becomes $G = \gamma A + gV$. Associated with the virtual motion of the surface, the free energy varies by

$$\delta G = \gamma \delta A + g\delta V \tag{2.7}$$

Replace p and p by using equations (2.5) and (2.6), giving

$$\delta G = \int (\gamma K + g)\delta r_n dA \tag{2.8}$$

Now, compare two equations (2.2) and (2.8), giving

$$p = -\gamma K - g \tag{2.9}$$

This equation expresses the driving pressure in terms of the geometric parameter, K, and the energetic quantities, γ and g. Combine the equations (2.3) and (2.9) together, leading

$$v_n = -m(\gamma K + g) \tag{2.10}$$

This partial differential equation governs the interface motion.

Herring [13] derived expressions of p when the surface tension is anisotropic and the interface forms facets.

2.1.3 Weak Statement for Evaporation-Condensation

Energetics and kinetic law together define the dynamics of surface motion. At a given time, the change of free energy determines the driving pressure, and the kinetic law updates the shape for every small time step. Repeats of these steps will then evolve the surface. Now replace the driving pressure p in equation (2.2) with the interface velocity v_n by using the linear kinetic law (2.3), giving

$$\int \frac{v_n}{m} \delta r_n dA = -\delta G \tag{2.11}$$

It describes that the actual velocity of the motion of the interface, v_n, satisfies equation (2.11) for arbitrary distribution of virtual motion, δr_n, on the interface. This statement is referred as weak statement of the problem.

The weak statement provides a global view regarding interface motion as a mean to release the total free energy. Comparing to the partial differential equation (2.10), the weak statement at least has the following advantages. First, equation (2.10) is incorrect when surface tension is anisotropic, whereas the weak statement (2.11) can easily circumvent the difficulties of anisotropy (even though the cases will be discussed in this thesis will focus on isotropic surface tension). Second, weak statement doesn't require the smoothness of surface. This merit is very useful to deal with the problems with complicate surface shape. Another very important advantage is that, because the problem has to be analyzed approximately in general, a partial differential equation may not be a good starting point. The integral form of weak statement is much easier for numerical analysis. One may find an approximate interface velocity that satisfies equation (2.11) for a family of virtual motions (instead of arbitrary virtual motions). Definitely, the larger the family, the more accurate the approximation. This consideration leads to Galerkin method, which will be roughly presented in next subsection.

2.1.4 Galerkin Method

The formal Galerkin method is listed here [11] and the detail finite element procedure will be specified for each certain case respectively.

Model the surface with n degrees of freedom, writing $q_1, q_2, \cdots q_{n-1}, q_n$ for the generalized coordinates, and $\dot{q}_1, \dot{q}_2, \cdots \dot{q}_{n-1}, \dot{q}_n$ for the generalized velocities. For example, a sphere has one

degree of freedom, its radius; a rod has two degrees of freedom, its radius and height; a general surface may be modeled by an assembly of triangles, with the positions of the vertexes being the generalized coordinates. The real coordinates of a point **x** on surface can also be expressed the generalized coordinates.The free energy is a function of the generalized coordinates, $\mathbf{G}(q_1, q_2 \cdots q_{n-1}, q_n)$, The generalized forces, $f_1, f_2, \cdots f_{n-1}, f_n$, are the differential coefficients of the free energy, namely

$$\delta G = -f_1 \delta q_1 - f_2 \delta q_2 - \cdots - f_{n-1} \delta q_{n-1} - f_n \delta q_n \equiv -\sum f_i \delta q_i \qquad \textbf{(2.12)}$$

Once the free energy function is known, the generalized forces are calculated from

$$f_i = -\partial G / \partial q_i \qquad \textbf{(2.13)}$$

The virtual motion of the surface, δr_n, is linear in the variations of the generalized coordinates:

$$\delta r_n = \sum \left(\mathbf{n} \cdot \frac{\partial \mathbf{x}}{\partial q_i} \right) \delta q_i \equiv \sum N_i \delta q_i \qquad \textbf{(2.14)}$$

The shape functions N_i depend on the generalized coordinates. The interface velocity is linear in the generalized velocities:

$$v_n = \sum N_i \dot{q}_i \qquad \textbf{(2.15)}$$

Now, substitute the above equations (2.12), (2.14) and (2.15) into the weak statement, (2.11), giving

$$\sum_{i,j} H_{ij} \dot{q}_j \delta q_i = \sum_i f_i \delta q_i \qquad \textbf{(2.16)}$$

where

$$H_{ij} = \int \frac{N_i N_j}{m} dA \qquad \textbf{(2.17)}$$

Since equation (2.16) holds for arbitrary virtual generalized coordinates changes, δq_i , the coefficient for each δq_i must be equal. Thus

$$\sum_j H_{ij}\dot{q}_j = f_i \tag{2.18}$$

Equation (2.18) is a set of linear algebraic equations for the generalized velocities. By solving these equations, the generalized coordinates will be updated for a small time step. The process is repeated for many time steps to evolve into the surface. Because the matrix H and the force column f depend on the generalized coordinate column q , equation (2.18) is a nonlinear dynamical system.

The matrix H is called the viscosity matrix, its physical interpretation is evident from equation (2.18): the element of the matrix, H_{ij}, is the resistant force in the q_i – direction when the state moves at unit velocity in q_j – direction. From equation (2.17), H is depends on the generalized coordinates but is independent on the generalized velocities or positions on the interface. The viscosity matrix is symmetric and positive-define.

2.2 Formulation of Diffusion on Interface

This section, another mechanism of mass transportation, mass diffusion on an interface, will be formulated. The interface may be either a free surface or a grain boundary. The diffusion species are taken to be electrically neutral, so that only mass conservation need be enforced. Same as evaporation-condensation, the free energy in this system may include surface energy, elastic energy, and external work etc. The terms will be determined for each case later.

2.2.1 Virtual Motion, Mass Conservation and Kinetic Law

Figure 2-2 illustrates a solid surface that represents either a free surface or a grain boundary in three dimensions. Denote the unit vector normal to the surface element by $\mathbf{n}$. An arbitrary contour lies on the surface, with the curve element dl, and the unit vector in the surface and normal to the curve element $\mathbf{m}$. At a point on the contour, $\mathbf{m}$ and $\mathbf{n}$ are perpendicular to each other and both are perpendicular to the tangent vector of the curve at the point.

Let's first consider two virtual motions. One of them is virtual mass displacement, denoted as $\delta\mathbf{I}$ [99] to distinguish it from the mass flux used below**.** It is a vector field tangent to the interface, such that $\delta\mathbf{I}\cdot\mathbf{m}$ is the volume of matter crossing per unit length of the curve. As before, $\delta\mathbf{I}$ **i**ndicates a virtual motion which means the amount of mass is infinitesimal and do not need to obey any kinetic law. Now, denote another virtual motion which is not shown in the Figure 2-2, $\delta\xi$. Let $\delta\xi$ be the volume of matter added to the interface per unit area. These two

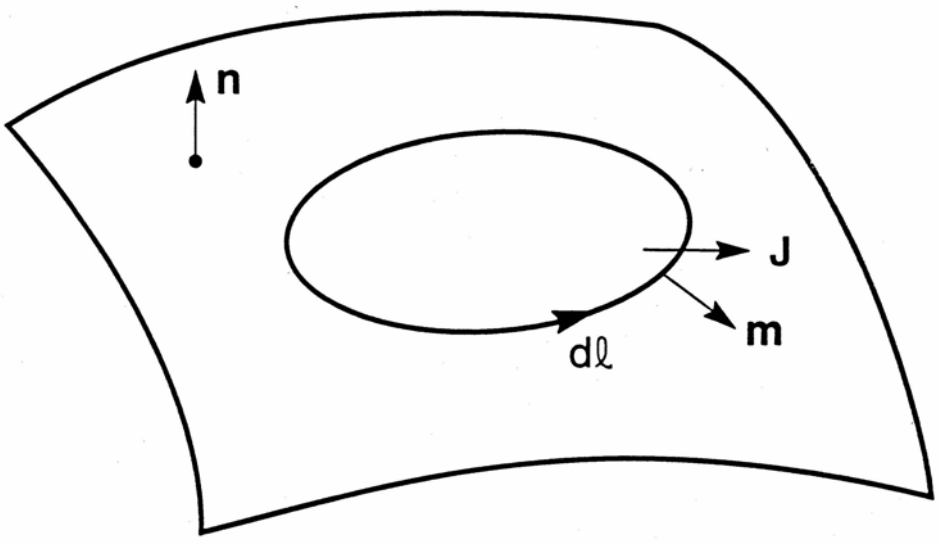

Figure 2-2: A solid interface in three dimensions. An arbitrary contour lying on the surface is shown. Suo [11]

virtual motion processes are not independent to each other. Because only diffusion involves into the mass transportation on the interface, they must satisfy the mass conservation law.

Consider the interface area enclosed by the contour in Figure 2-2. The mass conservation requires that the amount of mass added to the area equal to the amount of mass flowing in across the contour. Thus,

$$\int \delta\xi dA + \oint \delta\mathbf{I} \cdot \mathbf{m} dl = 0 \tag{2.19}$$

The first integral extends over the area of the interface enclosed by the contour, and the second one over the contour itself. The equation (2.19) must be satisfied by any contour and the enclosed area on the interface. Let two dimensional divergence theorem (surface divergence theorem), $\oint \delta\mathbf{I} \cdot \mathbf{m} dl = \int \nabla \cdot (\delta\mathbf{I}) dA$, applied. Substituting it into the equation (2.19), the mass conservation requirements then can be expressed in terms of surface divergence as the following,

$$\delta\xi + \nabla \cdot (\delta\mathbf{I}) = 0 \tag{2.20}$$

Define the time derivatives of these two kind of virtual motions. The mass flux, $\mathbf{J}$, is a vector field tangent to the surface, defined such that $\mathbf{J} \cdot \mathbf{m}$ is the volume of matter crossing per unit length of the curve per unit time. Let $\dot{\xi}$ be the volume of matter added to the interface per unit area per unit time. Similar to equations (2.19) and (2.20), the mass conservation requirements equations per unit time can be obtained

$$\int \dot{\xi} dA + \oint \mathbf{J} \cdot \mathbf{m} dl = 0 \tag{2.21}$$

and

$$\dot{\xi} + \nabla \cdot \mathbf{J} = 0 \tag{2.22}$$

Let's see what the $\dot{\xi}$ is. On the free surface, matter of the solid diffuses from one part of the surface to another. Mass added to a surface element cause the element to move in the direction toward the vacuum at the velocity $v_n = \dot{\xi}$. Thus, on the free surface

$$v_n = -\nabla \cdot \mathbf{J} \tag{2.23}$$

Now consider a grain boundary which is in local equilibrium. The mass inserted to the grain boundary immediately adds to either one of the two adjacent grains. Evidently, $\dot{\xi}$ determines the relative motion of one grain with respect to the other. But, the grain boundary itself does not migrate by this way. Denote the relative velocity as Δv_n, being positive when the two grains recede from each other. The mass added to a grain boundary element cause the two grains to drift apart at velocity $\Delta v_n = \dot{\xi}$. Thus, on the gain boundary

$$\Delta v_n = -\nabla \cdot \mathbf{J} \tag{2.24}$$

Associated with the virtual motion, $\delta \mathbf{I}$ (from discussion above, another virtual motion, $\delta \dot{\xi}$, is not independent of $\delta \mathbf{I}$), the free energy of the system varies by δG. Let $\mathbf{F}$ be the free energy reduction associated with a unit volume of matter relocating on the surface by diffusion per unit distance, which is the driving force for diffusion. That is,

$$\int \mathbf{F} \cdot \delta \mathbf{I} dA = -\delta G \tag{2.25}$$

The integral extends over the interface. The force vector, $\mathbf{F}$, is on the surface and equation (2.25) holds for arbitrary virtual motion.

Similar to previous section, free energy change only cannot determine the mass diffusion path. Following Herring [13], a linear kinetic law for interface diffusion is adopted,

$$\mathbf{J} = M\mathbf{F} \tag{2.26}$$

where M is the atomic mobility of diffusion on the interface. Although the mobility of diffusion, M, may depend on the crystalline direction and vary from point to point, an isotropic assumption is adopted in this thesis, giving,

$$M = \Omega D\delta / kT \tag{2.27}$$

where Ω is the volume per atom, D the self-diffusivity on the surface, δ the effective thickness of atoms participating in diffusion, k Boltzmann's constant, and T the absolute temperature.

2.2.2 Weak Statement and Galerkin Procedure

Simply replace the force in equation (2.25) with the mass flux by using the linear kinetic law (2.26), giving

$$\int \frac{\mathbf{J} \cdot \delta \mathbf{I}}{M} dA = -\delta G \tag{2.28}$$

The integral extends over all the interfaces in the system. The isotropic diffusion mobility is adopted though; different type of interfaces (i.e. free surface and grain boundary) may have different mobilities. The actual mass flux, $\mathbf{J}$, satisfies for all virtual motions $\delta \mathbf{I}$. Equation (2.28) is the weak statement of diffusion on the interface. The significant difference between interface diffusion and evaporation-condensation is that, for interface diffusion, mass conservation they must satisfy the mass conservation requirements equations (2.19) – (2.22).

The Galerkin procedure is similar to that in Section 2.1.4. Model the surface with n degrees of freedom, writing $q_1, q_2, \cdots, q_{n-1}, q_n$ for the generalized coordinates, and $\dot{q}_1, \dot{q}_2, \cdots, \dot{q}_{n-1}, \dot{q}_n$ for the generalized velocities. Following the dame procedure as in Section 2.1.4 to compute the generalized forces f_i, the virtual displacement δr_n, and the velocity of the interfaces v_n. Now, integral the differential equations of mass conservation requirements (2.20) and (2.22), giving

$$\delta I = \sum Q_i \delta q_i \tag{2.29}$$

and

$$J = \sum Q_i \dot{q}_i \tag{2.30}$$

where Q_i plays the similar role as the shape functions. The detail of these functions will be specified in later discusses. The weak statement (2.28) then can be leaded to the following equation with viscosity matrix,

$$H_{ij} = \int \frac{Q_i Q_j}{M} dA \tag{2.31}$$

As before, by solving these equations, the generalized coordinates will be updated to evolve into the surface. At a given time, the free energy variation determines the driving force, the kinetic law relates the driving force to the flux, and the flux then updates the surface shape according to mass conservation. The procedure repeats for the next time increment.

2.2.3 Differential Equations

Same as Section 2.1.2, the equivalent differential equations are presented here for completeness.

Consider an interface which is a closed surface in three dimensions. Herring [13] defined the chemical potential of an interface element, μ, as the increase of the free energy associated with the addition of one atom to the element. Here, a little bit change is made, consider μ as the increase of the free energy associated with the addition of a unit volume of mass to the element (i.e. volume of one atom, Ω.). Then it gives

$$\delta G = \int \mu \delta \dot{i} \, dA \tag{2.32}$$

The integral extends over the surface.

Apply the mass conservation law, equation (2.20), obtaining

$$\begin{aligned}\delta G &= -\int \mu \nabla \cdot (\delta \mathbf{I}) dA \\ &= -\int [\nabla \cdot (\mu \delta \mathbf{I}) - (\nabla \mu) \cdot \delta \mathbf{I}] dA\end{aligned} \tag{2.33}$$

Recall the surface divergence theorem, giving

$$\delta G = -\oint \mu \delta \mathbf{I} \cdot \mathbf{m} dl + \int (\nabla \mu) \cdot \delta \mathbf{I} dA \tag{2.34}$$

Since it is a close surface, the integral on the boundary vanishes. Finally, one obtains

$$\delta G = \int (\nabla \mu) \cdot \delta \mathbf{I} dA \tag{2.35}$$

Comparing these two equations, (2.25) and (2.35), the two integrals for arbitrary distribution of mass displacement, $\delta \mathbf{I}$, are equal, so that the two integrands must be identical, that is

$$\mathbf{F} = -\nabla \mu \tag{2.36}$$

The driving force is the negative gradient of the chemical potential. As expected, mass diffuse from an interfacial element with high chemical potential to an interfacial element with low chemical potential.

Let's now see what the velocity of the motion is when the mass diffusion occurs on the free surface and grain boundary respectively.

Recall equation (2.8), it defines the free energy variation associated with adding mass on the interface. For mass diffusion on the interface, the term of the difference in the free energy density vanishes because all matter is in the same phase. The equation can be reformed as the following

$$\delta G = \int (\gamma K + W) \delta i d A \tag{2.37}$$

where W is the energy density which may include strain energy density and electric energy density etc. As before, the surface tension, γ, is assumed to be isotropic, the sum of the two

principle curvature, K, is positive when the surface is convex. By comparing equation (2.37) with equation (2.32), one can obtain the chemical potential on the surface,

$$\mu = \gamma K + W \tag{2.38}$$

Substitute it into equation (2.36), giving the driving force

$$\mathbf{F} = -\nabla(\gamma K + W) \tag{2.39}$$

Combine the equation (2.39) with kinetic law (2.26) and mass conservation law (2.23), finally giving the velocity of the mass motion,

$$v_n = M\nabla^2(\gamma K + W) \tag{2.40}$$

This partial differential equation governs the motion of a free surface when the surface tension is isotropic.

Let σ_n be the normal stress on the grain boundary. To insert one unit amount of atom into the grain boundary, the normal stress does work, varying the free energy by

$$\delta G = -\int \sigma_n \delta i d A \tag{2.41}$$

Repeat the same steps as that of free surface. Consequently, the chemical potential is

$$\mu = -\sigma_n \tag{2.42}$$

The driving force for diffusion on the grain boundary is

$$\mathbf{F} = \nabla \sigma_n \tag{2.43}$$

Mass diffuse on the grain boundary from an element of low normal stress to an element of high normal stress.

Apply kinetic law (2.26) and mass conservation law on the grain boundary (2.24), giving

$$\Delta v_n = -M\nabla^2 \sigma_n \tag{2.44}$$

This partial differential equation governs the normal stress distribution on the grain boundary.

2.3 Multiple Kinetic Processes

This section, the weak statement for multiple kinetic processes is formulated. The formulations on the free surface and grain boundary are presented respectively.

2.3.1 On Free Surface

Consider two independent mass transportation mechanisms, mass diffusion and evaporation-condensation between solid and its vapor, occur the same time on the surface. Same symbols as that in Section 2.2 are used to denote the motion of diffusion on surface, such as mass displacement $\delta\mathbf{I}$, the mass flux $\mathbf{J}$ and the volume of matter added to the interface per unit area $\delta\xi$, etc. For evaporation-condensation process, denote δi as the volume of matter added to the surface per unit area by condensation. The mass exchange rate between the solid and the vapor is represented by flux j, which is the volume of matter added to a unit area of the solid surface per unit time due to evaporation-condensation.

Combining these two mass transportation mechanisms together, associated with the virtual motions, the total free energy reduces by

$$\int (\mathbf{F}\cdot\delta\mathbf{I} + p\cdot\delta i)dA = -\delta G \tag{2.45}$$

The integral extends over the entire surface area participating in mass transfer. Because $\delta\mathbf{I}$ and δi are independent and arbitrary, the weak statement defines the quantities $\mathbf{F}$ and p at every point on the surface.

Recall the kinetic laws for evaporation-condensation, equation (2.3) , and for mass diffusion, equation (2.26), respectively, consequently, the weak statement combining of mass diffusion and evaporation-condensation together is

$$\int \frac{\mathbf{J}\cdot\delta\mathbf{I}}{M}dA \; + \; \int \frac{j\cdot\delta i}{m}dA \; = -\,\delta G \tag{2.46}$$

Physically, $\delta\xi$ and δi represent independent ways to change solid shape. The shape change δr_n relates to the two ways by

$$\delta r_n = \delta i + \delta\xi \tag{2.47}$$

Recall the mass conservation law, equation (2.20), giving

$$\delta r_n = \delta i - \nabla\cdot(\delta\mathbf{I}) \tag{2.48}$$

In numerical simulation, as will be clear later, it is more convenient to treat δr_n and $\delta\mathbf{I}$ as independent quantities and subject δi to the constraint equation (2.48). Thus,

$$\delta i = \delta r_n + \nabla\cdot(\delta\mathbf{I}) \tag{2.49}$$

Same treatment is made for the two fluxes. Both fluxes $\mathbf{J}$ and j change the geometry of the solid. Mass conservation relates the normal velocity of the surface, v_n, to the fluxes of the two matter transport processes:

$$v_n = j - \nabla\cdot\mathbf{J} \tag{2.50}$$

Now, treat v_n and $\mathbf{J}$ as independent quantities and subject j to the constraint equation (2.50), giving,

$$j = v_n + \nabla\cdot\mathbf{J} \tag{2.51}$$

Substitute these two constraint relations (2.49) and (2.51), into the weak statement (2.46), giving us the reformed weak statement,

$$\int \frac{\mathbf{J}\cdot\delta\mathbf{I}}{M}dA \; + \; \int \frac{(v_n + \nabla\cdot\mathbf{J})\cdot\left[\delta r_n + \nabla\cdot(\delta\mathbf{I})\right]}{m}dA \; = -\,\delta G \tag{2.52}$$

In this form, the weak statement only involves two virtual fields, δr_n and $\delta \mathbf{I}$. They vary independently, subject to no constraint.

2.3.2 On the grain boundary

Consider a grain boundary which both migrates and acts as a diffusion path. Mass can migrates from one grain to another one, or, diffuses from surface into grain boundary and then distributes to the adjacent grains. Let δr_n be the virtual migration of the grain boundary, $\delta \mathbf{I}$ be the mass displacement on the grain boundary, and δG be the free energy variation associated with the combined virtual motion. Similar to evaporation-condensation, migration exchanges mass between solid and solid (two grains). Consequently, define the migration driving pressure p and the diffusion driving force $\mathbf{F}$ simultaneously by

$$\int \left(\mathbf{F} \cdot \delta \mathbf{I} + p \cdot \delta r_n \right) dA = -\delta G \tag{2.53}$$

The integrals extend over the grain boundary area. As discussion in Section 2.1.1, the diffusion on the grain boundary only recedes the two grains from each other buy not change the grain boundary itself. Thus, the mass displacement $\delta \mathbf{I}$ and the virtual migration δr_n are independent of each other, and the δr_n is associated with the actual velocity of the motion.

Replace the driving forces by the kinetic laws of the two processes, (2.3) and (2.26), giving

$$\int \frac{\mathbf{J} \cdot \delta \mathbf{I}}{M} dA + \int \frac{v_n \cdot \delta r_n}{m} dA = -\delta G \tag{2.54}$$

where m is the mobility of migration of grain boundary and the actual migration velocity v_n and flux $\mathbf{J}$ satisfy this weak statement for arbitrary mass conserving virtual motion. Turnbull [97] showed that the interface velocity is linear in the driving pressure if $\Omega p << kT$. The interface

motion involves the same atomic process as self-diffusion on the interface. The interface mobility m relates to the self-diffusion on the interface D by $m = \Omega^{2/3} D / kT$.

2.3.3 Mass Transportation on Multiple Interfaces

Consider an interface combining of both free surface and grain boundary. On one hand, mass diffusion on the free surface and flow along grain boundary then distribute into two grains; on the other hand, mass exchange between solid and its vapor on the free surface and between two grains which causes grain boundary migration.

Simply combine the weak statement on the free surface for two processes, diffusion and evaporation-condensation, the equation (2.52), and the weak statement on the grain boundary for diffusion and migration of grain boundary, equation (2.54), giving

$$\int \left\{ \frac{\mathbf{J} \cdot \delta \mathbf{I}}{M_s} + \frac{\left(v_n + \nabla \cdot \mathbf{J}\right)\left[\delta r_n + \nabla \cdot \left(\delta \mathbf{I}\right)\right]}{m_s} \right\} dA + \int \left\{ \frac{\mathbf{J} \cdot \delta \mathbf{I}}{M_{gb}} + \frac{v_n \delta r_n}{m_{gb}} \right\} dA = -\delta G \qquad \textbf{(2.55)}$$

The first term of integrals on the left hand side extends over the free surface area; the second term of integrals extends over the grain boundary area. M_s and M_{gb} represent the mobilities of surface diffusion and grain boundary diffusion, respectively; and m_s and m_{gb} represent the mobilities of mass exchange on free surface and grain boundary diffusion, respectively. The free energy on the right hand side includes any free energy of the full system, both on free surface and grain boundary, such as free surface tension and grain boundary tension.

Equation (2.55) is the general form of weak statement which includes multiple kinetic processes (i.e. diffusion and migration of interface) and multiple types of interface (i.e. free surface and grain boundary) in three dimensions. Other kinetic processes can be similarly added to the weak statement. An example is given in Appendix A.

Chapter 3

3 Surface Evolution of Stressed Thin Film

In the following, the well known problem, the morphology evolution of a residually stressed thin film, is simulated. Consider a thin film attached to a substrate (Figure 3-1). Assume the elastic strain mismatch between the substrate and film is ε_0, such that the corresponding in-plane biaxial stress is $\sigma_0 = E\varepsilon_0/(1-\upsilon)$, where E and υ are Young's modulus and Poisson ratio of the

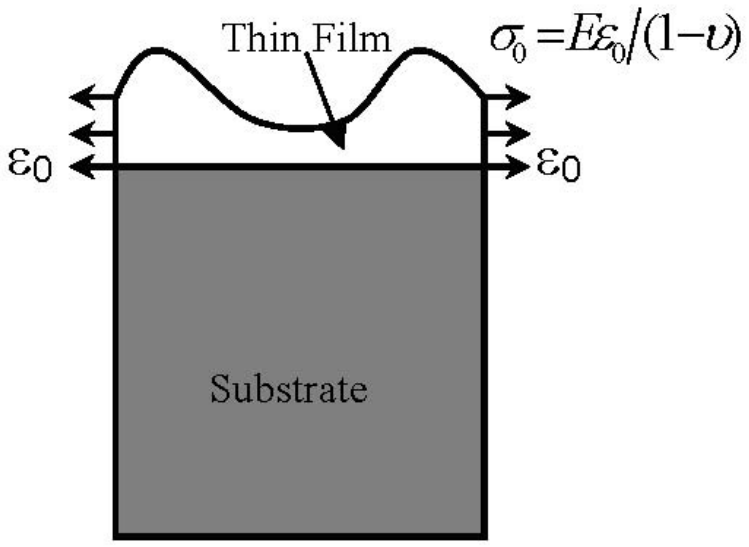

Figure 3-1: A thin film on a substrate with elastic strain mismatch ε_0.

thin film. Assume that the substrate is much thicker than the thin film (i.e. the thickness of substrate is ten times more than that of thin film), thus, the stress in substrate can be ignored. For simplicity of discussion, the assumption that the substrate has the same elastic constants as the thin film is adopted. The instability appears then furthermore forms groove when the mass transportations occur on the surface of the stressed thin film. Two mass transportation mechanisms, surface diffusion and evaporation-condensation, will be considered being involved into this case.

This chapter is arranged as following. Loading conditions will be discussed in the next section. Then the weak statement presented in chapter 2 will be reviewed and specified. Afterward, the surface grooves induced by surface diffusion and evaporation-condensation will be simulated and compared with each other. The similarity and difference between them will be discussed. The effect of the mobility ratio of two processes when they are concurrent is studied also. Finally, the dependence of surface kinetic pathway on its initial profile is focused and discussed. Surfaces with initial sharp cracks, sharp and semicircle notches are simulated.

3.1 Loading Condition

Figure 3-1 already shows the loading condition of this case. Since boundary element method is used to solve the stress field, the solution of half-plane problem, e.g. combining the thin film and substrate together, is much more accurate than that of thin film. But the discontinuous boundary condition (i.e. the jump of strain between thin film and substrate) occurs for the half-plane problem, which is not that good for BEM numerical implementation. To get rid of this trouble, one can assume the substrate has the same strain as thin film, which is shown in Figure 3-2.

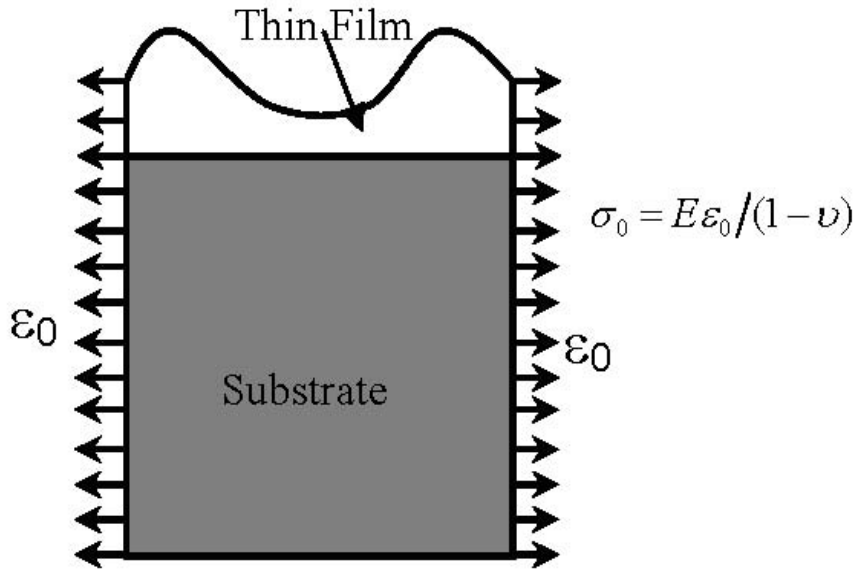

Figure 3-2: Loading condition for half-plane problem. Elastic strain mismatch ε_0 apply to both thin film and its substrate.

The above assumption simplifies the numerical process and makes it more accurate. But the changes of the loading condition make the problem no longer same as the original case. The stress fields of the whole body (thin film and substrate together) under these two loading conditions are different from each other obviously. It is needed to be evaluated that how this change of loading condition affects the case which is being discussed.

As shown in Figure 3-3, separate both original and replacing problems into two parts. One part of the original problem is that a uniform stress filed applied on the thin film body and the other part is a stress field applied on the surface of thin film. Similarly, the replacing problem has one part of uniform stress field applied on the whole body and one part of stress field applied on the surface of thin film. One can see that although the parts with uniform stress filed applied of these two problems are different from each other, the parts with stress field applied on the free surface are exactly the same. Considering our current case, surface profile evolves by surface

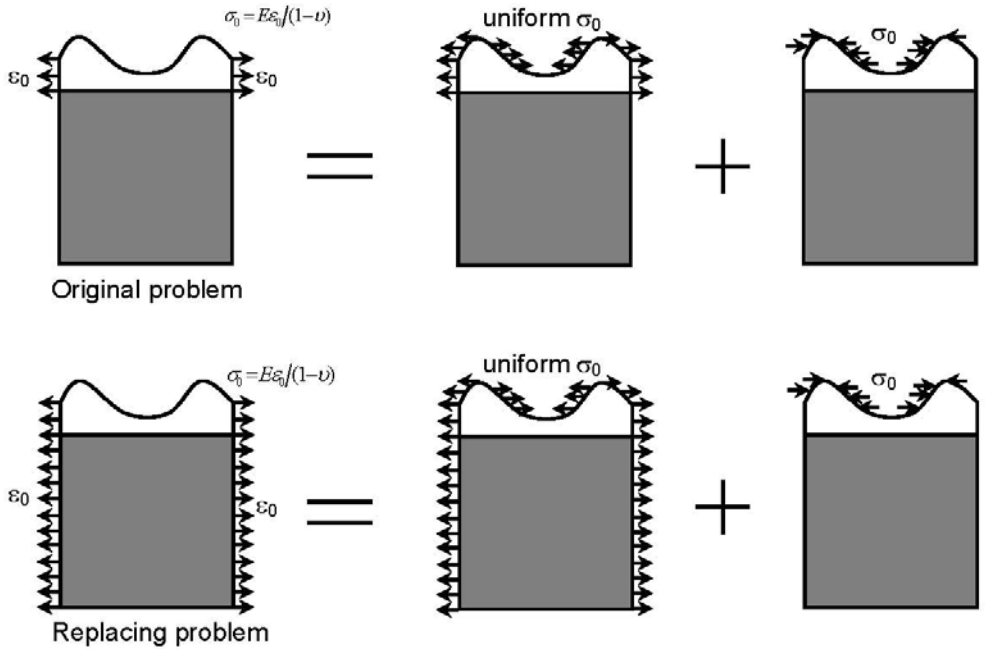

Figure 3-3: Both original problem and replacing problem are separated into two parts, a uniform stress filed part and a surface stress field part. The surface stress field parts of these two problems are exactly same as each other.

diffusion and/or evaporation-condensation. Because both mass transportation mechanisms occur on the free surface, only the strain energy on the free surface, which is counted into free energy of the system, is sensitive to this problem. This condition approves that the solution of the replacing problem is reliable for the original case.

Figure 3-4 shows the loading condition used to solve the replacing problem on half of the simulating cell. One side is fixed in horizontal direction, and the other side is prescribed a horizontal displacement $l\varepsilon_0$, where l is the simulating cell width (i.e. the wavelength of the sinusoidal perturbation on the flat surface), ε_0 the initial uniform strain of the thin film and the

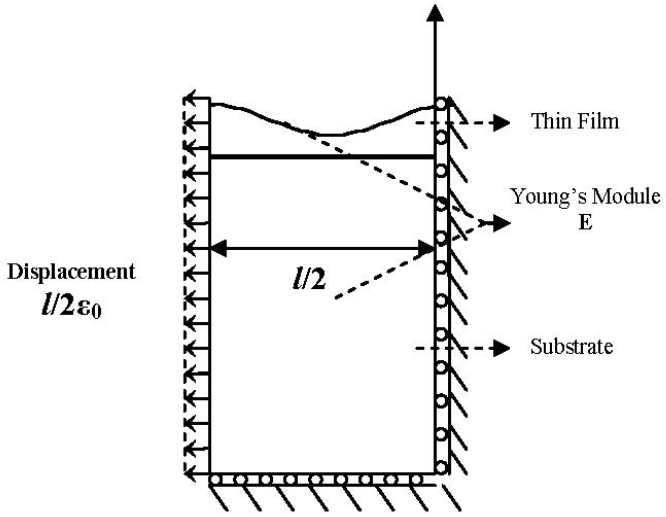

Figure 3-4: The loading condition of half simulating cell

substrate. The top surface is traction free. As mentioned above, the thin film and the substrate have the same Young's Modulus E and Poisson ratio υ.

3.2 Formulations and Numerical Implementation

This section, the numerical scheme is described. First, the weak statement will be reviewed and specified into two-dimensional case. The detail finite element following Galerkin procedure then is presented. Also the calculation of strain energy density on the surface based on the solution of the stress field solved by boundary element method will be discussed.

3.2.1 Weak Statement in Two Dimensions

Recall the general weak statement in three dimensions, equation (2.55). Since the current case being studied only occurs on the free surface and involves two mass transportation methods, surface diffusion and evaporation-condensation. The weak statement then becomes

$$\int \left\{ \frac{\mathbf{J} \cdot \delta \mathbf{I}}{M} + \frac{\left(v_n + \nabla \cdot \mathbf{J}\right)\left[\delta r_n + \nabla \cdot \left(\delta \mathbf{I}\right)\right]}{m} \right\} dA = -\delta G \tag{3.1}$$

The integral extends over the surface area.

Consider the half plane problem. The solid is invariant in one direction, and its shape change can be studied in a cross-section perpendicular to that direction. In the cross-section, the solid is represented by an area and the surface by a curve. The weak statement for this two-dimensional problem without grain-boundary diffusion involved becomes

$$\int \left\{ \frac{J\delta \mathbf{I}}{M} + \frac{\left(v_n + \partial J / \partial s\right)\left[\delta r_n + \partial\left(\delta \mathbf{I}\right)/\partial s\right]}{m} \right\} ds = -\delta G \tag{3.2}$$

The integral extends over the curve which represents the surface. The virtual mass displacement associated with surface diffusion, $\delta \mathrm{I}$, is the volume of atoms crossing a unit length curve segment in the thickness direction.

Consider the residually stressed thin film in this case. Since the residual stress is caused by the mismatch strain between thin film and substrate, there is no work done by the external load. The total free energy of the solid body includes surface tension γ and strain energy. Assume there is no chemical energy difference associated with depositing unit volume of mass on solid phase from vapor, when the solid is flat and stress free (i.e. $g = 0$). The total free energy of the system is

$$G = \int_{surface} \gamma dA + \int_{solid\ body} w dv \tag{3.3}$$

where w is the strain energy density. The first term of the integral extends over the surface area and the second term of the integral extends over the solid body. Consequently, in two-dimensional case, the free energy change due to the virtual motions is

$$\delta G = \int \gamma \delta(ds) + \int w \delta r_n ds \tag{3.4}$$

3.2.2 Finite Element

As stated above, the weak statement demands that the actual fields J and v_n, satisfy equation (3.2) for all virtual motions. To obtain an approximate solution of J and v_n, one relaxes this demand. Instead of requiring that equation (3.2) be satisfied for all virtual motions, one requires that equation (3.2) be satisfied for a family of virtual motions. A finite element method is one way to implement this idea. Let's recall and detail the Galerkin procedure in the following. Because the weak statement requires low order differentials only and does not have the requirement of smoothness of the surface, the curve is modeled by an assembly of straight segments. For example, a particle is modeled by a polygon of many sides. Each segment is an element, and two neighboring elements meet at a node. The motions of the nodes constitute the family of virtual motions. In principle, the length of each element is arbitrary, and different elements can have different lengths. In practice, short elements are placed where a curved object is of interest and long elements are placed elsewhere to reduce computation time.

Figure 3-5 shows one element, with two nodes at the positions (x_1, y_1) and (x_2, y_2). The element has length l and slope θ; the local coordinate, s, is measured from the middle point of the element. When the two nodes change positions by $(\delta x_1, \delta y_1)$ and $(\delta x_2, \delta y_2)$, the element remains to be straight, elongating, translating, and rotating, according to the nodal position changes. Consequently, at points the element moves in the normal direction by distance

$$\delta r_n = N_1 \delta x_1 + N_2 \delta y_1 + N_3 \delta x_2 + N_4 \delta y_2 \tag{3.5}$$

with the interpolation coefficients being

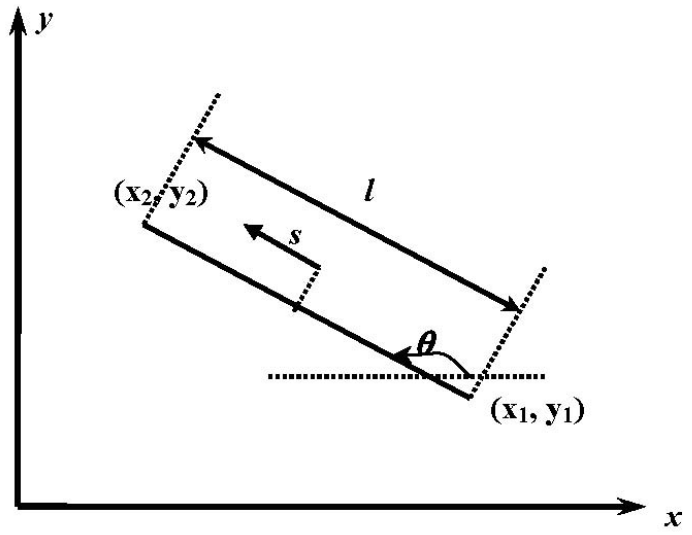

Figure 3-5 : A straight line element.

$$N_1 = \left(\frac{1}{2} - \frac{s}{l}\right)\sin\theta \qquad N_2 = -\left(\frac{1}{2} - \frac{s}{l}\right)\cos\theta$$
$$N_3 = \left(\frac{1}{2} + \frac{s}{l}\right)\sin\theta \qquad N_4 = -\left(\frac{1}{2} + \frac{s}{l}\right)\cos\theta \tag{3.6}$$

And the element length changes by

$$\delta l = -\cos\theta\delta x_1 - \sin\theta\delta y_1 + \cos\theta\delta x_2 + \sin\theta\delta y_2 \tag{3.7}$$

Similarly, when the nodes move at velocities $(\dot{x}_1, \dot{y}_1)$ and $(\dot{x}_2, \dot{y}_2)$, at points the element moves in the normal direction at velocity

$$v_n = N_1\dot{x}_1 + N_2\dot{y}_1 + N_3\dot{x}_2 + N_4\dot{y}_2 \tag{3.8}$$

For the other independent virtual motion, mass displacement $\delta \mathrm{I}$, let $\delta \mathrm{I}_1$, $\delta \mathrm{I}_2$ and $\delta \mathrm{I}_m$ be the virtual mass displacements at the two end nodes and the mid-point of the element. Interpolate the mass displacement at point s on the element by

$$\delta \mathrm{I} = Q_1 \delta \mathrm{I}_1 + Q_m \delta \mathrm{I}_m + Q_2 \delta \mathrm{I}_2 \tag{3.9}$$

with the interpolation coefficients being

$$Q_1 = \frac{s}{l}\left(\frac{2s}{l} - 1\right),\ Q_2 = \frac{s}{l}\left(\frac{2s}{l} + 1\right),\ Q_m = 1 - \left(\frac{2s}{l}\right)^2 \tag{3.10}$$

The same interpolation is used for the flux J. Let J_1, J_2 and J_m are the fluxes at the two end nodes and the mid-point of the element, the flux at point s on the element is given by

$$J = Q_1 J_1 + Q_m J_m + Q_2 J_2 \tag{3.11}$$

In summary, each element has seven degrees of freedom, includes four degrees of freedom $(\delta x_1, \delta y_1, \delta x_2, \delta y_2)$, to describe the motion of the element and three degrees of freedom $(\delta \mathrm{I}_1, \delta \mathrm{I}_2, \delta \mathrm{I}_m)$ to describe the mass diffusion on the element. For each surface element, the generalized coordinates q^e is, namely

$$q^e = \begin{bmatrix} x_1 & y_1 & \mathrm{I}_1 & x_2 & y_2 & \mathrm{I}_2 & \mathrm{I}_m \end{bmatrix}^T \tag{3.12}$$

Consequently, virtual changes in the generalized coordinates δq^e is

$$\delta q^e = \begin{bmatrix} \delta x_1 & \delta y_1 & \delta \mathrm{I}_1 & \delta x_2 & \delta y_2 & \delta \mathrm{I}_2 & \delta \mathrm{I}_m \end{bmatrix}^T \tag{3.13}$$

and the generalized velocities $\dot{q}^e$ is

$$\dot{q}^e = \begin{bmatrix} \dot{x}_1 & \dot{y}_1 & \mathrm{I}_1 & \dot{x}_2 & \dot{y}_2 & \mathrm{I}_2 & \mathrm{I}_m \end{bmatrix}^T \tag{3.14}$$

For each element, the integral over the surface in the weak statement (3.2) gives a bilinear form

$$\left(\delta q^e\right)^T \mathbf{H}^e q^e = -\delta G \tag{3.15}$$

where $\mathbf{H}^e$ is a 7 x 7 matrix, the components of which are given in the Appendix B.

The right-hand side of the weak statement (3.2), δG, is a sum over all the elements. Assume f^e is the column of driving forces associated with the generalized coordinates of one element. Because free energy varies as the shape varies, only the driving forces associated with the virtual

motions of the coordinates, $(\delta x_1, \delta y_1, \delta x_2, \delta y_2)$, are used. No driving forces are associated with $(\delta \mathrm{I}_1, \delta \mathrm{I}_2, \delta \mathrm{I}_m)$. Thus, for one element, the free energy reduction of the element with the virtual motion is

$$-\delta G = f_1 \delta x_1 + f_2 \delta y_1 + f_3 \delta x_2 + f_4 \delta y_2 \tag{3.16}$$

The corresponding generalized driving forces for one element is

$$f^e = \begin{bmatrix} f_1 & f_2 & 0 & f_3 & f_4 & 0 & 0 \end{bmatrix}^T \tag{3.17}$$

The detail factors of the driving force column are presented in Appendix C.

Assemble all the nodal velocities and fluxes into a column $\dot{q}$, and the corresponding virtual movements and mass displacements into a column δq. Assemble all the nodal driving forces into the column f and arrange their sequence such that $-\delta G = \delta q^T f$. Sum over all the elements, equation (3.2) becomes

$$(\delta q)^T \mathbf{H} \dot{q} = (\delta q)^T f \tag{3.18}$$

The matrix $\mathbf{H}$ is assembled from the contributions of all the elements. Equation (3.18) holds for any virtual motion δq, so that

$$\mathbf{H} \dot{q} = f \tag{3.19}$$

$\mathbf{H}$ is called the viscosity matrix. The components of the viscosity matrix $\mathbf{H}$ and force vector f depend on generalized coordinates q.

Consequently, equation (3.19) is a set of nonlinear ordinary differential equations that govern the generalized coordinates as a function of time. The equation (3.19) shows that the velocity direction usually differs from the direction of the generalized force, i.e., gradient of free energy. Equation (3.19) is integrated numerically to evolve the surfaces.

3.2.3 Calculation of Strain Energy Density and Numerical Algorism

Strain energy density at solid surface is needed to be calculated the force vector in equation (3.19). Due to the advantage of Boundary Element Method (BEM) discussed earlier in Chapter 1, BEM (e.g. [100**,** 101]) is used for obtaining the strain energy density on and/or near to the free surface. In Appendix D, the brief description of BEM is presented for completeness of this thesis. Another advantage of BEM is that both BEM and the equation for surface evolution, equation (3.19), are formulated on solid surface. No calculation of internal stresses or displacements is needed. Since mechanical equilibrium can be established instantaneously compared to the rate of surface evolution, an assumption that thin film solid is always in mechanical equilibrium when its surface evolves is adopted. Thus, stress field can be solved independently by using elasostatics for any given surface configuration at any given moment.

After solving equations in BEM, the displacements and tractions along the solid boundary have been obtained immediately. In order to calculate the strain energy density along evolving surface, other stress components are also needed. Theoretically, these stress components can be obtained by integrating displacements or tractions with corresponding kernel functions along the boundary. However, due to the singularities of the integration kernels, such approach would generate large numerical error near surface [100]. Follow [100], in this work, all unknown stress components are calculated by using local displacements at the surface. The idea is as follows. Consider a local coordinate at a point on the solid surface, with x_3- axis in the normal direction, and x_1- and x_2- axes in two tangential directions. The traction components are σ_{31}, σ_{32} and σ_{33}, which are known either from boundary condition or the solutions from BEM. By using the displacements at neighboring points, one can calculate their derivatives with respect to x_1- and x_2- axes, to obtain the in-plane strains, ε_{11}, ε_{12} and ε_{22}. Thus, the corresponding in-plane

stresses, σ_{11}, σ_{12} and σ_{22}, can be calculated from generalized Hook's law. Knowing all the stress components, the local strain energy density along surface then can be calculated. In the simulation, quadratic elements in BEM are used for stress and strain energy density calculation.

Let's simply describe the numerical algorism here Figure 3-6 shows the flow chart of the algorism. Imagine at the time t in a simulation. The current surface configuration was solved from last time step and one want to know the configuration after a time increment Δt. First, solve the stress field under given boundary conditions and current geometry by using BEM. Then by using the current generalized coordinates, calculate viscosity matrix $\mathbf{H}$ and force vector f in equation (3.19). By solving equation (3.19), get nodal velocities, which are integrated over a small time step using Runge–Kuta method to get surface configuration and/or new boundary conditions after one time step. Repeat the procedure to evolve the surface.

3.3 Morphology Evolution with Small Perturbation on Surface

3.3.1 Surface Grooving due to Surface Diffusion

Assume surface diffusion is the only mass transport mechanism to induce surface morphology change. For a small sinusoidal perturbation of wavelength l, the perturbation

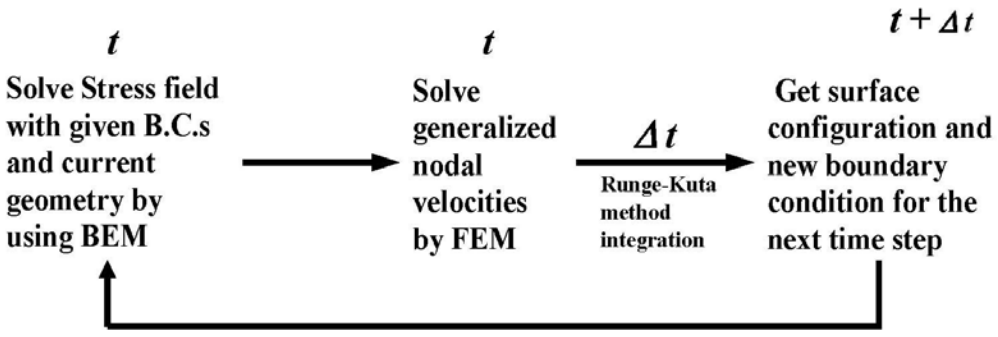

Figure 3-6: Flow chart of the numerical algorism.

waviness will either grow or decay. Denote Λ as a dimensionless loading parameter,

$$\Lambda = \frac{(1-\nu^2)\sigma_0^2 l}{E\gamma} \tag{3.20}$$

to represent the competition between strain energy reduction and surface energy increase associated with surface roughening. From linear stability analysis [38], for an initial small sinusoidal perturbation, when the groove depth d, which is the height difference between the peak and valley of the waviness, is much smaller than the wavelength, i.e. $d/l << 1$, one have

$$d = d_0 \exp\left(\frac{\Lambda}{\pi} - 1\right) t_N^d \tag{3.21}$$

where d_0 is the initial groove depth and t_N^d is the normalized time for diffusion process,

$$t_N^d = M\gamma\left(\frac{2\pi}{l}\right)^4 t \tag{3.22}$$

From equation (3.21), the perturbation will grow when Λ is large than π.

The above analytical result is used to check our numerical code. Comparing the unit of the two integral terms in the weak statement (3.2), one can observe that the unit of mobility of surface diffusion M is the same as the mobility of evaporation-condensation multiplies second order of length, i.e. ml_e^2. l_e here is a representative length in a problem. The dimensionless ratio ml_e^2/M measures the relative rate of surface diffusion and evaporation-condensation. When $ml_e^2/M << 1$, the effect of evaporation-condensation is negligible on processes occurring on the length scale l_e and any length scales smaller than l_e. In our numerical simulation, the cell length l is chosen as the representative length and a very small number $\left(10^{-6}\right)$ is assigned to ml^2/M to ensure mass conservation in the surface diffusion process and ignore the evaporation-condensation process.

In Figure 3-7, groove depth as a function of normalized time, t_N^d, for five different values of loading parameter Λ is plotted. The dots are from our numerical simulation and the solid lines are from the analytical solution, equation (3.21).

In the two cases of groove depth decaying, $\Lambda = 1$ and $\Lambda = 3$, d/l is always very small, so the numerical results perfectly match the theoretical prediction by equation (3.21). The numerical results for other three unstable cases, $\Lambda = 4$, $\Lambda = 5$, and $\Lambda = 9$, agree well with the theoretical results at small groove depth, but diverge quickly when grooves are close to cusp-shape. The cusps can further deepen, until local stress is large enough to cause de-cohesion cracking [54]. The results show that from initial small perturbation to forming cusps, most of evolution time is spent on the stage of small groove depth. When the load increases, the surface

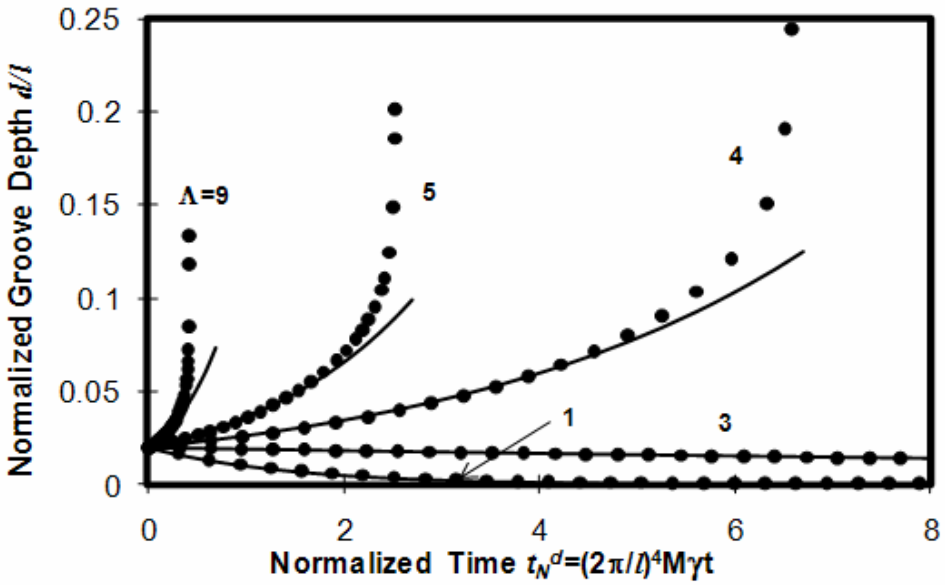

Figure 3-7: Groove depth vs. normalized time for surface diffusion induced grooving. The dots are from numerical simulations and solid lines from linear stability analysis.

forms cusps in shorter time, and the cusps are more localized, with major shape change near the grooves. All the above simulations start from the same initial small sinusoidal perturbation, with $d_0/l = 0.02$. The time sequences of surface profile of morphology evolution for two unstable cases, $\Lambda = 5$ and $\Lambda = 9$, are shown in Figure 3-8 and Figure 3-9, respectively. The surface forms localized cusp in very short time for $\Lambda = 9$ and a relative longer time for $\Lambda = 5$.

3.3.2 Surface Grooving due to Evaporation-Condensation

If surface evolution is only governed by the process of evaporation-condensation, from linear perturbation analysis, when groove depth is very small ($d/l << 1$), it also follows equation

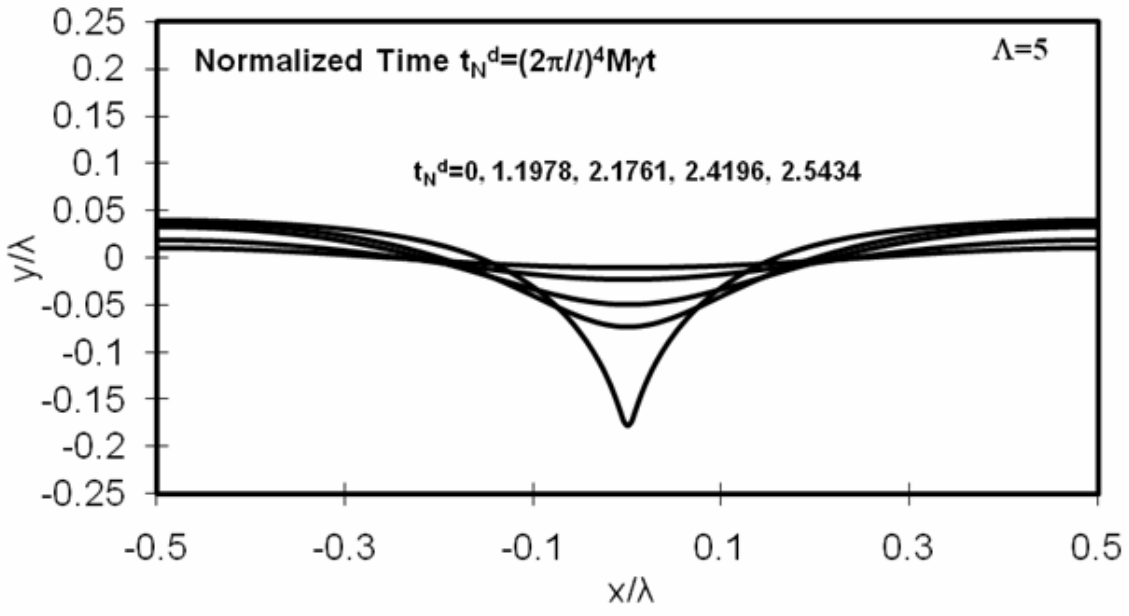

Figure 3-8: Surface profiles of morphology evolution caused by surface diffusion (Λ= 5).

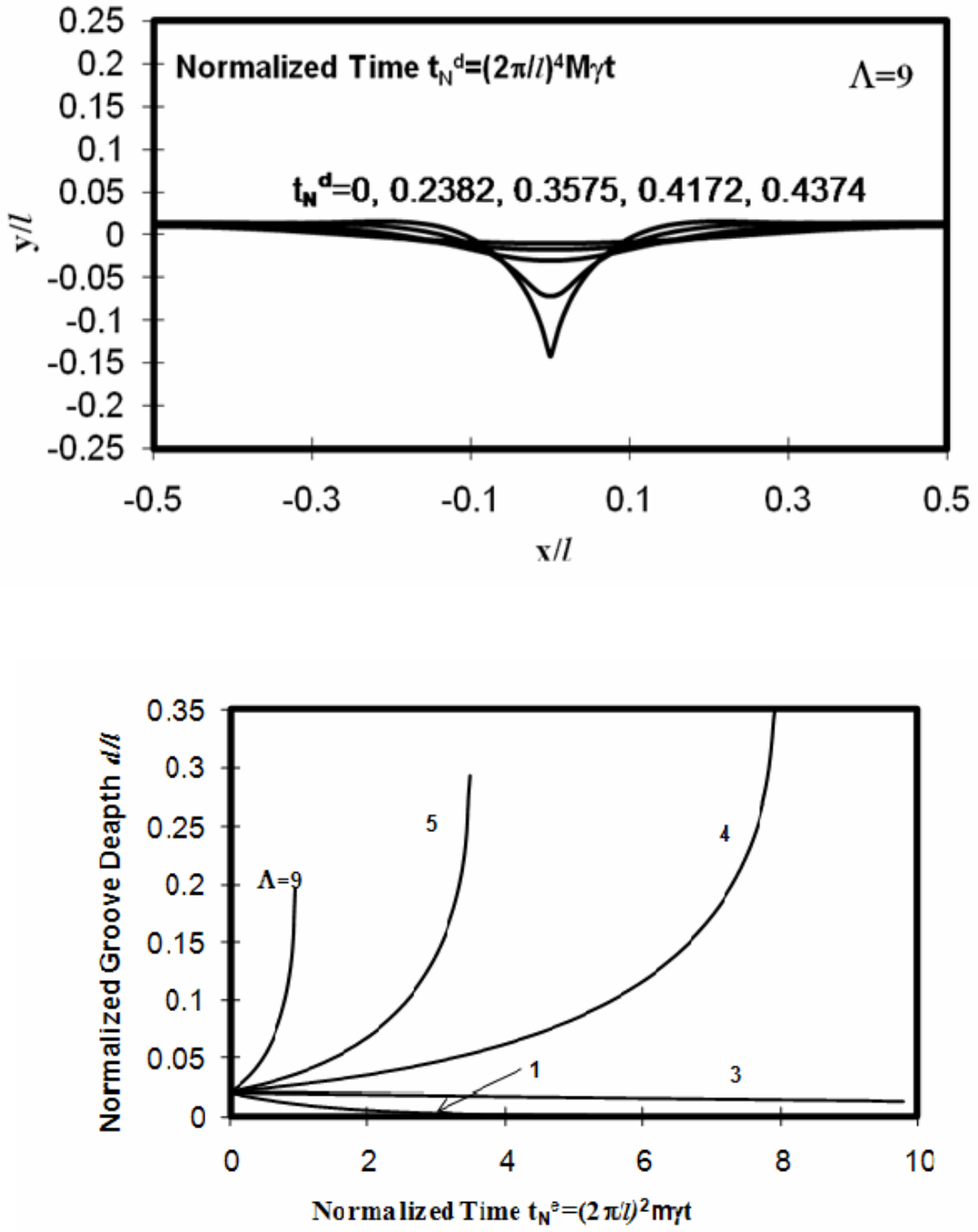

Figure 3-10: Groove depth vs. normalized time for evaporation-condensation induced grooving.

(3.21), but with the different normalized time,

$$t_N^e = m\gamma\left(\frac{2\pi}{l}\right)^2 t \qquad \textbf{(3.23)}$$

As a comparison to Figure 3-7, Figure 3-10 plots the groove depth versus normalized time t_N^e from our simulation results. It has the same general trend as in Figure 3-7. However, under same load level, the depth of groove at the time when sharp-tipped cusp forms is larger than that in surface diffusion controlled surface grooving, shown in Figure 3-7.

The time sequences for surface morphology evolution profiles are given in Figure 3-11 and Figure 3-12 for the cases of $\Lambda = 5$ and $\Lambda = 9$, respectively. Though there is no chemical energy difference, g, between the solid and its vapor, they still exchange mass from each other due to the effects of stress and curvature. The surface not only changes shape but also the overall position because mass is not conserved in the solid. The surface profiles first approaches to a nearly steady shape at which the solid body loses mass evenly over the entire surface. Later, the solid loses mass preferentially at the groove root and a cusp finally forms. Compare with the surface evolution shown in Figure 3-8 and Figure 3-12 under the same load, surface profile change due to evaporation-condensation is more global than that controlled by surface diffusion, which generates a localized groove. When cusp forms, the groove depths in the evaporation-condensation controlled cases are $0.27l$ and $0.19l$ for load $\Lambda = 5$ and $\Lambda = 9$, comparing to $0.17l$ and $0.13l$ in surface diffusion cases. Of course, the above two numbers depend on the stop criterion used in simulation, but the general conclusion is that surface cusp generated by evaporation/condensation is wider and deeper than that by surface diffusion.

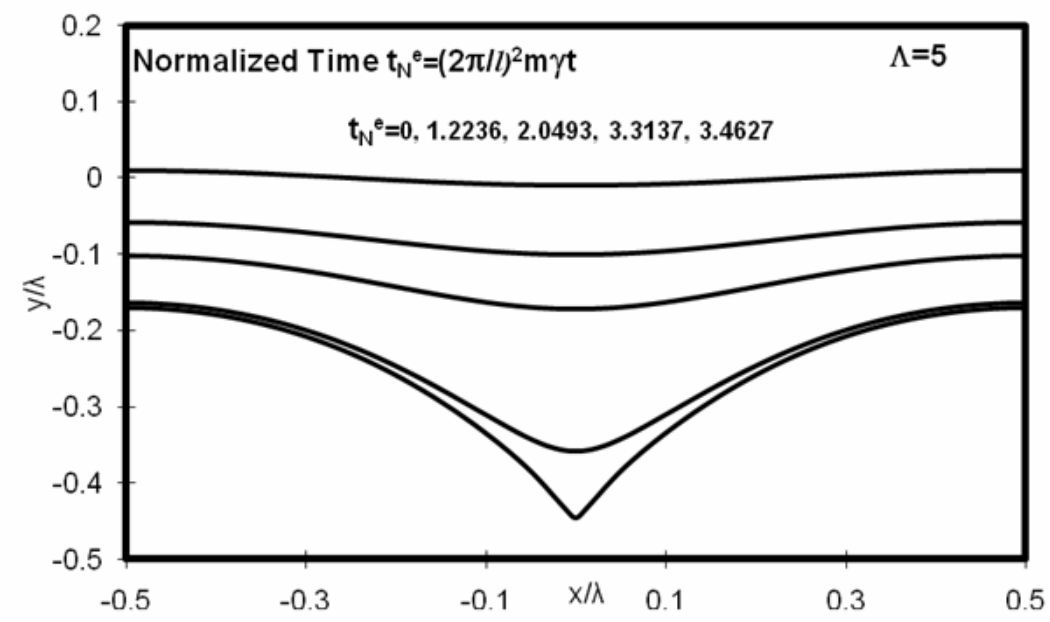

Figure 3-11: Surface profiles of morphology evolution caused by evaporation-condensation (Λ= 5).

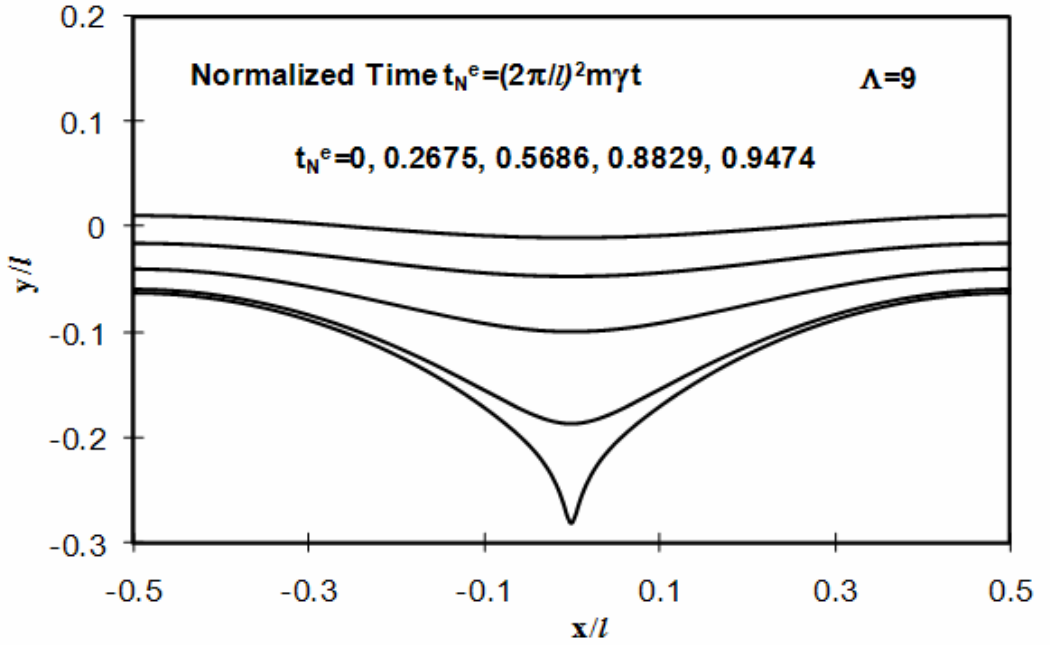

Figure 3-12: Surface profiles of morphology evolution caused by evaporation-condensation (Λ= 9).

3.3.3 Concurrent Surface Diffusion and Evaporation-Condensation

In the above two cases, surface evolution is governed by either surface diffusion or evaporation-condensation. The program, based on the weak statement, equation (3.2), can naturally deal with concurrent surface diffusion and evaporation-condensation or deposition. In this section, several cases with different mobility ratios ml^2/M, but same load, $\Lambda = 5$ have been simulated. From equations (3.22) and (3.23), there are two characteristic times,

$$\tau_d = l^4/(2\pi)^4 M\gamma \tag{3.24}$$

for surface diffusion and

$$\tau_e = l^2/(2\pi)^2 m\gamma \tag{3.25}$$

for evaporation-condensation. Two characteristic times are same when $ml^2/M = 39.5$.

For comparison, Table 3-I shows the dependence of cusp forming time, normalized by τ_d and τ_e respectively, on the mobility ratio ml^2/M. Although in theory, it does not matter how the time is normalized, but numerically, when two characteristic times are much different, as in

Table 3-I: The dependence of cusp forming time on the mobility ratio of evaporation and surface diffusion.

ml^2/M	Normalized Cusp Forming Time	
	$t_N^d = t/\tau_d$	$t_N^e = t/\tau_e$
10^{-6}	2.543	6.4×10^{-8}
0.1	4.374	0.011
10	5.151	1.305
100	0.807	2.043
10^4	0.014	3.463
10^6	1.4×10^{-4}	3.513

the cases in Figure 3-7 and Figure 3-10, the smaller characteristic time has to be used to normalize time, to ensure enough resolution in time. Table 3-I shows that the cusp forming time is about several τ_d when $ml^2/M < 100$, and about several τ_e when $ml^2/M \geq 10$. To avoid numerical errors, in the simulations, the time in the first three cases in Table 3-I are normalized by surface diffusion characteristic time τ_d and the time in the last three cases are normalized by evaporation-condensation characteristic time τ_e.

Figure 3-13 plots the groove depth as a function of normalized time t_N^d, which is normalized by characteristic time τ_d, for the cases which are dominated by surface diffusion. The mobilities ratio range is $m_s l^2/M_s \leq 10$. From Figure 3-13, when surface diffusion mobility is fixed, but

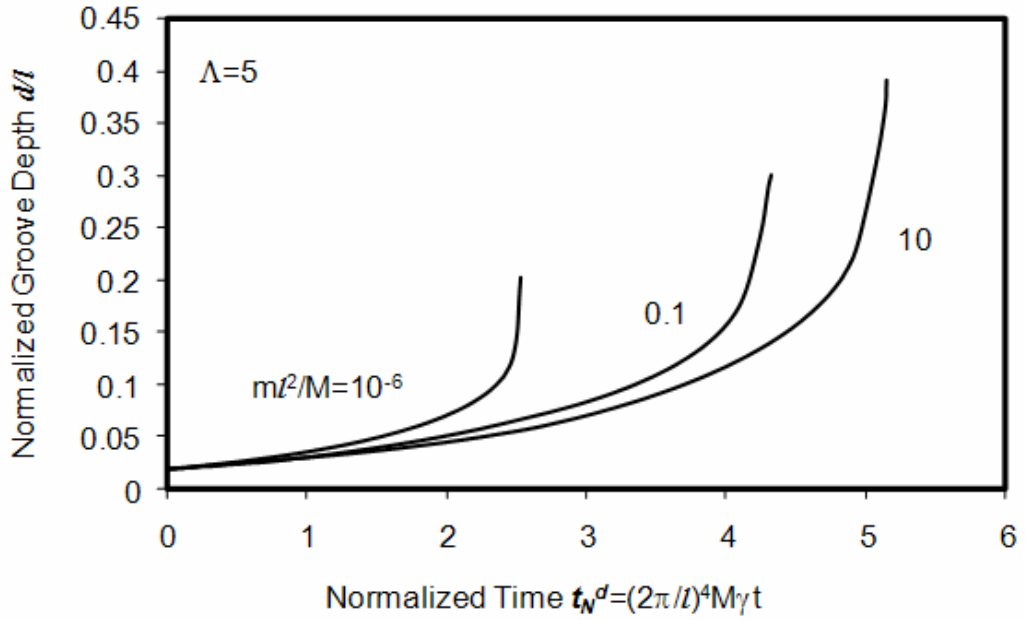

Figure 3-13: Groove depth vs. normalized time for grooving due to concurrent surface diffusion and evaporation-condensation. Surface diffusion dominant, $ml^2/M = 10^{-6}, 0.1, 10$.

evaporation-condensation mobility increases, surface forms cusp slower and the groove depth when cusp forms is deeper. The results can be explained by the surface profiles in Figure 3-8 and Figure 3-11. When surface diffusion is the only mass transport process, because the gradient of chemical potential at the surface is greater near to groove than at peak, the mass removed from the bottom of groove tends to build up near to the opening of the groove, making the groove more localized. When evaporation-condensation is in effect, it smoothes the mass build-up at the groove opening, reduce the stress concentration at the bottom of the groove and the driving force for groove deepening. The shape change of the surface becomes more global. To have the same stress concentration at the bottom, the groove needs to be deeper than that generated by surface diffusion alone. Thus, when the mobility of evaporation-condensation increases, the time to form cusp becomes longer and the corresponding groove depth increases. But, according to the time normalization and the normalized cusp forming time shown in Table 3-I, when evaporation-condensation is in dominance, the time to form cusp decreases when the mobility of evaporation-condensation increases. Figure 3-14 shows the groove depth versus normalized time t_N^e, which is normalized by characteristic time τ_e, for evaporation-condensation dominant cases. The mobilities ratio range is $ml^2/M \geq 100$. Again, larger evaporation-condensation mobility corresponds to larger groove depth when cusp forms. The differences between the cases of $ml^2/M = 10^4$ and $ml^2/M = 10^6$ are negligible, indicating surface diffusion can be ignored when $ml^2/M > 10^4$.

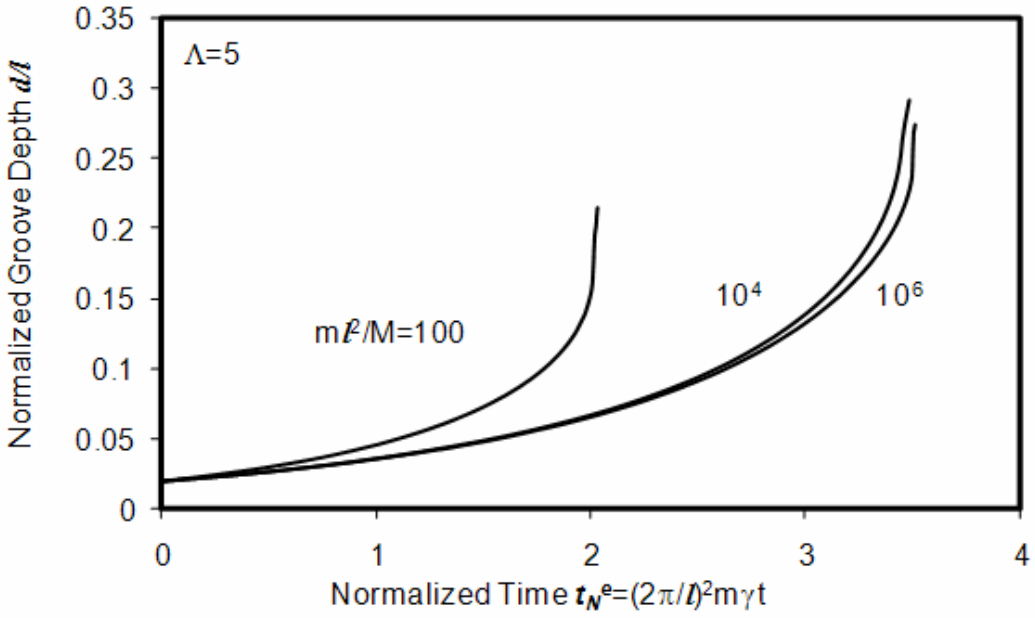

Figure 3-14: Groove depth vs. normalized time for grooving due to concurrent surface diffusion and evaporation/condensation. Evaporation/condensation dominant, $ml^2/M = 100, 10^4, 10^6$.

3.4 Dependence of Surface Evolution on Initial Profile

In this section, only consider surface evolution caused by surface diffusion has been considered. The qualitative results presented in this section also hold for evaporation-condensation cases.

3.4.1 Saddle Point

As shown in equation (3.19), after discretization, surface evolution is governed by a set of non-linear ordinary differential equations. As a dynamical system, its phase space is formed by

all its generalized coordinates. As pointed out by Yu [57], the state of a stressed flat surface is a saddle point in the phase space formed by all the surface configurations.

A residually stressed flat surface is a steady state since it remains flat if there is no fluctuation or external perturbation. However, from linear instability analysis, one knows that it is not a stable energy minimum state since the surface may groove with very small perturbation. Of course, it is not an energy maximum state, either. Imagine there is a small crack on the surface. Compare with flat surface under same remote stress, the extra surface energy in the cracked surface is proportional to the crack length, a, while the strain energy difference is proportional to the square of the crack length, a^2. Obviously, there is competition between the surface energy and strain energy. Thus, if the crack is small enough, the free energy of the surface with crack is larger than that of a flat surface; whereas, the free energy of the surface with crack is less than that of a flat surface.

Figure 3-15 [57] shows a two dimensional phase diagram, used to illustrate some general features of a system evolving around a saddle point. In the figure, $\dot{x}_1 = \lambda_1 x_1$, $\dot{x}_2 = \lambda_2 x_2$ with

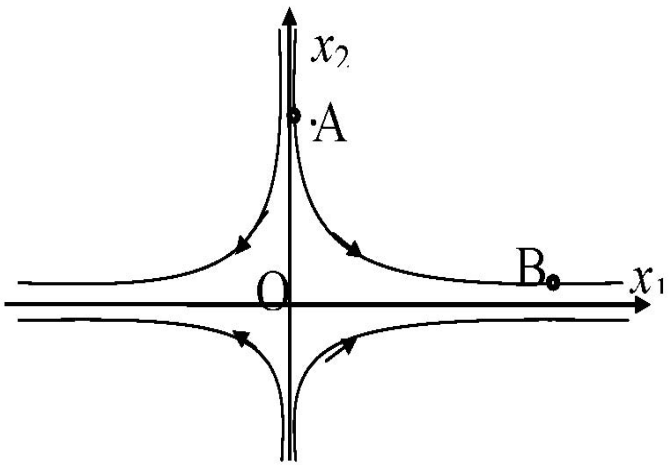

Figure 3-15: A saddle point in a 2D dynamical system. Yu [57]

$\lambda_1 > 0$ and $\lambda_2 < 0$. O is the saddle point. If starting from the initial point A, the system first approaches the saddle point, and the distance to the point O decreases; but, when it passes certain point, the distance to the saddle point increases again, and the system is turned away from the point O. If the system starts from point B, it is turned away from O immediately, and the distance to the point O increases monotonically. Let r be the distance to the point O, giving

$$dr^2/dt = 2(\lambda_1 x_1^2 + \lambda_2 x_2^2) \tag{3.26}$$

The system evolves very slowly when its trajectory in phase space is close to the saddle point, thus the evolution path could spend very long time in the neighborhood of the saddle point O.

This section shows that the morphology evolution of a stressed surface due to surface diffusion has the above general feature of a saddle point, explore the dependence of morphology evolution on the initial state of surface and discuss the implications in morphology control. Similar study has been done for crack nucleation from a single notch due to stress dependent reaction [57]. In that study, solid surface was represented by a family of curves using a complex conformal mapping. The kinetic pathway was thus limited to some specific group of curves. In this study, only surface diffusion is considered, a more general method, finite element method, which can describe any surface shape, is used, and thus the general conclusion derived from lower dimensional models for surface reaction [57] is proved that it still holds for surface diffusion case.

3.4.2 Evolution Possibilities with Initial Crack on Surface

Figure 3-7 shows that for a given stress level, when wavelength is large enough, making the loading parameter $\Lambda > \pi$, a sinusoidal perturbation grows and finally surface forms cusps. For a period infinity surface, one can always find a wave length l make loading level, Λ, greater than the critical value π. What will happen if there are sharp cracks on the surface in the beginning

and the surface is subsequently annealed? Will the stress concentration near crack facilitate surface diffusion and further deepen the cracks or the cracks be healed due to annealing?

From elastic fracture mechanics, when energy release rate of a crack is larger than fracture toughness, the crack will propagate. Under annealing, a crack with energy release rate smaller than fracture toughness can be partially healed, driven by the reduction of surface energy.

Consider a surface with periodically aligned surface cracks of same size a (See Figure 3-16). The distance between two neighboring cracks is l. If $a > 3l/14$, the energy release rate is about $\sigma^2 l/\overline{E}$ [102]. The fracture toughness for brittle material is 2γ. When the crack size $a > 3l/14$, the critical normalized load for crack propagation is $\Lambda_C \equiv (\sigma^2 l/\overline{E}\gamma)_C = 2$, lower than π, which is the critical normalized load for inducing surface instability from a flat surface. Hence, for $a > 3l/14$, any load that can induce surface instability can drive the cracks propagating. Even $\Lambda < \pi$, since the critical normalized load is $\Lambda_c = 2$, the crack still will propagate till fracture if $\Lambda > \Lambda_c \equiv 2$. If $\Lambda < \Lambda_c$, for this periodically aligned infinity surface, the crack will heal at the

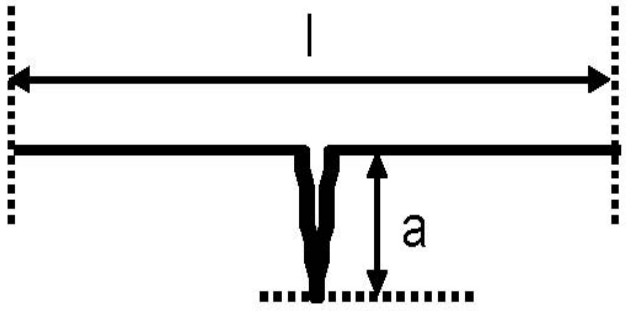

Figure 3-16: a surface with periodically aligned surface cracks of same size *a*

beginning, then grow with larger period length which makes the adjusted normalized load $\Lambda' > \Lambda_c$. When $a < 3l/14$, the energy release rate at crack tip is about $3 \sim 4\sigma^2 a/\overline{E}$ [102], which is independent of the period length l. Let's adopt the lower end of the energy release rate range as the critical value and note $\Lambda^a = \sigma^2 a / E\gamma$. Thus, the critical load is $\Lambda_c^a = 2/3$. Obviously, the crack will propagate till fracture when $\Lambda^a > \Lambda_c^a \equiv 2/3$. When $\Lambda^a < \Lambda_c^a$ and $\Lambda > \pi$, the cracks will heal at the beginning, then grow with same period length. When $\Lambda^a < \Lambda_c^a$ and $\Lambda < \pi$, the cracks will heal at the beginning, then grow with larger period length. Generally, the cracks will always grow either with the same period length when the load is big enough or with a larger period length when the load is relative small; either grow immediately or heal firstly and then grow. In the following, the case in which the cracks heal first and then grow with same period length is focused on.

3.4.3 Surface Profile Evolution with Initial Crack

Always, one could find a load that satisfies, $\Lambda^a < 2/3$ and $\Lambda > \pi$, so that the cracks could be healed at the beginning under surface diffusion, according to Griffith fracture theory, but it will not evolve back into perfectly flat surface, according to linear stability analysis. How will the surface evolve?

Figure 3-17 shows surface profile evolution with initial crack size, $a/l = 0.1$ and $\Lambda = 5$. Thus, $\Lambda^a = 0.5$. Since the initial energy release rate is smaller than the fracture toughness 2γ, the crack tip recedes and the crack is healed in the beginning due to annealing induced surface diffusion. The groove depth drastically decreases, the surface becomes smoother and slightly curved, and however, it does not return to and keep at a flat surface since it is unstable when $\Lambda > \pi$. The surface stays near flat for quite a long time, due to small driving force close to the

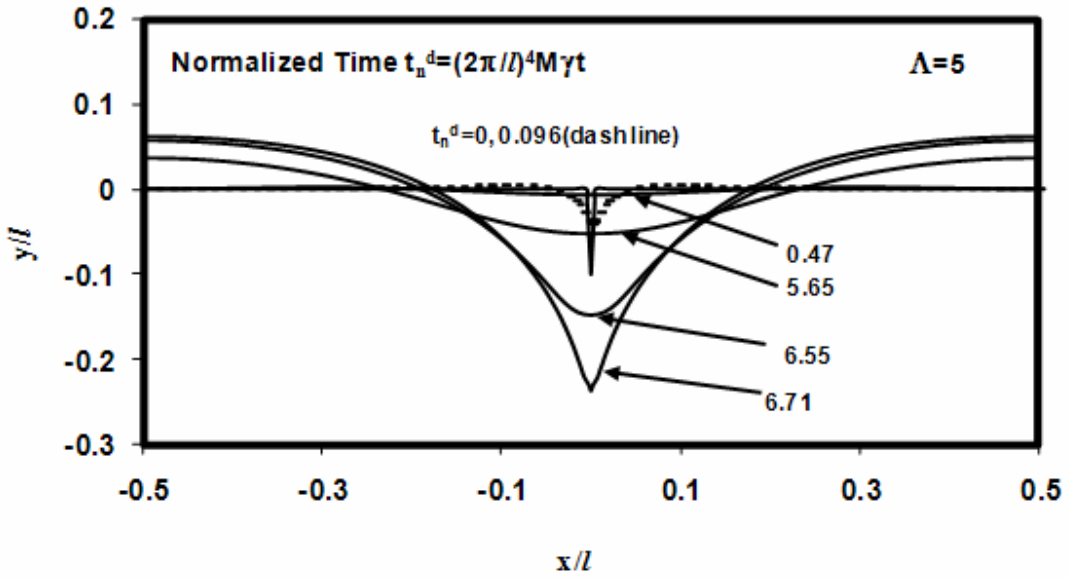

Figure 3-17: Surface profiles of morphology evolution from initially cracked surface (Λ= 5, *a/l*=0.1 under surface diffusion).

so called saddle point. Then a new type of surface groove, with smooth varying surface profile, slowly develops. The groove depth gradually increases then. The bottom of the groove gradually re-sharpens, and eventually cusp with sharp tip forms. The overall surface profile, when cusp forms, looks much different from the beginning, though both having sharp tip at the root of groove or crack. The evolution of the surface is analogy to the initial point A in the dynamical system in Figure 3-16. It first approaches steady state saddle point, the flat surface state, evolves slowly near it, and eventually is driven away. Comparing two surface profiles at $t_n^d = 0.096$ and $t_n^d = 0.47$, the latter one, almost flat, is smoother than the first one, however, it takes shorter time to form surface cusp.

Figure 3-18 shows groove depth versus normalized time for surfaces evolution starting from four different initial surface configurations, all under the same normalized load, $\Lambda = 5$. The dashed line corresponds to surface starting from a small initial sinusoidal perturbation, $d_0/l = 0.02$, copied from Figure 3-7. The other three cases, in solid lines, start from surfaces with either notch or crack, having initial groove depth $d_0/l = 0.04$. Though the surface with small sinusoidal perturbation looks much smoother than the other three cases, and has smallest initial groove depth, it takes shortest time for the film to form cusps. The groove depth increases monotonically, similar to the dynamical system in Figure 3-16 starting from initial point B. The surface is immediately driven away from flat surface state.

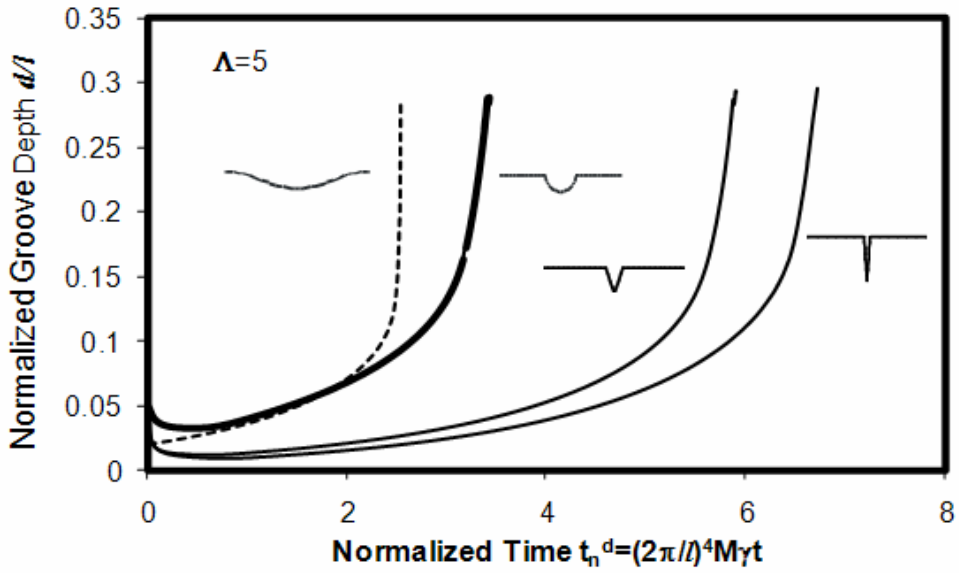

Figure 3-18: Groove depth vs. normalized time for surfaces evolving from different initial configurations (Λ= 5, under surface diffusion)

The evolution of surface starting from initial sharp or semicircle notch is similar to the one with initial surface crack. Groove depth decreases drastically in the beginning, stays near constant for some time, then gradually increases, until finally diverges in short time. Among four curves in Figure 3-18, the surface with initial surface crack takes longest time to form cusp, with initial sharp notch the next, followed by semicircle notch case, and the one which is very close to a perfectly flat surface takes the shortest time to form cusp. The results show that surface with localized surface defects or excessive surface area could delay the development of surface instability. All the three cases are analogy to the dynamical system in Figure 3-16 which starts from point A.

Chapter 4

4 Stress Relaxation of Thin Film due to Mass Diffusion

Still consider a two dimensional system, a residually stressed thin film with traction free surface on its substrate. Additionally, in this case, assume the thin film is combined of multi grains with uniform grain size and thickness. Figure 4-1 shows the schematics of stressed multi-grain thin film with free surface. The thin film is under remote stress σ which is generated by the mismatch strain between the thin film and its substrate. l is the grain size and h is the grain

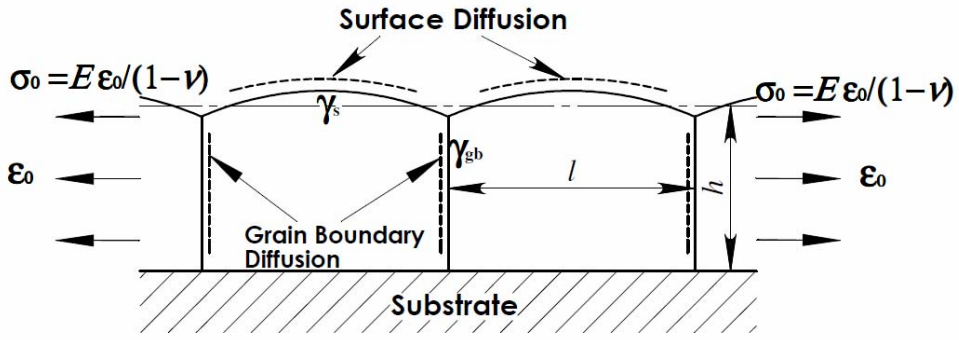

Figure 4-1: Schematic geometry of stressed thin film under surface and grain boundary diffusion.

thickness. γ_s and γ_{gb} are the surface energy and grain boundary energy, respectively. As mentioned in Chapter 1, the residual stress can be partially relaxed by several mechanisms such as cracking and/or delamination [59 - 62], dislocation [63, 64] and diffusional creeps [65 - 68]. Assume that, the mass transport along the free surface and grain boundary by diffusional progresses only, thus, there are two ways to relax stress in thin film. One is by the change of surface profile due to surface diffusion or reaction, as demonstrated in our previous simulation [Chapter 3 and Ref. 69]. The other is by diffusion of mass into grain boundary from the free surface when the film is under tensile stress or out of grain boundary to free surface when the stress is compressive. The assumptions that there is no migration or sliding of grain boundary and the inserted mass at one grain boundary join the two neighboring grains evenly are adopted.

This chapter is arranged as following. Review the formulations and numerical implementation in the next section. Then, simulate the model problem, a strained thin film with initially flat free surface, to show surface morphology evolution and normal traction relaxation along the grain boundary. Focus on the effects of surface profile on stress relaxation by comparing the results of simulations under different surface-grain-boundary energy ratio. Finally, fit the experimental results by the simulation results and determine the surface and grain boundary diffusivities.

4.1 Formulations and Numerical Implementation

4.1.1 Weak Statement and Free Energy

Recall the general weak statement in three dimensions, equation (2.55). Consider only two mass transportation methods, surface diffusion and grain boundary diffusion involved in, and there's no migration of grain boundary, giving the weak statement,

$$\int \left\{ \frac{\mathbf{J}\cdot\delta\mathbf{I}}{M_s} + \frac{(v_n + \nabla\cdot\mathbf{J})[\delta r_n + \nabla\cdot(\delta\mathbf{I})]}{m_s} \right\} dA + \int \left\{ \frac{\mathbf{J}\cdot\delta\mathbf{I}}{M_{gb}} \right\} dA = -\delta G \qquad \textbf{(4.1)}$$

The integral of the first term extends over the free surface area and the integral of the second term extends over the grain boundary area. Using the same loading condition as that in Chapter 3, thus, in this half plane thin film problem, the two-dimensional version of weak statement becomes

$$\int \left\{ \frac{J\delta\mathbf{I}}{M_s} + \frac{(v_n + \partial J/\partial s)[\delta r_n + \partial(\delta\mathbf{I})/\partial s]}{m_s} \right\} ds + \int \frac{J\delta\mathbf{I}}{M_{gb}} ds = -\delta G \qquad \textbf{(4.2)}$$

The first term of the left side is combined of surface diffusion and evaporation-condensation, and the second term is for the grain boundary diffusion. Same as before, let the dimensionless group $m_s l_e / M_s$ be a very small number to make the evaporation-condensation process on the surface negligible. Also, choose the grain size l as the representative length l_e.

Consider this two dimensional system, a residually stressed thin film with traction free surface (see Figure 4-1), the total virtual free energy changes due to virtual motion caused by surface and grain boundary diffusion is

$$\delta G = \delta\left(\int_{Surface} \gamma_s ds \right) + \int_{surface} w\delta r_n ds + \delta\left(\int_{g.b.} \gamma_{gb} dy \right) + \int_{g.b.} w\delta[u_{gb}]dy - \int_{g.b.} \sigma_{gb}\,\delta[u_{gb}]dy \qquad \textbf{(4.3)}$$

where γ_s and γ_{gb} are surface tension and grain boundary tension, w the strain energy density, δr_n the virtual normal displacement of free surface, σ_{gb} the normal stress on grain boundary. When mass flows into grain boundary, the atoms at the original grain boundary are pushed to the two sides. Assume $[u_{gb}]$ the separation of the original grain boundary caused by the mass insertion and $\delta[u_{gb}]$ is the virtual separation due to the virtual mass insertion. From mass

conservation law, equation (2.20), one has $\delta[u_{gb}] = -\nabla \cdot \delta I_{gb}$, thus, equation (4.3) can be revised as

$$\delta G = \delta\left(\int_{Surface} \gamma_s ds\right) + \int_{surface} w\delta r_n ds + \delta\left(\int_{g.b.} \gamma_{gb} dy\right) - \int_{g.b.} w\nabla \cdot (\delta I_{gb}) dy + \int_{g.b.} \sigma_{gb} \nabla \cdot (\delta I_{gb}) dy \qquad \textbf{(4.4)}$$

The first four terms at the right hand of equation (4.4) are all due to free surface configuration and grain boundary change. Although there is no external work done by the load, there is still the fifth term which is the strain energy reduction due to the negative work done to the *original grain configuration* by mass insertion. Usually, $w << \sigma_{gb}$ at the grain boundary and the fourth term can be ignored.

The stress field associated with strain energy density w and the normal stress σ_{gb} on the grain boundary in equation (4.4) is still generated by pre-descript displacement on the grain boundary and solved by BEM [100, 101]. Use the same line element and finite element procedure as that in Chapter 3. But the viscosity matrix for grain boundary diffusion is not 7 x 7 but 3 x 3 matrix. The components of the element viscosity matrix for grain boundary is listed in Appendix E.

The algorithm is similar to our previous work [69] and last chapter (see Figure 3-6). The difference is that there is not only the surface configuration but also the boundary condition changes after each small time step. See Figure 4-2 and imagine at the beginning of a new time step in a simulation. The current surface configuration was solved from last time step. Solve the stress field under given boundary conditions and current geometry firstly. Using the current generalized coordinates, viscosity matrix $\mathbf{H}$ and force vector f in equation (3.19) are calculated. By solving equation (3.19), nodal velocities, which are integrated over a small time step using Runge-Kuta method to get surface configuration after one time step are obtained. Besides, a new

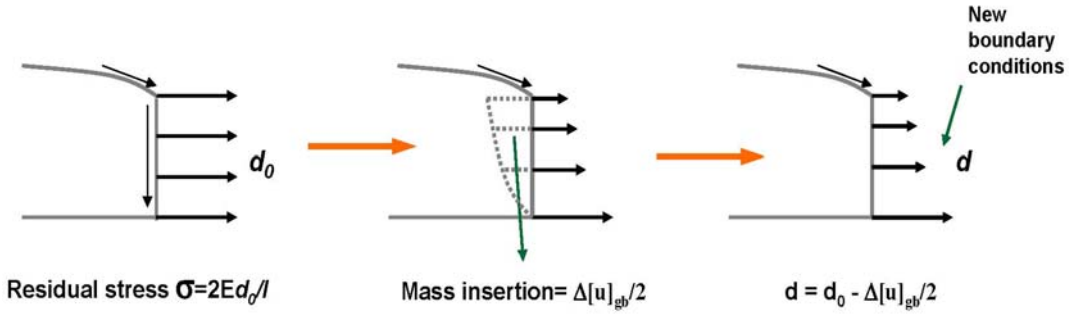

Figure 4-2: a) Original boundary conditions b) Mass insertion along grain boundary c) New Grain boundary for next time step

boundary condition for the next time step is obtained. Since the mass inserting into the grain boundary, there is an inelastic deformation along the grain boundary which has contribution to the pre-described displacement on grain boundary. Repeat the procedure to evolve the surface and stress relaxation.

4.1.2 Natural boundary conditions and controlling parameters

In Ref. [76, 77], the continuity equations at the junction of grain boundary and surface are needed to solve the differential equations. In the current integral formulation, such conditions are automatically satisfied. Using mass conservation law, $\delta u_n = -\nabla \cdot \delta I_s$ and geometric relation, $\delta(dA) = \kappa \delta u_n dA$, in which κ is surface curvature, then integrating by part, equation (4.4) can be rewritten as

$$\delta G = \int_{\partial\Omega} \nabla \cdot (w + \gamma_s \kappa) \delta I_s dA - \int_{g.b.} \nabla \cdot \sigma_n \delta I_{gb} dA + (2\gamma_s \cos\frac{\theta}{2} - \gamma_b) \delta u_i^t + (\gamma_s \kappa^t + \sigma_n^t) \delta I_{gb}^t \qquad \textbf{(4.5)}$$

in which δu_i^t is the virtual displacement at the triple junction and δI_{gb}^t is the virtual mass displacement in or out of the triple junction. Combine the above equation with the weak

statement, equation (4.2), and use the fact that all the virtual variables in the above equations are arbitrary and independent, the differential equations used in Ref. [76, 77] and the boundary conditions at the triple junction can be derived,

$$2\gamma_s \cos\frac{\theta}{2} - \gamma_{gb} = 0 \tag{4.6}$$

$$\gamma_s \kappa^t + \sigma_n^t = 0 \tag{4.7}$$

These two equations show that in our integral formulation, local equilibrium condition, equation (4.6), and the continuity condition of chemical potential, equation (4.7), are natural boundary conditions and do not need be manually prescribed in our integral formulation.

Combining weak statement, equation (4.2), and free energy variation, equation (4.4), and normalizing everything by the grain size l, grain boundary energy γ_{gb} and the plane modulus $\overline{E}$, one can get the following dimensionless controlling parameters: surface/grain-boundary energy ratio $\bar{\gamma} = \gamma_s / \gamma_{gb}$, initial grain thickness/size ratio $\bar{h}_0 = h_0 / l$, initial normalied stress level $\bar{\sigma}_0 = \sigma_0 l / \gamma_{gb}$, and initial normalized strain energy $\bar{w}_0 = \sigma_0^2 l / \overline{E}\gamma_{gb}$. Where γ_s, h_0 and σ_0 are surface energy, initial grain boundary height (grain thickness) and initial normal stress along grain boundary, respectively. Also, another parameter of mobility ratio $\Delta = M_s / M_{gb}$ is used to determine the time scale.

Finding the characteristic time is very important in time normalization and determining the size of each time step in numerical simulation. Let's first consider two limiting cases: case one, surface diffusion is very fast, so that stress relaxation is limited by the rate of grain boundary diffusion; and case two, grain boundary diffusion is very fast, so that stress relaxation is limited by the transport of mass along the surface. From simple analysis, it can be shown that the characteristic time for the first case is

$$\tau_{gb} = \frac{4h_0^2 L}{\pi^2 M_{gb} \overline{E}} \tag{4.8}$$

and that of the second case is

$$\tau_s = \frac{h_0 L^2}{\pi^2 M_S \overline{E}} \tag{4.9}$$

Each characteristic time is directly related to the mobility of the rate limiting process. For the convenience of comparing with the previously published results by others [77], numerical pre-factors are included.

4.2 Stress Relaxation and Surface Morphology Evolution

4.2.1 Free Surface Cases

In the following, the results from the simulation of stress relaxation and surface evolution on a residually stressed thin film are presented. The boundary conditions used to solve the surface evolution are given in Figure 4-3; mainly, the horizontal displacement along the grain boundary

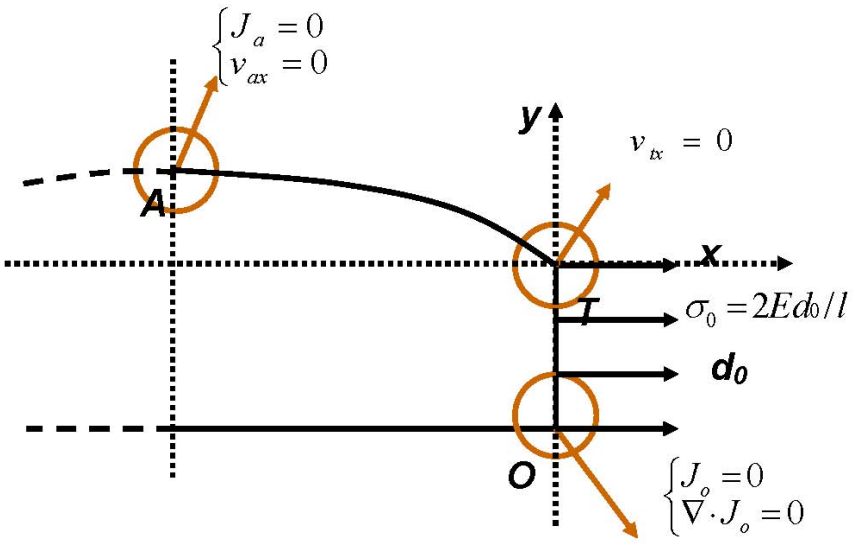

Figure 4-3: Boundary Conditions used to solve the surface evolution.

is prescribed. Assume the initial in-plain strain mismatch between the substrate and film is ε_0. It corresponds to an in-plane biaxial stress $\sigma_0 = E\varepsilon_0/(1-\nu)$. For simplicity of discussion, assume the substrate has the same elastic constants as the thin film. In the simulation, quadratic elements in BEM for stress calculation and linear element in FEM for calculation of surface morphology evolution and grain boundary diffusion are used.

In Figure 4-4, the normalized average normal stresses $\overline{\sigma}_{gb}/\sigma_0$ along the grain boundary are plotted as a function of normalized time $t_n = t/\tau_{gb}$ at several different values of mobility ratio Δ. $\overline{\sigma}$ is calculated by the following equation,

$$\overline{\sigma}_{gb} = \frac{1}{h}\int_0^h \sigma_{gb}\, dy \qquad \textbf{(4.10)}$$

where h is the current height of the grain boundary. Figure 4-4 shows that, all the curves for mobility ratio $\Delta \geq 0.5$ are almost the same. Since large Δ means relatively fast surface diffusion, the results indicates that the stress relaxation is limited by grain boundary diffusion when mobility ratio $\Delta \geq 0.5$. These can be called as grain boundary diffusion controlled processes. In Figure 4-5, time is normalized by another time scale τ_s, defined in equation (4.9). The dash line is from Zhang and Gao [76] for the second limiting case in which the grain boundary diffusion is so fast that once mass is inserted into grain boundary it will be immediately redistributed to reach minimum potential energy. Figure 4-5 shows that for $\Delta \leq 0.01$, the stress relaxation is limited by surface diffusion. Obviously, surface diffusion controlled process occurs when $\Delta \leq 0.01$. Combine Figure 4-4 and Figure 4-5, concluding that surface diffusion and grain boundary diffusion are fully coupled for $0.01 < \Delta < 0.5$. Other parameters in these cases are $\overline{\gamma} = 1$, $\overline{h} = 1$, $\overline{\sigma}_0 = 100$ and $\overline{w}_0 = 0.01$.

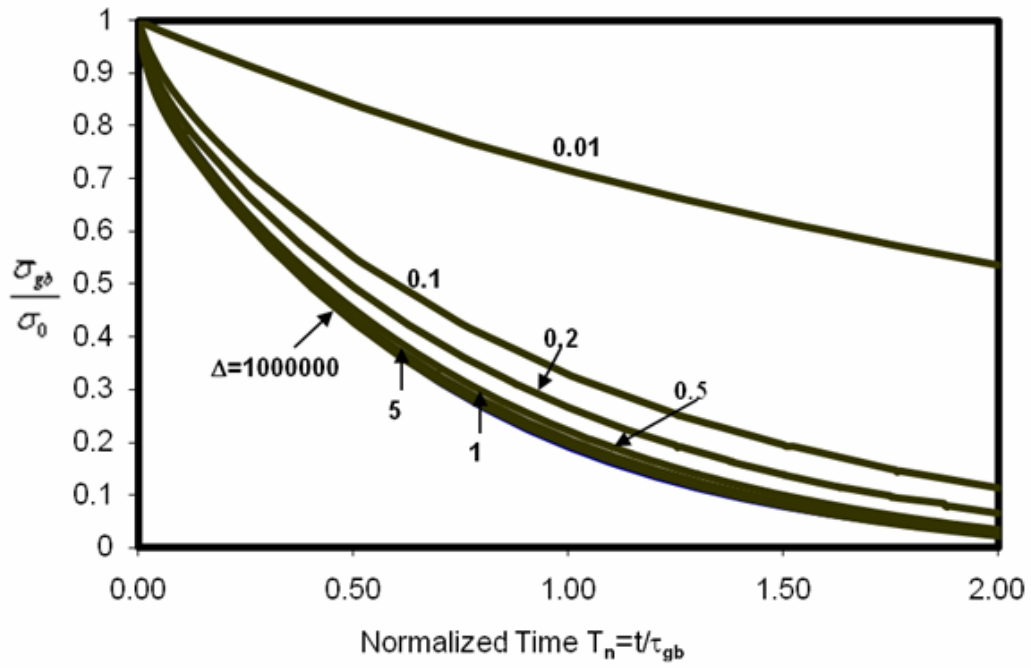

Figure 4-5: Stress relaxation of thin film with free surface under several different mobility ratios. Time normalized by τ_{gb} which defined in Equ. (4.8).

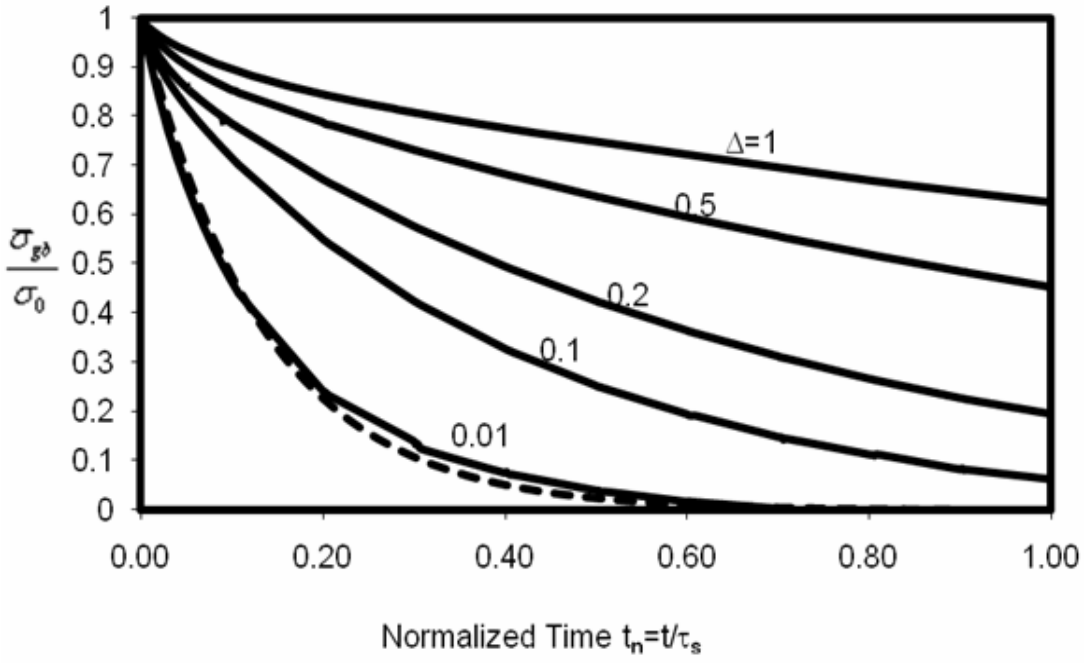

Figure 4-5: Stress relaxation of thin film with free surface under several different mobility ratios. Time normalized by τ_{gb} which defined in Equ. (4.9).

Figure 4-6, Figure 4-7 and Figure 4-8 show us the evolution of surface profiles for three different mobility ratios. When stress relaxation is limited by grain boundary diffusion, surface changes shape much faster than stress relaxation, as shown in Figure 4-6 and Figure 4-4; and when stress relaxation is limited by surface diffusion, relaxation and surface grooving occur at about the same speed, as shown in Figure 4-8 and Figure 4-5. Although cusps form at the triple point, there's no stress singularity since the self-satisfied chemical potential continuity relation at the triple point.

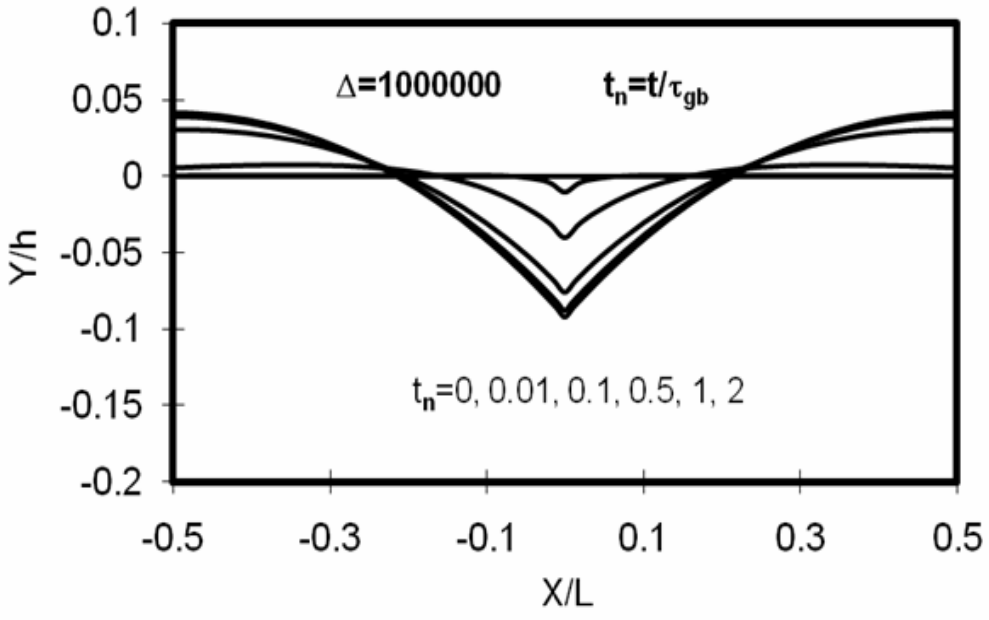

Figure 4-6: Surface profile of morphology evolution of the thin film with free surface. Surface diffusion limited process ($\Delta = 1000000$)

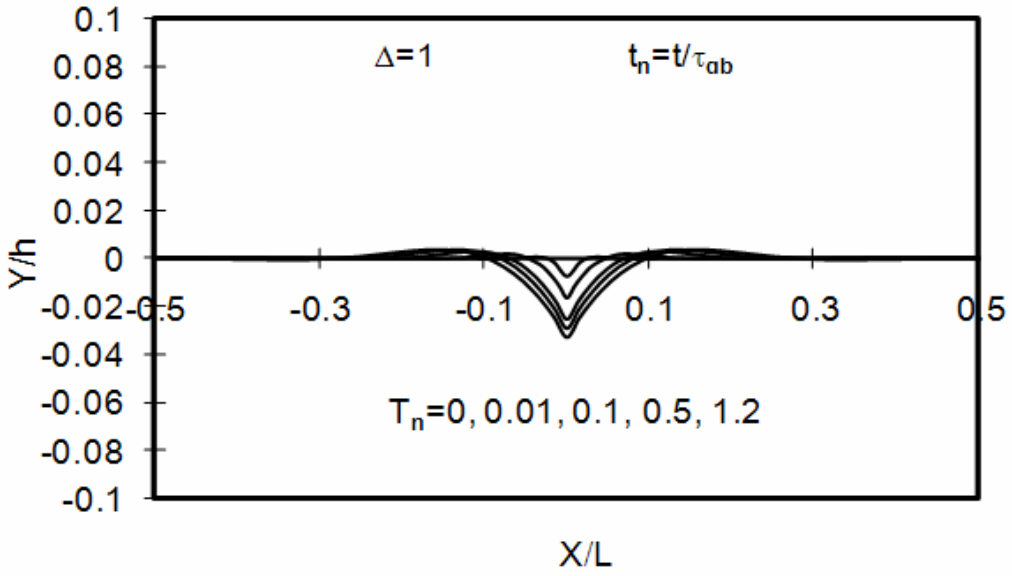

Figure 4-8: Surface Profile of morphology evolution of the thin film with free surface. Comparable surface diffusion and grain boundary diffusion. ($\Delta = 1$).

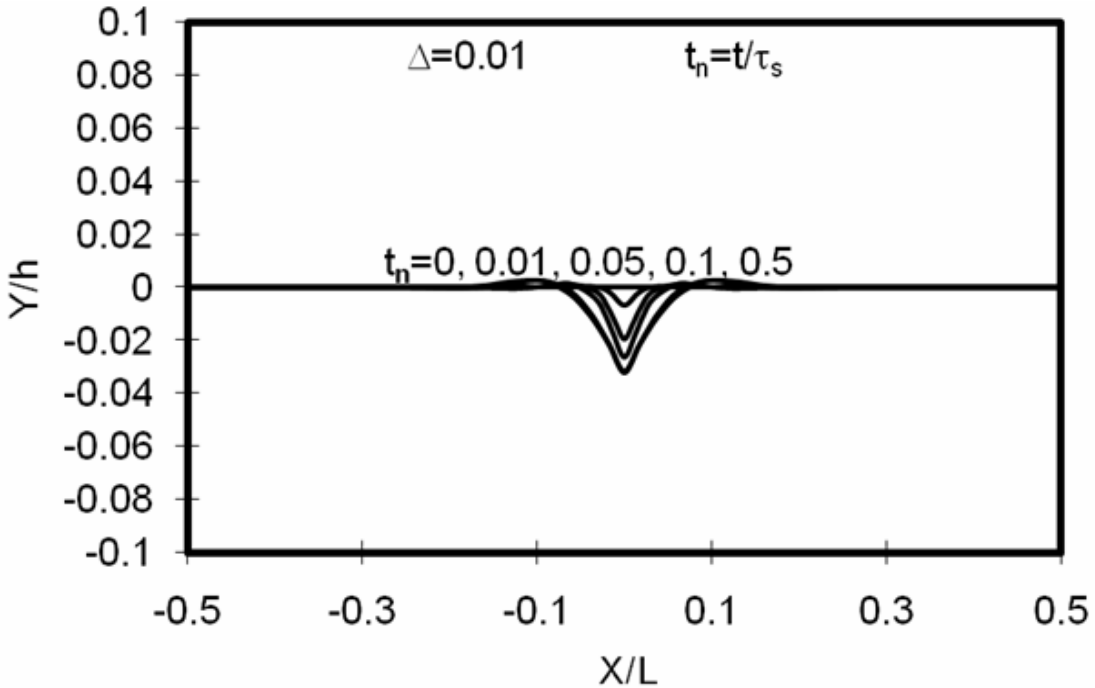

Figure 4-8: Surface profile of morphology evolution of the thin film with free surface. Grain boundary diffusion limited process ($\Delta = 0.01$).

4.2.2 Capped Surface Cases

When a metal thin film is covered by a brittle film such as an oxidation layer, the film/film interface may keep relatively flat. The residual stress in metal could still be reduced by mass diffusion along the film/film interface. Huang *et al.* [77] studied the stress relaxation of capped Cu thin film by assuming that the film-cap interface remains flat all the time and the mass transport induces a locally nonzero normal stress at the interface. Gao *et al.* [75] studied the constrained grain boundary diffusion by assuming surface tension is very large so that the surface of the film remains perfectly flat during the diffusion process. Assume that the top layer is much thinner than that of the thin film. The stress field is solved the same way as before. Similar to Gao *et al.* [75], the thin top layer is modeled as a membrane with large surface tension ($\bar{\gamma} = 1000$) to simplify the problem (see Figure 4-9). The difference is that surface diffusion is

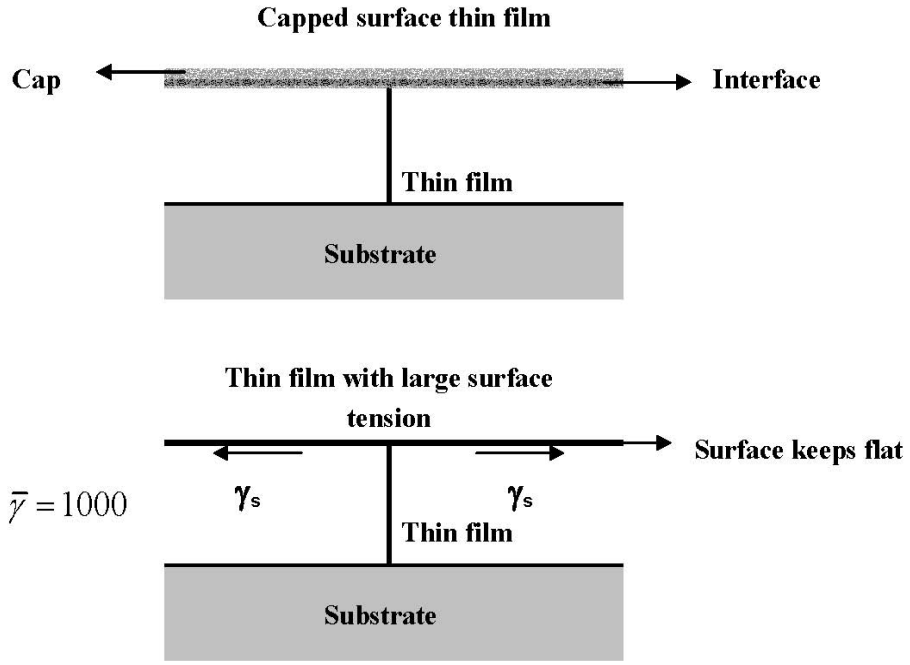

Figure 4-9: Equivalent capped surface of the thin film

ignored in Gao's work but surface and grain boundary diffusion are coupled together in this work. M_s is still used to denote the equivalent interface diffusion mobility and split these cases into two parts by the separating point $\Delta = 1$ so that the results can be simply compare with the results in free surface cases. Of course, other effect parameters are the same as those in the free surface cases, $\bar{h} = 1$, $\bar{\sigma}_0 = 100$ and $\bar{w}_0 = 0.01$.

In Figure 4-10 and Figure 4-11, the stress relaxation as a function of normalized time for the cases with capped surface but different mobility ratio are plotted. In Figure 4-10, stress relaxation process is mainly limited by grain boundary diffusion, and time is normalized by τ_{gb}; similarly, in Figure 4-11, the whole process is mainly limited by interface diffusion, and time is normalized by τ_S. Compared with the results in free surface cases (Figure 4-4 and Figure 4-5), the stress relaxation is much more sensitive to the interface mobility for capped thin films than it

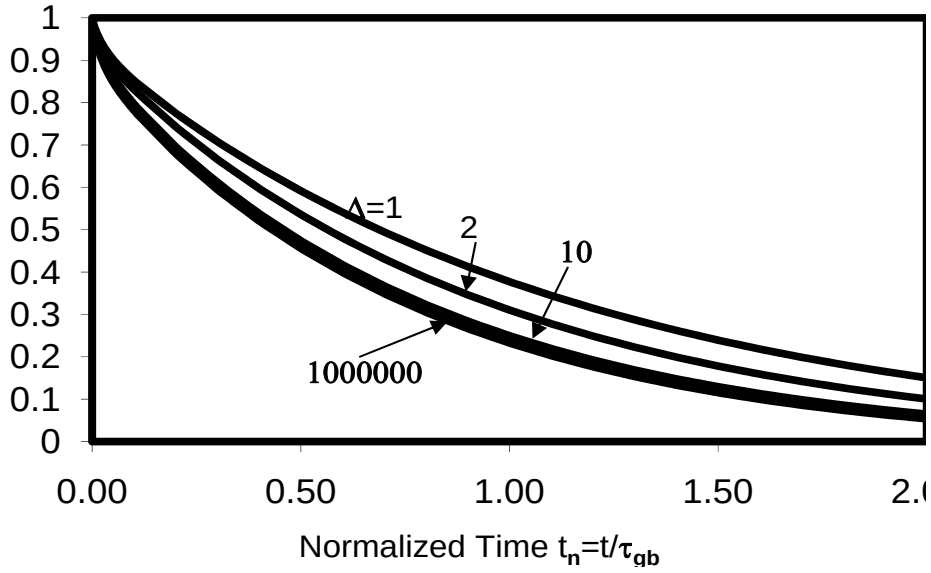

Figure 4-10: Stress relaxation of thin film with capped surface under several different mobility ratios. Time normalized by τ_{gb} which defined in equation (4.8).

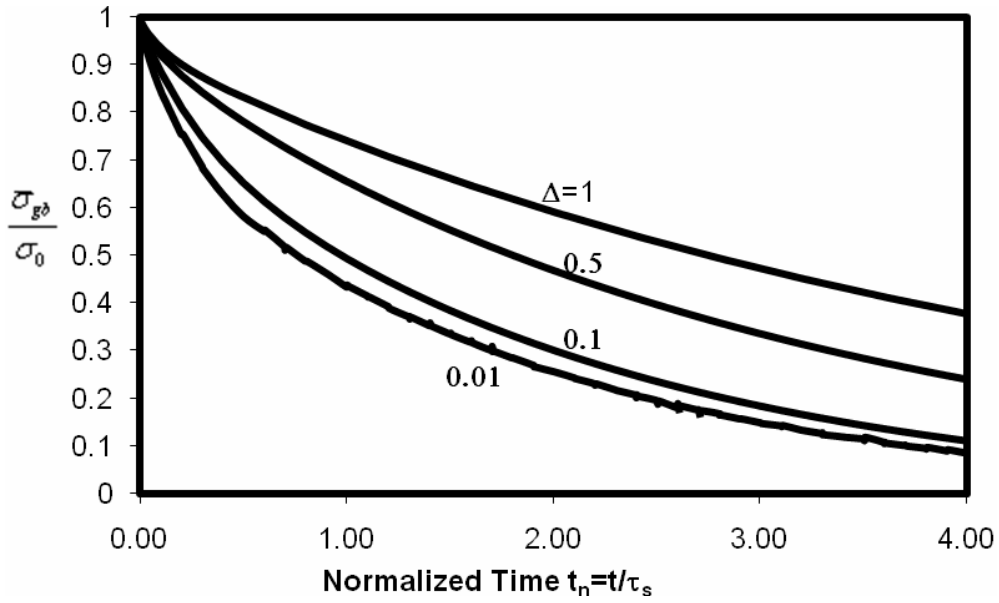

Figure 4-11: Stress relaxation of thin film with capped surface under several different mobility ratios. Time normalized by τ_s which defined in equation (4.9)

is to the surface mobility for the thin films with free surface. On the other hand, the stress relaxation is less sensitive to the grain boundary mobility for capped thin films than the thin films with free surface. Simulation results also show that when mobility ration $0.1 < \Delta < 10$, interface diffusion and grain boundary diffusion are fully coupled and outside that range, stress relaxation is almost independent of the mobility ratio. In these processes, the surface keeps flat and its position goes down evenly because of the initial tensile stress in the thin film and the relocating of mass from surface to grain boundary.

4.3 Effect of controlling parameters

4.3.1 Effect of surface energy/grain boundary energy ratio ($\bar{\gamma}$)

Stress field depends on loading level and surface profile. The latter is affected by the dihedral angle at the triple junction, junction of grain boundary and free surface. According to equation (4.6), the dihedral angle is determined by $\bar{\gamma}$, the ratio of surface energy and grain boundary energy. In this section, the effect of $\bar{\gamma}$ is studied. In the previous study on stress relaxation with capped surface case, surface with very large surface tension is used to model the capped layer. This section checks beyond which point of $\bar{\gamma}$ the results are insensitive to $\bar{\gamma}$.

Under different values of $\bar{\gamma}$, Figure 4-12, Figure 4-13 and Figure 4-14 show the normal stress relaxation along grain boundary for cases with very large surface diffusion mobility, comparable surface and grain boundary diffusion mobilities and very large grain boundary

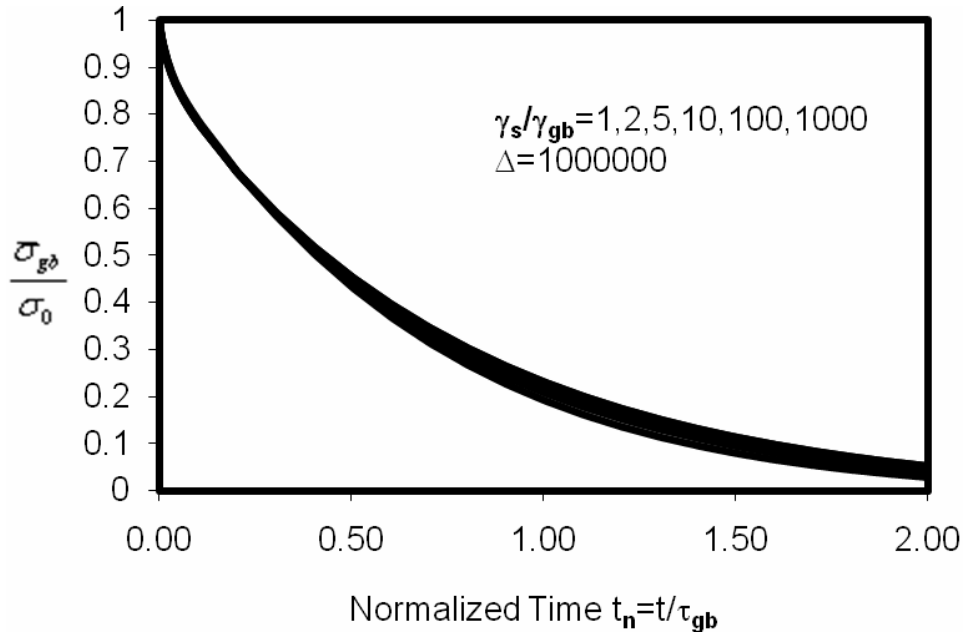

Figure 4-12: Stress relaxation of thin film when surface diffusion is infinity ($\Delta = 1000000$)

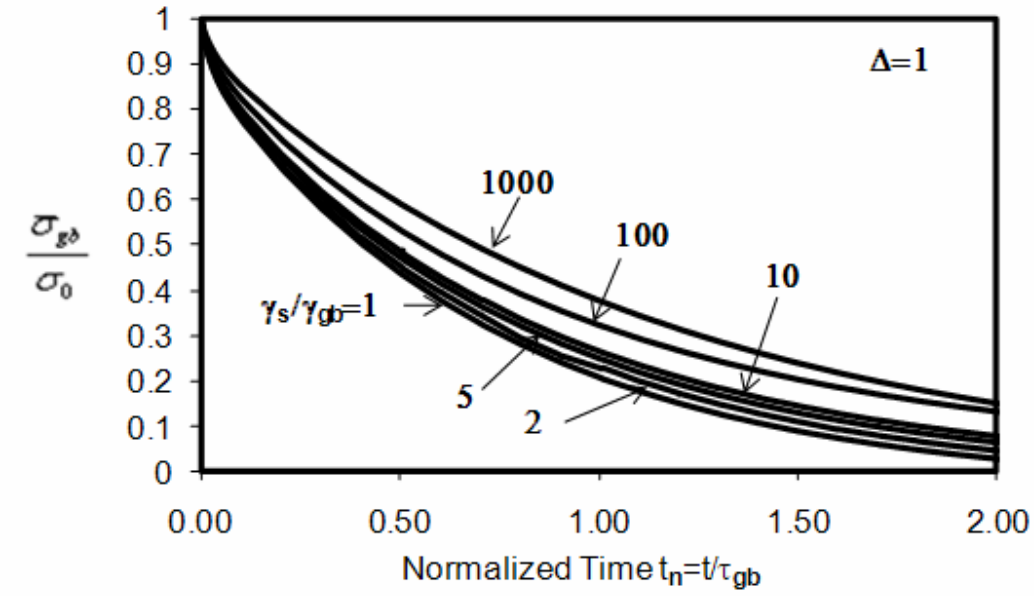

Figure 4-14: Stress relaxation of thin film when surface and grain boundary diffusion are comparable ($\Delta = 1$)

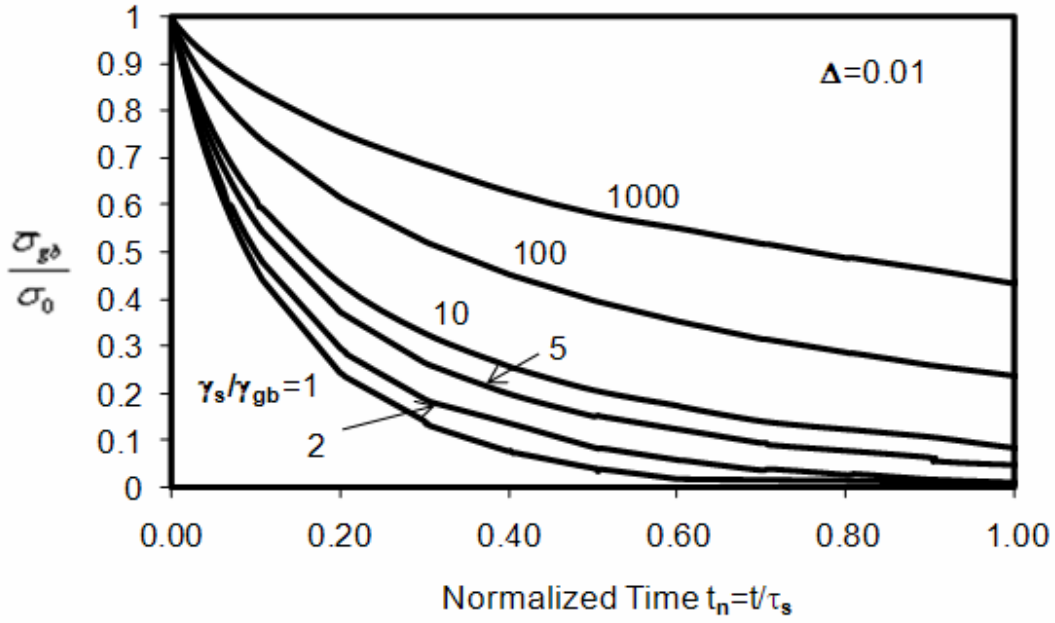

Figure 4-14: Stress relaxation of thin film when grain boundary diffusion is infinity ($\Delta = 0.01$)

diffusion mobility, respectively. When the stress relaxation process is limited by the rate of grain boundary diffusion, the stress relaxation curves for different values of $\bar{\gamma}$ are very close (Figure 4-12); when surface diffusion and grain boundary diffusion become comparable (Figure 4-13), stress relaxation is slightly delayed when $\bar{\gamma}$ increases; and when stress relaxation is limited by the rate of surface diffusion, stress relaxation is significantly slowed down by the increase of $\bar{\gamma}$, i.e. the increase of dihedral angle (Figure 4-14). The results can be understood as following. Large $\bar{\gamma}$ corresponds to larger dihedral angle, relatively smaller stress concentration, and smaller surface curvature κ^t at the triple point according to equation (4.7), so the driving force for surface diffusion becomes smaller and slows down the stress relaxation if it is limited by surface diffusion.

In Figure 4-15, Figure 4-16 and Figure 4-17, the equilibrium surface profile state under different surface/grain boundary mobility ratio are plotted. Though the dihedral angle is not

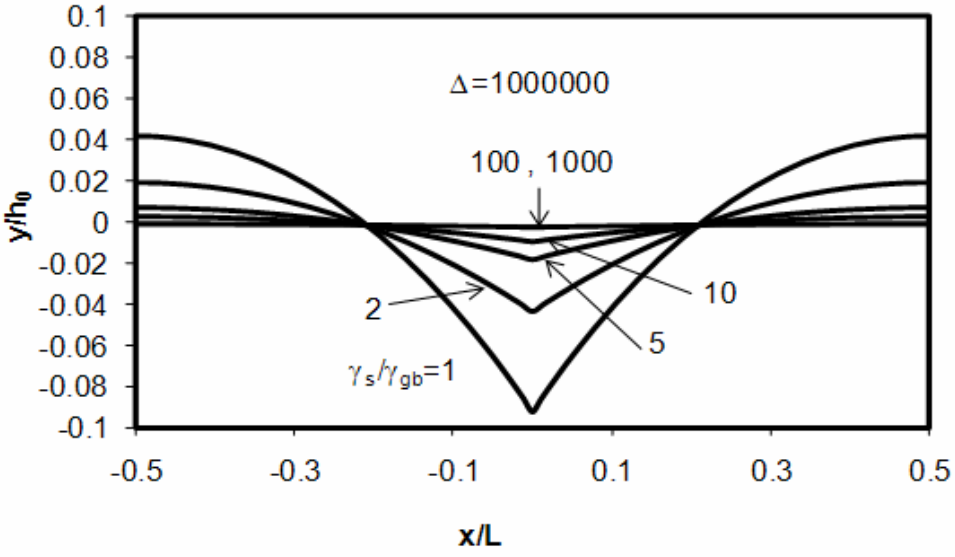

Figure 4-15 : Surface profiles at equilibrium state when surface diffusion is infinity

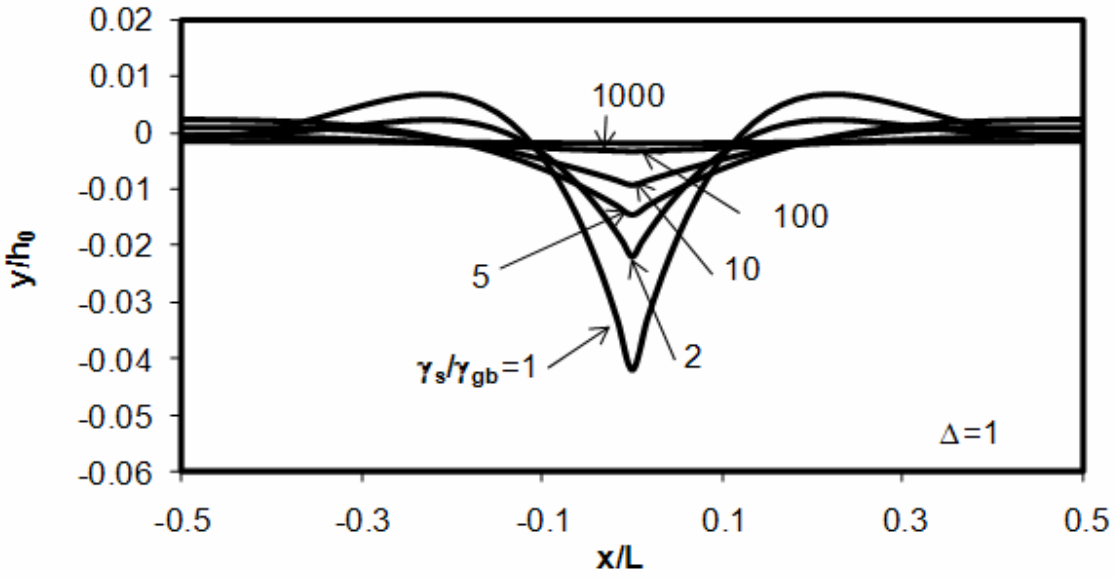

Figure 4-17: Surface profiles at equilibrium state when surface and grain boundary diffusion are comparable ($\Delta = 1$)

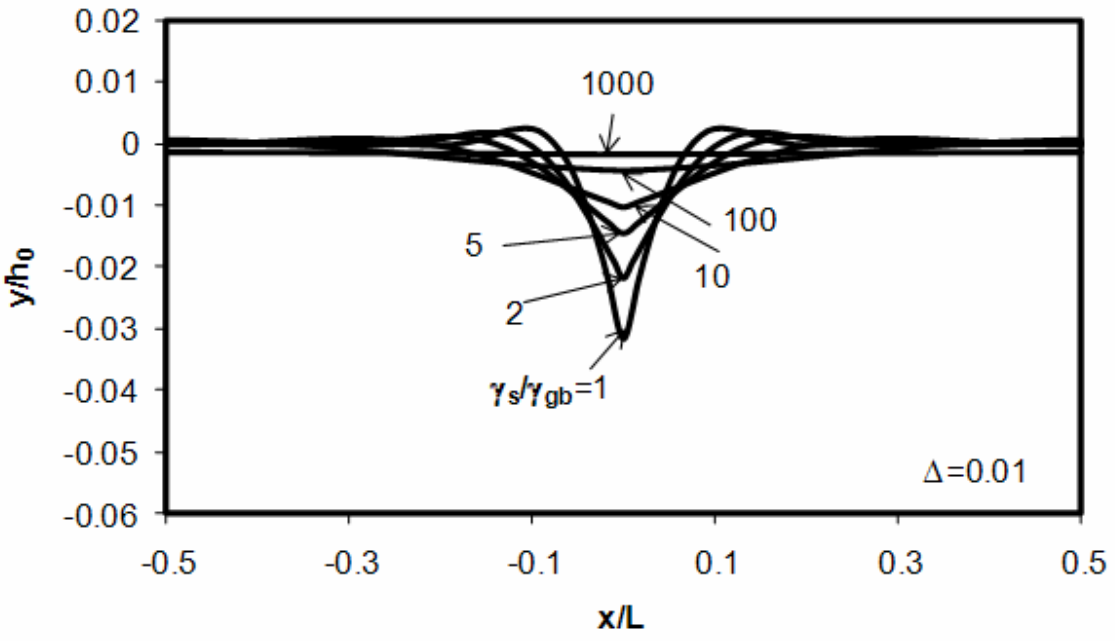

Figure 4-17: Surface profiles at equilibrium state when Grain boundary diffusion is in dominant ($\Delta = 0.01$)

prescribed, it can be verified that the dihedral angle in our simulation satisfies equation (4.6). Other parameters in these cases are $\bar{h} = 1$, $\bar{\sigma}_0 = 100$ and $\bar{w}_0 = 0.01$.

4.3.2 Effects of initial normal stress σ_0

There are two dimensionless parameters involving initial stress, $\bar{\sigma}_0 = \sigma_0 l / \gamma_{gb}$ and $\bar{w}_0 = \sigma_0^2 l / \bar{E}\gamma_{gb}$. In grain boundary diffusion, flux is proportional to the normal stress and the effect of $\bar{w}_0$ can be ignored. So if normalize stress by the initial stress σ_0, when surface diffusion is relatively fast and the stress relaxation is limited by grain boundary diffusion, stress relaxation curve should be independent of initial stress. On the other hand, surface diffusion is greatly affected by the gradient of strain energy density along the surface, so when surface diffusion is limiting the stress relaxation, the parameter $\bar{w}_0 = \sigma_0^2 l / \bar{E}\gamma_{gb}$ is expected to show some noticeable effect. These predictions are verified in Figure 4-18, 4-19 and 4-20 which show

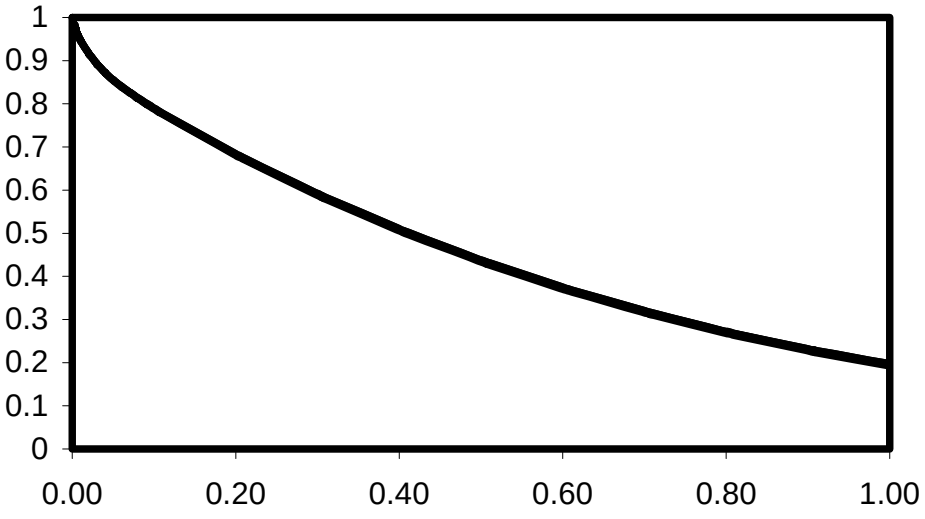

Figure 4-18: Stress relaxation of thin film with free surface under several different initial normal stresses along grain boundary. ($\Delta = 1000000$)

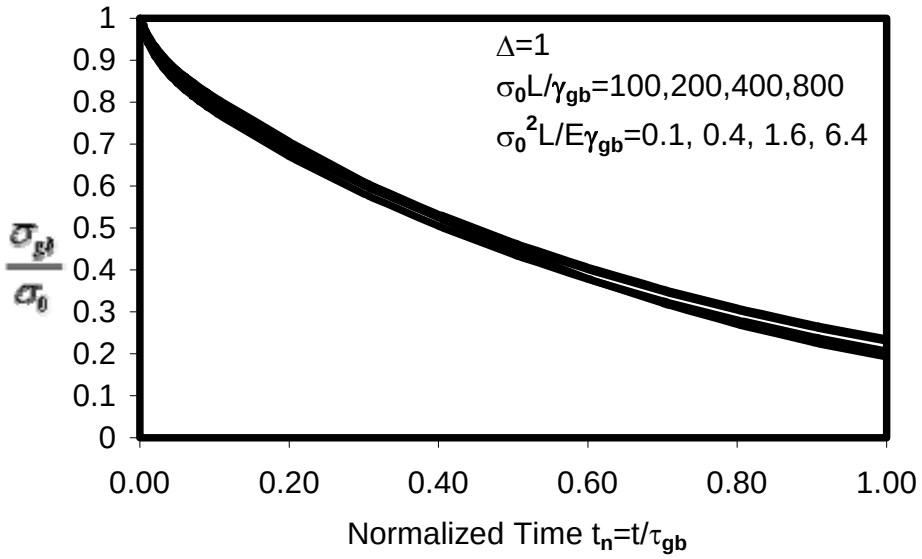

Figure 4-20: Stress relaxation of thin film with free surface under several different initial normal stresses along grain boundary. Surface and grain boundary diffusion are comparable ($\Delta = 1$).

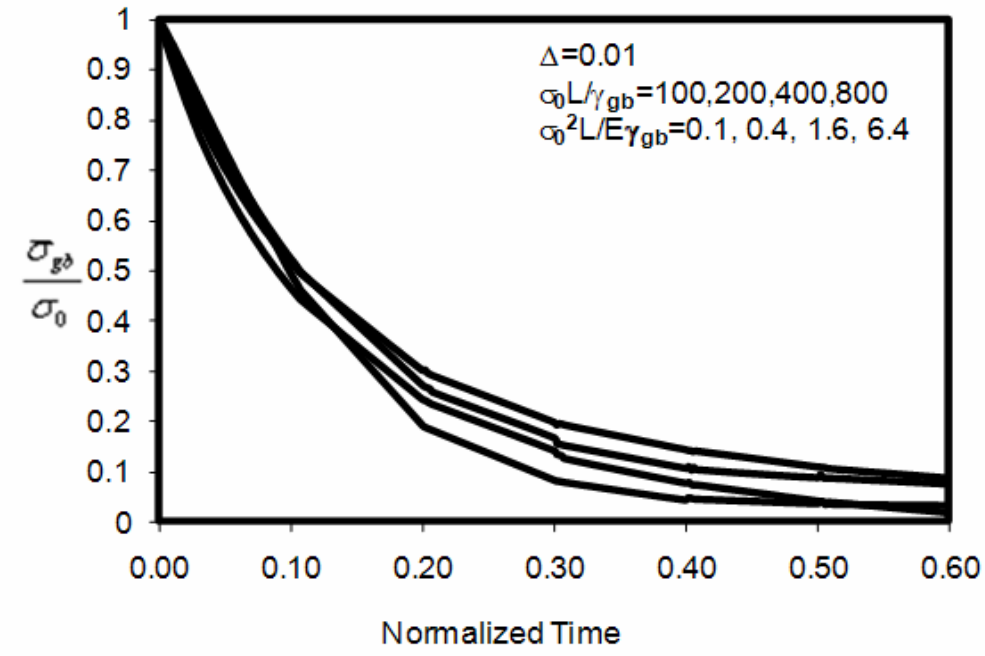

Figure 4-20: Stress relaxation of thin film with free surface under several different initial normal stresses along grain boundary. Grain boundary diffusion is in dominant ($\Delta = 0.01$).

the stress relaxation curves of thin film ($\bar{\gamma} = 1$) under several different initial normal stresses (σ_0).

For capped surface($\bar{\gamma} = 1000$), since the interface almost remains flat, the gradient of strain energy density is negligible and $\overline{w}_0$ is expected not to have effect on stress relaxation. This is also verified by numerical simulations. Figure 4-21 shows the result when surface diffusion and grain boundary diffusion rates are comparable. The results of another two limiting cases are similar (Figures are not shown here).

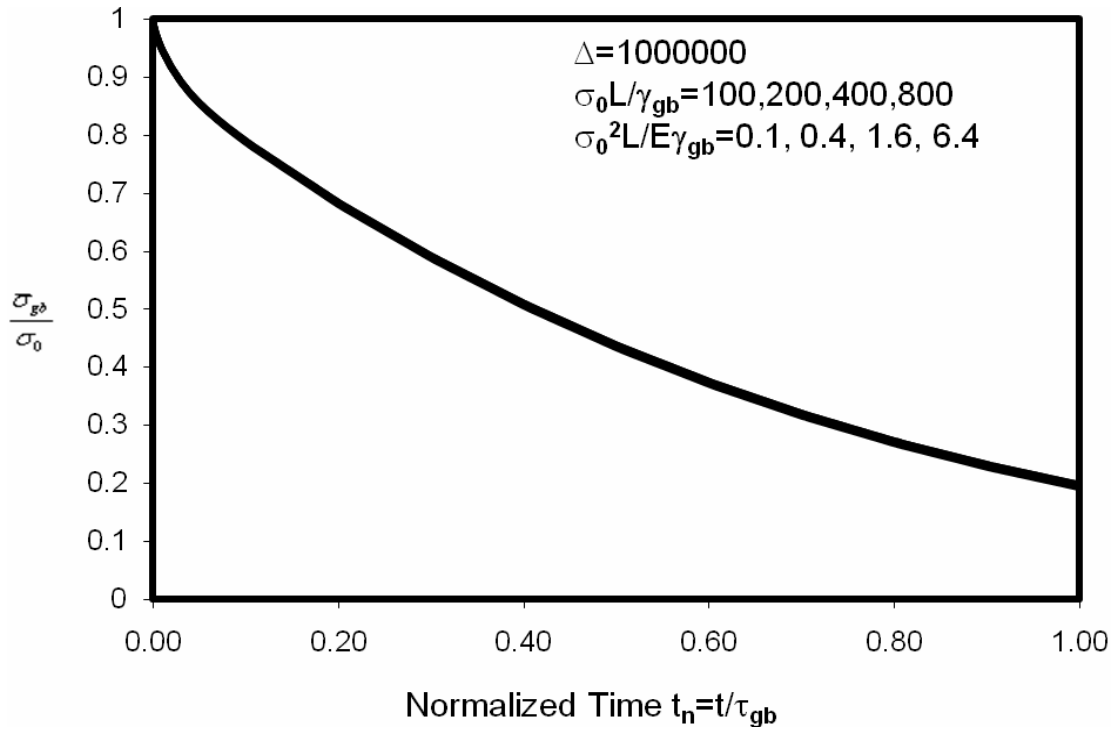

Figure 4-21: Stress relaxation of thin film with caped surface under several different initial normal stresses along grain boundary. ($\Delta = 1$).

4.4 Fitting Experimental Results to Obtain Diffusivity

Grain boundary and surface diffusivities can be deduced by fitting experimental results using numerical simulation. Figure 4-22 shows the stress relaxation data of unpassivated Cu films annealed at different temperatures. The curves were generated from the data in Gan *et al.*[78]. In the temperature range of these experiments, surface diffusion is believed to be much faster than grain boundary diffusion and the stress relaxation process can be approximated as grain boundary diffusion limited. According to our model, as well as Huang's [77], after normalization, as done in Figure 4-4, all these curves ideally should be very close, as the curves for $\Delta > 0.5$ in Figure 4-4. However, in reality, stress evolution in thin film may involve other mechanisms, for example, dislocation generation [75]. In the above experiments, diffusion

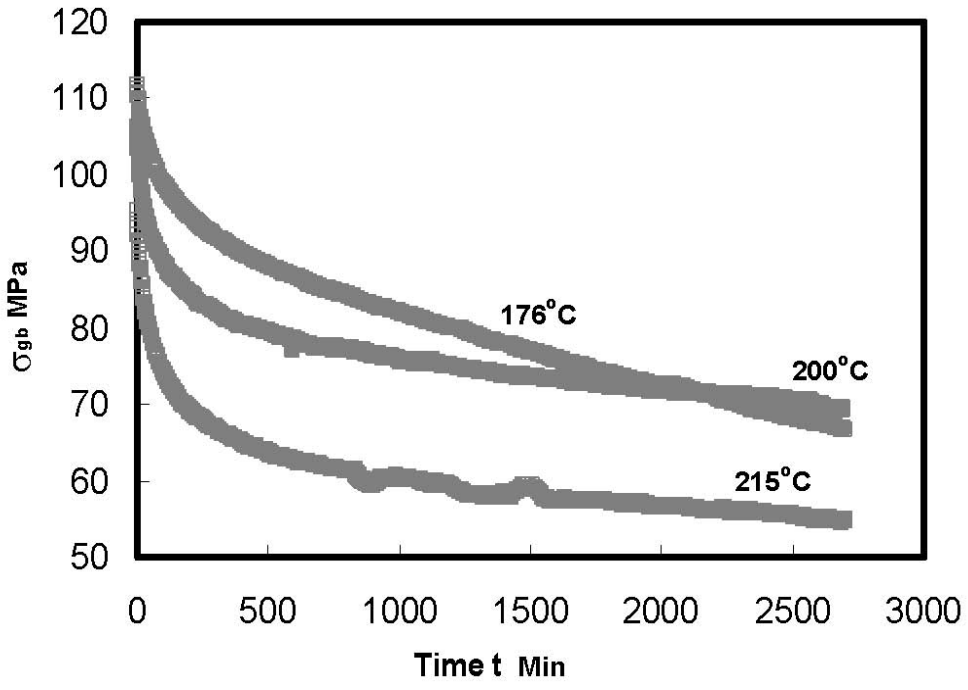

Figure 4-22: Experimental data of stress relaxation of unpassivated Cu film at different temperatures and the fitting curves

processes can relieve majority of the stress in the time period, but not all. In the data processing, the stress $\sigma_n = (\sigma - \sigma_\infty)/(\sigma_0 - \sigma_\infty)$, where σ_∞ is the stress cannot relieved by surface and grain boundary diffusion (see Figure 4-23), is normalized.

First, let's derive the characteristic time in the three stress relaxation curves. According to the dimensional analysis, if stress relaxation process is limited by grain boundary diffusion, the normalized stress σ_n is a function of the normalized time t/τ_{gb} and the effect of temperature is fully accounted in the characteristic time, τ_{gb}. For a given normalized stress σ_n, the ratio of the corresponding relaxation time t_1 and t_2 at temperature T_1 and T_2 is thus the inverse ratio of the two characteristic time

$$t_1/t_2 = \tau_{gb}^{(2)}/\tau_{gb}^{(1)} \tag{4.11}$$

For the experimental data in Figure 4-22, first choose a set of normalized stress from 0.2 to 1

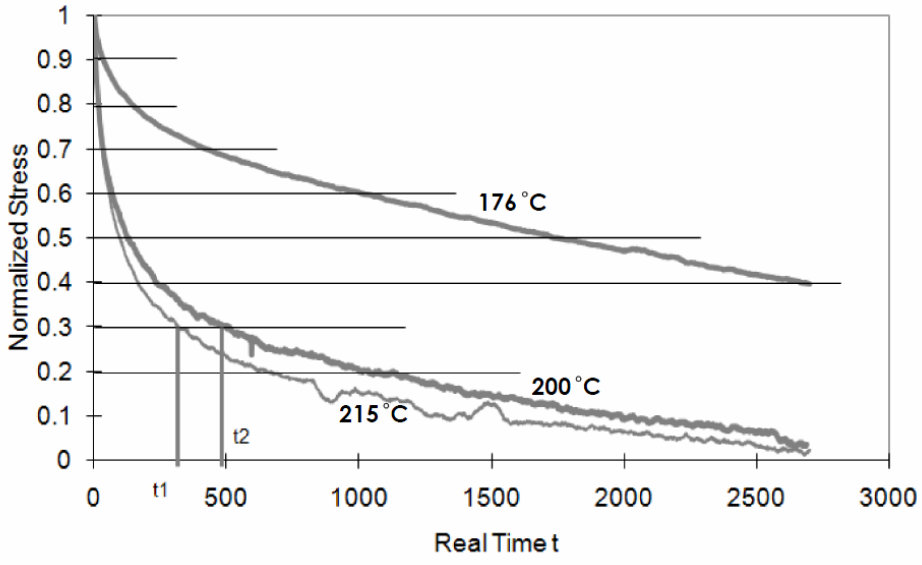

Figure 4-23: Normalized stress relaxation curves of Cu thin film with free surface.

(shorten the second vertical bar) (Figure 4-24). For each normalized stress chosen, find the corresponding relaxation time at three different temperatures. Choosing the set of relaxation time at 215°C as the reference, compare the other two sets with it. In Figure 4-24a, each point corresponds to one specific normalized stress level. Its horizontal coordinate is the corresponding relaxation time at 215°C, and the vertical coordinate is the relaxation time at 176°C for the top curve or 200°C for the lower. The data can be fitted by straight lines passing through the origin; the slope of each curve is the ratio of characteristic time at two different temperatures. In constructing Figure 4-24a, no normal stress below 0.2 is selected, because at the tail of the relaxation curves, a slight reduction of stress takes long time and relaxation time is highly sensitive to the variation of stress. In Figure 4-24b, the relaxation time at 176°C and 200°C are normalized by that of 215°C using the time ratios obtained in Figure 4-24a and plot the stress relaxation curves for three different temperatures. The three curves in Figure 4-24b overlap each other, especially the two curves of 200°C and 215°C.

From Figure 4-24a, the ratio of characteristic time at two different temperatures is determined. Then, compare the normalized time in Figure 4-4 with the relaxation time at 215°C for several normalized stresses from 0.2 to 1. By linearly fitting the two sets of data, the characteristic time, $\tau_{gb} = 15.2 \times 10^3$s at 215°C is obtained. Thus the characteristic time at 176°C and 200°C can be subsequently obtained, $\tau_{gb} = 21.6 \times 10^3$s at 200°C and $\tau_{gb} = 257 \times 10^3$s at 176°C.

Next, the activation energy and diffusivity of grain boundary diffusion need to be determined. The grain boundary diffusivity $D_{gb}\delta_{gb}$ depends on temperature,

$$\delta_{gb} D_{gb} = \delta_{gb} D_{gb0} \exp\left(-\frac{Q_{gb}}{kT}\right) \tag{4.12}$$

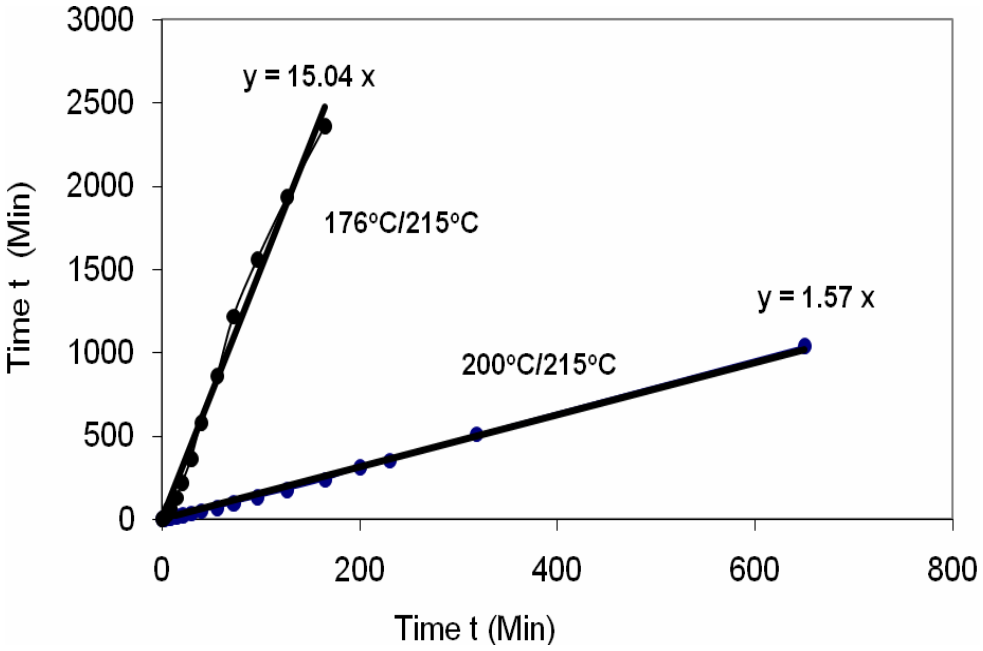

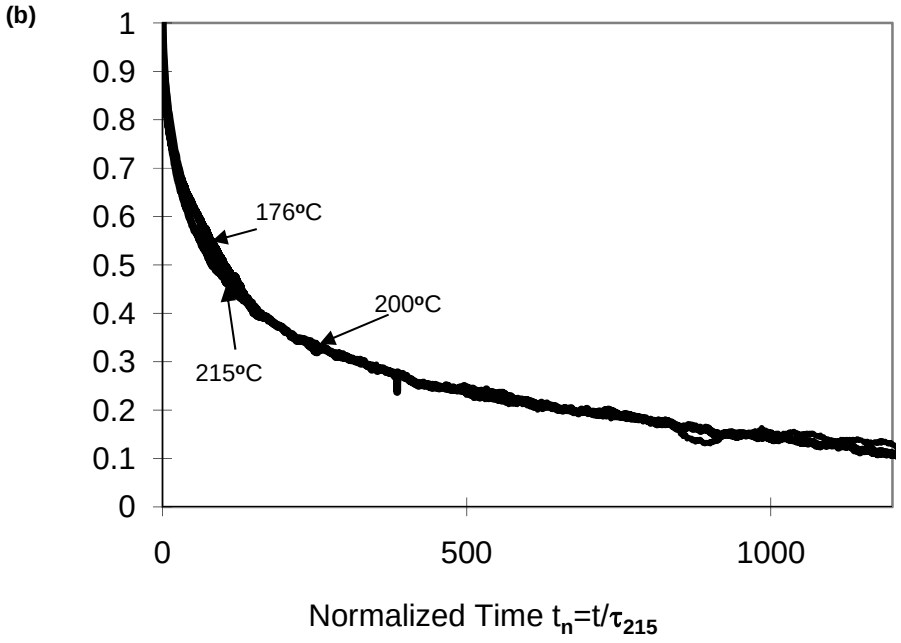

Figure 4-24: Normalized stress relaxation curves. a) Relaxation time ratio between different temperatures. Choose the curve at 215°C as the reference line. b) Normalized all stress relaxation times to the one at 215°C.

where D_{gb0} is the pre-exponential factor for grain boundary diffusivity, and Q_{gb} the activation energy for grain boundary diffusion. The diffusivity is related to the mobility, $M_{gb} = D_{gb}\delta_{gb}\Omega / kT$, which determines the characteristic time through equation (4.8). Combine these relations, giving

$$\delta_{gb} D_{gb} = \frac{4h^2 L}{\pi^2 \Omega} \cdot \frac{kT}{\overline{E}\,\tau_{gb}} \tag{4.13}$$

Using the data obtained above, one can plot $\ln(\overline{E}\,\tau_{gb}/T)$ v.s. $1/T$, which should follow a linear relation according to equations (4.12) and (4.13). By linearly fitting the data, the slope, Q_{gb}/k, and the activation energy, $Q_{gb} = 1.47ev$ can be obtained. The associated constant coefficient in fitting is used to determine the pre-exponential factor $\delta_{gb} D_{gb0} = 3.2 \times 10^{-10}\ m^3/s$. In the calculation, the modulus $\overline{E}$ for Cu is a function of temperature,

$$\overline{E} = 166.3 - 0.094\overline{T} + 7.59 \times 10^{-5}\overline{T}^2 \tag{4.14}$$

where $\overline{E}$ is in GPa and $\overline{T}$ is in ^{o}C [78].

Wide ranges of activation energy Q_{gb} and the pre-exponential factor $\delta_{gb} D_{gb0}$ have been reported previously [103-115] for the grain boundary diffusivity of Cu. In Table 4-I data from different other sources are listed. The historical data reveals the high sensitivity of the results on the methods. From the data in the table, it shows that the activation energy is much larger than the scaling energy kT. According to equation (4.12), even from the same set of data, a slight variation in activation energy can results in huge difference in $\delta_{gb} D_{gb0}$. It indicates that the diffusivity obtained in experiments may not be used to predict diffusivity at a temperature that is far away from the range from which the activation energy and $\delta_{gb} D_{gb0}$ were obtained. Though $\delta_{gb} D_{gb0}$ differs significantly, not the estimated diffusivity. For example, at 200^{o}C, the

Table 4-I: Historical data of activation energy Q_{gb} and the pre-exponential factor $\delta_{gb} D_{gb0}$

	$Q_{gb}(eV)$	$\delta_{gb} D_{gb0}(m^3/s)$	Temperature Range (^{o}C)	$\delta_{gb} D_{gb}(m^3/s)$ at 200^{o}C
Horvath *et al.* [103]	0.64	1.5×10^{-18}	80 - 120	2.27×10^{-25}
Cai *et al*. [114]	0.72	5.2×10^{-18}	20 - 50	1.11×10^{-25}
Surholt *et al*. [111]	0.74	3.89×10^{-16}	511 - 700	3.97×10^{-24}
Gupta *et al*. [110]	0.95	2.9×10^{-15}	250 - 450	2.19×10^{-25}
Gan et al [78]	1.07	1.1×10^{-14}	176, 200, 225	4.37×10^{-26}

diffusivity $\delta_{gb} D_{gb}$ calculated from equation (4.12) is also listed in Table 4-I and the numbers are not as diverse as $\delta_{gb} D_{gb0}$. The numbers obtained, by using the experimental data in Gan et al [78] and our numerical results, are $Q_{gb} = 1.47ev$ and $\delta_{gb} D_{gb0} = 3.2\times10^{-10}\, m^3/s$. These lead to the estimation of diffusivity, $\delta_{gb} D_{gb} = 6.5\times10^{-26}\, m^3/s$ at 200^{o}C, which is of same order of magnitude as that from Gan et al [78]. The numbers are from the best fit of experimental data at three different temperatures. Only use the data for 200^{o}C and 215^{o}C, obtaining $Q_{gb} = 0.48ev$, $\delta_{gb} D_{gb0} = 1.34\times10^{-20}\, m^3/s$, and the estimation of $\delta_{gb} D_{gb} = 9.5\times10^{-26}\, m^3/s$. Apparently, more data at different temperatures are needed to have more accurate estimation.

Combining the grain boundary diffusivity obtained above and adjusting the ratio between interface diffusivity and grain-boundary diffusivity, interface diffusivities of the passivated Cu film at different temperatures can be deduced by doing least-square fitting then. Figure 4-25

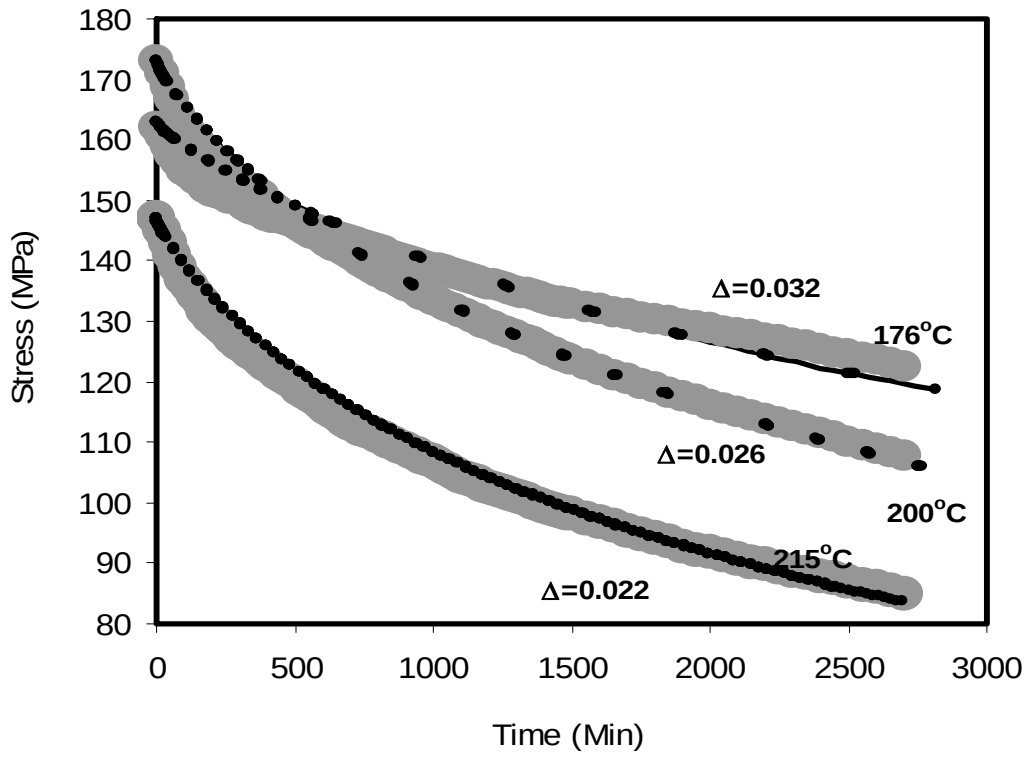

Figure 4-25: Stress relaxation curves at different temperatures of the capped Cu film. The dotted lines are from simulation fitting curves.

shows the stress relaxation data of passivated Cu films annealed at different temperatures, 176, 200 and 215°C. The curves were generated from the data in Gan *et al.*[78] also. The dot curves are the fitting results from our numerical model.

Putting the interface diffusivities into an Arrhenius plot, as shown in Figure 4-26, the activation energy and pre-exponential factor for the interface diffusion: $Q_{gb} = 0.51\,eV$ and $\delta_i D_{i0} = 4.3\times10^{-22}\,m^3/s$ are obtained. These results are similar as those in [78], $Q_{gb} = 0.54\,eV$ and $\delta_i D_{i0} = 6.4\times10^{-22}\,m^3/s$.

Interface diffusion activation energies of Cu film with different caps were reported by Hu *et al* [116 - 118]. The activation energy obtained from electromigration (EM) lifetime process was found to be between 0.75 and 1.25 *eV*. Also, the activation energy determined from EM lifetime

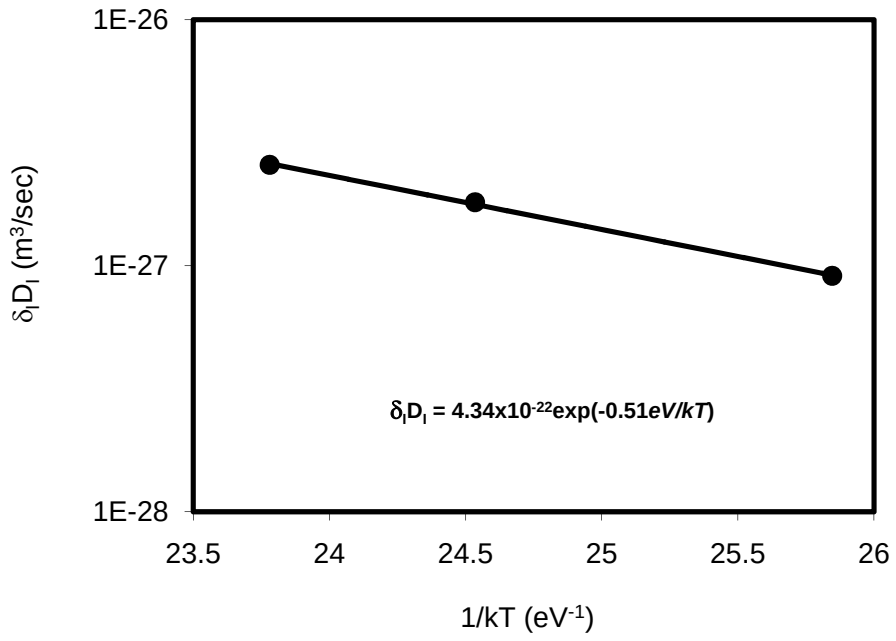

Figure 4-26: Deduced interface diffusivity as a function of temperature of the capped Cu film.

in the Cu lines of 0.75-0.84 [119] and 0.7-0.98 [120] was reported. Obviously, different Cu/cap interface relates activation energy and generally the activation energy of grain boundary diffusion is approximately 0.2 *eV* higher than that of interface diffusion [116]. From these results, the activation energy and pre-exponential factor of interface diffusion of Cu film deduced from our present study can be considered reasonable.

Chapter 5

5 Evolution of Stressed Fiber due to Surface Diffusion

Water jet is unstable. It can break into droplets when the wavelength of a sinusoidal perturbation λ is greater than the cylinder circumference $2\pi R$, where R is the radius of the unperturbed cylinder. The driving force is the reduction of surface energy. The phenomenon is called Rayleigh instability [121]. Mullins and Nichols [14, 83] obtained same threshold condition for solid cylinder rods under annealing: to minimize the surface energy, a small perturbation may grow and break the cylinder. They also got the similar result for cylinder voids in solids [84]. Similar to stressed thin film, when a fiber is under stress, it becomes more unstable. Linear stability analyses [92 -95] have showed that Instabilities exist even the wavelength of the fiber is smaller than the circumference to relax the elastic energy.

To study the non-linear evolution process of cylinder solid with large amplitude perturbation under stress, the weak statement is applied to the stressed fiber to simulate its morphology evolution. In the next section, the weak statement is first reviewed and is then used to formulate a finite element method for axi-symmetric surface motion. The numerical result on the morphology evolution of a stressed fiber is reported. It shows that, under a periodic perturbation, the stressed fiber may evolve back to initial shape, or develop grooves first then approach to a

steady state shape, or develop cusps and break into particles. The simulation results will roughly obtain these two stress threshold conditions corresponding to different wavelengths.

5.1 Numerical Methods

The numerical procedure is similar to the two cases in the last two chapters. The difference is that this case studies axi-symmetric surface.

5.1.1 Weak Statement and Axisymmetric Finite Element

Recall the general weak statement in three dimensions, equation (2.55). Only surface diffusion is considered as the mass transportation method in stressed fiber, such that the weak statement becomes,

$$\int \left\{ \frac{\mathbf{J} \cdot \delta \mathbf{I}}{M} + \frac{\left(v_n + \nabla \cdot \mathbf{J}\right)\left[\delta r_n + \nabla \cdot \left(\delta \mathbf{I}\right)\right]}{m} \right\} dA = -\delta G \,. \tag{5.1}$$

The integral extends over the surface area. Similarly, $m\lambda / M = 10^{-6}$ is adopted to suppress the evaporation-condensation process.

Following Yu and Suo [54], the axisymmetric finite element is formulated. An axisymmetric surface is generated by rotating a plane curve around an axis lying on the same plane. The generating curve is divided into many small straight elements. The surface is then represented by the coordinates of all the nodal points and the motions of the nodes describe the motion of the surface. Each node on the plane curve represents a circle on the surface in three dimensions. Figure 5-1 shows one element with nodes (x_1, y_1) and (x_2, y_2). The element has length l, slope θ; again, the local coordinate, s, is measured from the middle point of the element.

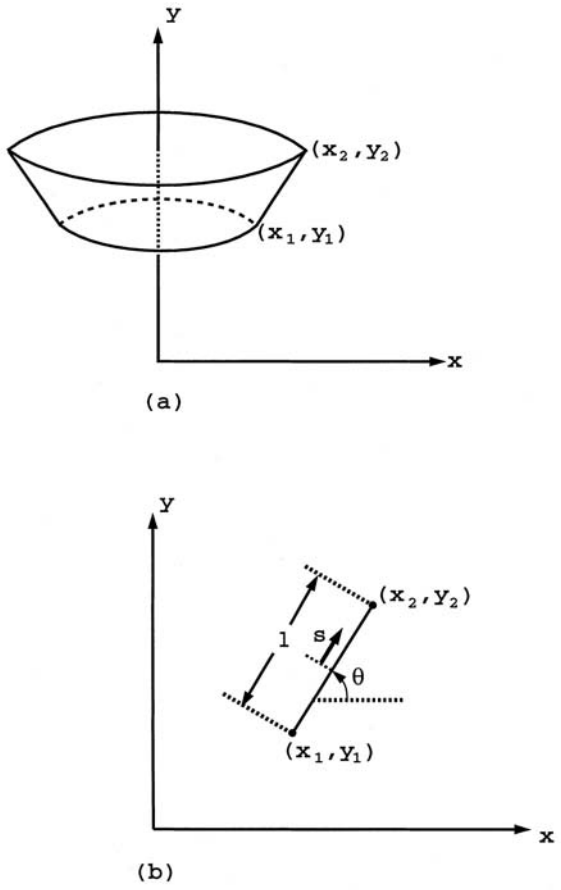

Figure 5-1: An axisymmetric element in three dimensions (a) and in a plane (b). Yu and Suo [54]

Adopt the same treatment as that in two dimensions cases. Let I_1, I_2, I_m be the mass displacements at the two nodes and the middle point of the element, and J_1, J_2, J_m the fluxes at the two nodes and the middle point of the element. On one element, interpolate the virtual displacement and actual velocity linearly by using shape functions (3.6)

$$\delta r_n = N_1 \delta x_1 + N_2 \delta y_1 + N_3 \delta x_2 + N_4 \delta y_2 \qquad \textbf{(5.2)}$$

$$v_n = N_1\dot{x}_1 + N_2\dot{y}_1 + N_3\dot{x}_2 + N_4\dot{y}_2$$

and interpolate the virtual mass displacement and actual mass flux quadratically by using shape function (3.10)

$$\begin{aligned} \delta \mathrm{I} &= Q_1\delta \mathrm{I}_1 + Q_m\delta \mathrm{I}_m + Q_2\delta \mathrm{I}_2 \\ J &= Q_1 J_1 + Q_m J_m + Q_2 J_2 \end{aligned} \tag{5.3}$$

For each element, the integral over the surface in the weak statement (5.1) gives the bilinear form $\left(\delta q^e\right)^T \mathbf{H}^e q^e$, where $\mathbf{H}^e$ is a 7 x 7 matrix, the components of which are given in the Appendix F.

Assuming the mechanical load is given as displacement controlled, there is no work done by the external load in the surface evolution process. The total free energy of this system is

$$G = \int_{surface} \gamma dA + \int_{solid\ body} w dv \tag{5.4}$$

where γ is the surface tension and w is the strain energy density of the element. The free energy reduction associated with the virtual motions, δG, is a sum over all elements. Assume the surface energy, γ, is isotropic and the strain energy, w, is uniform in one element. The free energy variation in one element then is

$$\delta G = \gamma \delta A + w\delta v \tag{5.5}$$

For one element, as shown in Figure 5-1, the surface area is

$$A = \pi\left(x_1 + x_2\right)l \tag{5.6}$$

where x_1 and x_1 are the radii at the two nodes of the element. The virtual surface area variation is

$$\delta A = \pi\left(x_1 + x_2\right)\delta l + \pi\left(\delta x_1 + \delta x_2\right)l \tag{5.7}$$

δl can be represented by the interpolation of two nodes as equation (3.7). Thus, one can obtain the virtual surface area variation as a function of virtual motions of two nodes of the element, giving

$$\begin{aligned}\delta A = {} & \pi\left[l-\left(x_1+x_2\right)\cos\theta\right]\delta x_1 - \pi\left[\left(x_1+x_2\right)\sin\theta\right]\delta y_1 \\ & + \pi\left[l+\left(x_1+x_2\right)\cos\theta\right]\delta x_2 + \pi\left[\left(x_x+x_2\right)\sin\theta\right]\delta y_2\end{aligned} \tag{5.8}$$

Since the mass exchange occurs on the surface by the surface diffusion, only the virtual volume change near surface is of interest, which is

$$\delta v = \int_l 2\pi r \delta r_n ds \tag{5.9}$$

where r is the radius at arbitrary point of the element which can be represented by the interpolation of two nodes

$$r = \left(\frac{1}{2}-\frac{s}{l}\right)x_1 + \left(\frac{1}{2}+\frac{s}{l}\right)x_2 \tag{5.10}$$

Place (5.10) into the virtual volume change, equation (5.9), and integrate over one element, giving

$$\begin{aligned}\delta v = {} & \frac{\pi l}{3}\left[\left(2x_1+x_2\right)\sin\theta\right]\delta x_1 - \frac{\pi l}{3}\left[\left(2x_1+x_2\right)\cos\theta\right]\delta y_1 \\ & + \frac{\pi l}{3}\left[\left(x_1+2x_2\right)\sin\theta\right]\delta x_2 - \frac{\pi l}{3}\left[\left(x_x+2x_2\right)\cos\theta\right]\delta y_2\end{aligned} \tag{5.11}$$

Because free energy G defined by equation (5.4) varies as the shape varies, only driving forces associated with the motion of the coordinates are used. No driving forces are associated with the virtual mass displacements at two nodes and the mid-point of the element. Consequently, the free energy reduction of the element is

$$-\gamma\delta A - w\delta v = f_1\delta x_1 + f_2\delta y_1 + f_3\delta x_2 + f_4\delta y_2 \tag{5.12}$$

where δx_1, δy_1, δx_2 and δy_2 are virtual motions of the two nodes of the element. Substitute virtual surface area variation equation (5.8) and virtual body variation near to the surface equation (5.11) into the left hand side of equation (5.12) and compare the factors for each arbitrary virtual motion of two end nodes of the element, giving the force components acting on the two nodes due to element surface tension and elastic energy

$$\begin{bmatrix} f_1 \\ f_2 \\ f_3 \\ f_4 \end{bmatrix} = \pi\gamma \begin{bmatrix} -l + (x_1 + x_2)\cos\theta \\ (x_1 + x_2)\sin\theta \\ -l - (x_1 + x_2)\cos\theta \\ -(x_1 + x_2)\sin\theta \end{bmatrix} + \frac{\pi l w}{3} \begin{bmatrix} -(2x_1 + x_2)\sin\theta \\ (2x_1 + x_2)\cos\theta \\ -(x_1 + 2x_2)\sin\theta \\ (x_1 + 2x_2)\cos\theta \end{bmatrix} \tag{5.13}$$

5.1.2 Mass Conservation in Three Dimensions

Mass conservation law, equation (2.48), is applied to the second term of integral in the weak statement (5.1). In the definition of the weak statement (5.1), the virtual motions are in three dimension, i.e. $\delta\mathbf{I}$ is the volume of matter crossing per unit length of the curve, δi the volume of matter added to the surface per unit area.

In this model, straight line elements are used to generate the axisymmetric surface. Each node on the plane element represents a circle on the surface in three dimensions. Thus, the mass conservation law becomes,

$$r\delta r_n = r\delta i - \nabla \bullet (r\delta I) \tag{5.14}$$

From equation (5.10), r is a function of the local coordinate, s, also. The mass conservation law then finally be modified as

$$r\partial i = r\delta r_n + r\frac{\partial(\delta I)}{\partial s} + \delta I\cos\theta \tag{5.15}$$

Similarly, the relation between actual velocity and fluxes gives

$$r\,j = r v_n + r\frac{\partial J}{\partial s} + J\cos\theta \tag{5.16}$$

Then the revised weak statement in which the conservation laws (5.15) and (5.16) are included becomes

$$\int\left\{\frac{\mathbf{J}\cdot\delta\mathbf{I}}{M} + \frac{\left(r v_n + r\frac{\partial J}{\partial s} + J\cos\theta\right)\left[r\delta r_n + r\frac{\partial(\delta I)}{\partial s} + \delta I\cos\theta\right]}{m r^2}\right\}dA = -\delta G \tag{5.17}$$

The integral can be calculated element by element. In each element, using the shape functions to interpolate all the virtual motions and actual velocity and fluxes, and applying $dA = 2\pi r ds$ to the equation (5.17), one can get the element viscosity matrix $\mathbf{H}^e$.

The numerical integration of the second term may diverge because of the factor r^{-2}. Since the evaporation-condensation process in this case is neglected, which means m is a very small number comparing to M, the radius of the middle point of the element, $(x_1 + x_2)/2$, is used to replace the radius r in the denominator of the second term in equation (5.17). Denote

$$m' = m\left(\frac{x_1 + x_2}{2}\right)^2 \tag{5.18}$$

and substitute it into equation (5.17), giving

$$\int\left\{\frac{\mathbf{J}\cdot\delta\mathbf{I}}{M} + \frac{\left(r v_n + r\frac{\partial J}{\partial s} + J\cos\theta\right)\left[r\delta r_n + r\frac{\partial(\delta I)}{\partial s} + \delta I\cos\theta\right]}{m'}\right\}dA = -\delta G \tag{5.19}$$

The element viscosity matrix $\mathbf{H}^e$ obtained from equation (5.19) is list at Appendix F.

5.2 Evolution of Stressed Fiber

5.2.1 Linear Perturbation Analysis

Figure 5-2 illustrates a long cylinder of initial radius R_0 with isotropic surface tension γ. Perturb the cylinder to a wavy surface of revolution

$$r(z,t) = R_0\left[\rho(t) + \varepsilon(t)\cos\frac{2\pi z}{\lambda}\right] \tag{5.20}$$

where r is the radius of the perturbed surface, z the axis of revolution, t the time, ρR_0 the average radius, εR_0 the amplitude, and λ the wavelength.

Mass conservation requires that the volume of the cylinder keeps constant. Thus,

$$\int_0^{\lambda} \pi r^2 dz = \pi {R_0}^2 \lambda \tag{5.21}$$

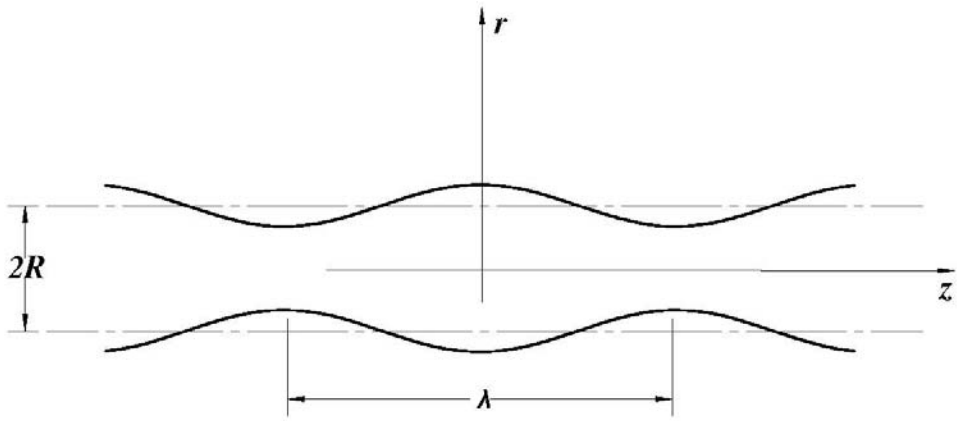

Figure 5-2: Perturb a cylindrical surface to a surface of revolution with undulation along the axial direction

The left hand side is the volume of one wave period of cylinder after perturbation and the right hand side is that before perturbation. Solve this equation by substituting r in equation (5.20) into equation (5.21), to the leading term in ε, giving

$$\rho = 1 - \frac{\varepsilon^2}{4} \tag{5.22}$$

Putting ρ above back into equation (5.22), one has the surface profile as

$$r = R_0[1 - \frac{\varepsilon^2}{4} + \varepsilon \cos(kz)] \tag{5.23}$$

where $k = 2\pi / \lambda$ is the wave vector, introduced into the lateral surface of the fiber.

Derive the linear perturbation growth rate by solving the weak statement (5.1). Since in this case only surface diffusion has been considered, equation (5.1) is simplified by getting rid of the term of evaporation-condensation process. Thus, the modified weak statement becomes

$$\int \frac{J \cdot \delta I}{M} dA = -\delta G \tag{5.24}$$

Because it is axi-symmetric, the boundary condition at $z = 0$ is $J_{(z=0)} = 0$. Thus, for the part between any cross section and the polar point, the mass conservation requires that the volume reduction per unit time should equal to the mass flow across the cross section per unit time, which gives

$$2\pi r J = -\frac{\partial}{\partial t} \int_0^z \pi r^2 dz \tag{5.25}$$

Radius r is expressed in equation (5.23). In the linear perturbation analysis, ε is very small in the evolution progress. Neglecting second and higher order of ε, obtain

$$J = -\frac{R_0 \lambda}{2\pi} \sin(kz) \dot{\varepsilon} \tag{5.26}$$

where $\dot{\varepsilon}$ is the time derivative of ε. Consequently, the virtual mass displacement is

$$\delta I = -\frac{R_0 \lambda}{2\pi} \sin(kz)\delta\varepsilon \tag{5.27}$$

where $\delta\varepsilon$ is the virtual change of ε. Substitute flux J in equation (5.26), and virtual mass displacement δI in equation (5.27), into weak statement (5.24) and integrate over one wavelength period, giving

$$\int \frac{\left(\frac{R_0 \lambda}{2\pi}\right)^2 \sin^2(kz)\dot{\varepsilon}\delta\varepsilon}{M} dA = -\delta G \tag{5.28}$$

Colin [92] et al. derived the free energy density variation, ΔU, for a stressed pore channel. By conforming it to a stressed fiber, one can obtain

$$\Delta U = \frac{\gamma\varepsilon^2}{4}\left[\omega^2 - 1 + \frac{(1+\upsilon)\omega}{2\pi}\Lambda f\left(\frac{2\pi}{\omega}\right)\right] \tag{5.29}$$

where $\omega = 2\pi R_0 / \lambda$, and the dimensionless variable, Λ, is the loading level

$$\Lambda = \frac{\sigma^2 \lambda}{E\gamma} \tag{5.30}$$

in which E is the elastic modules. The function $f\left(\frac{2\pi}{\omega}\right)$ is defined by

$$f(\frac{2\pi}{\omega}) = \frac{(3-2\upsilon)I_0(\omega) - I_1^2(\omega) - \frac{4(1-\upsilon)I_0(\omega)I_1(\omega)}{\omega}}{I_0^2(\omega) - I_1^2(\omega) - \frac{2(1-\upsilon)I_1^2(\omega)}{\omega^2}} \tag{5.31}$$

where υ is Poisson ratio, $I_0(\omega)$ and $I_1(\omega)$ are modified Bessel functions of the first kind of zero and first order, respectively. The free energy density variation, ΔU， includes strain energy density, w, and surface energy, γ, which are mentioned in equation (5.5). Denote the total free energy variation of a volume of one wavelength period ΔW,

$$\Delta W = 2\pi R \Delta \mathrm{U} \tag{5.32}$$

Then the total free energy variation associated with virtual motion for one wavelength period, δG, is

$$\delta G = \frac{\partial(\Delta W)}{\partial \varepsilon}\delta\varepsilon \tag{5.33}$$

By combining equations (5.29) and (5.32), finally, δG can be represent as

$$\delta G = \pi R_0 \lambda \gamma \left[\omega^2 - 1 + \frac{(1+\upsilon)\omega}{2\pi} \Lambda f\left(\frac{2\pi}{\omega}\right)\right]\varepsilon\delta\varepsilon \tag{5.34}$$

Finally an ODE, to the leading term of ε, can be obtained by substituting equation (5.34) into the equation (5.28), integrating it and neglecting the high order of ε,

$$\dot{\varepsilon} = \frac{M\gamma}{R_0^4}\omega^2\left[1 - \omega^2 + \frac{(1+\upsilon)\omega}{2\pi}\Lambda f\left(\frac{2\pi}{\omega}\right)\right]\varepsilon \tag{5.35}$$

By solving this ODE, one can obtain the amplitude of linear perturbation as a function of time

$$\varepsilon = \varepsilon(0)e^{t/\tau} \tag{5.36}$$

where τ is the characteristic time

$$\frac{1}{\tau} = \frac{M\gamma}{R_0^4}\omega^2\left[1 - \omega^2 + \frac{(1+\upsilon)\omega}{2\pi}\Lambda f\left(\frac{2\pi}{\omega}\right)\right] \tag{5.37}$$

Equation (5.36) shows that the characteristic time, τ, determines the perturbation growth rate $1/\tau$. The bigger $1/\tau$ represents the faster perturbation growth, and vice versa.

The limiting case, unstressed fiber, reduces to Rayleigh's result, which is that a cylinder is unstable under sinusoidal perturbation whose wavelength λ is greater than the cylinder

circumference $2\pi R$. By simply setting the loading level $\Lambda = 0$ in equation (5.37), one can obtain the characteristic time, τ_0, of perturbation growth for unstressed cylinder,

$$\frac{1}{\tau_0} = \frac{M\gamma}{R_0^4}\omega^2\left(1-\omega^2\right) \tag{5.38}$$

According to equation (5.38), $\omega = 1$ is the critical value for perturbation growth. When $\omega > 1$, $1/\tau_0 < 0$, perturbation amplitude decreases along time per equation (5.36); whereas $\omega < 1$, $1/\tau_0 > 0$, perturbation amplitude grows along time. $\omega = 1 = 2\pi R_0/\lambda$, gives the critical wavelength of unstressed fiber,

$$\lambda_{c0} = 2\pi R_0 \tag{5.39}$$

Also, setting $d\left(1/\tau\right)/d\omega = 0$ gives the fastest growth rate for the unstressed cylinder can be obtained,

$$\lambda_{m0} = 2\sqrt{2}\pi R_0 \tag{5.40}$$

For the stressed fiber, the critical perturbation wavelength of fastest growth rate still can be obtained by letting $d\left(1/\tau\right)/d\omega = 0$, where $1/\tau$ is defined by equation (5.37),

$$2 - 4\omega^2 + \frac{3\left(1+\upsilon\right)}{2\pi}\omega\Lambda f\left(\frac{2\pi}{\omega}\right) - \left(1+\upsilon\right)\Lambda f'\left(\frac{2\pi}{\omega}\right) = 0 \tag{5.41}$$

This equation gives the relationship between the wavelength λ_m and loading level Λ. Figure 5-3 plots the perturbation growth rate under different uniaxial stresses ($1/\tau$ vs. ω). The solid lines are the linear analysis results of fiber instability which are predicted by equation (5.37), with different loading level, $\sigma^2 R_0/E\gamma = 1, 0.5, 0.1, 0$, respectively. These curves indicate that the maximum groove growth rate increases and shifts to smaller perturbation wavelength as

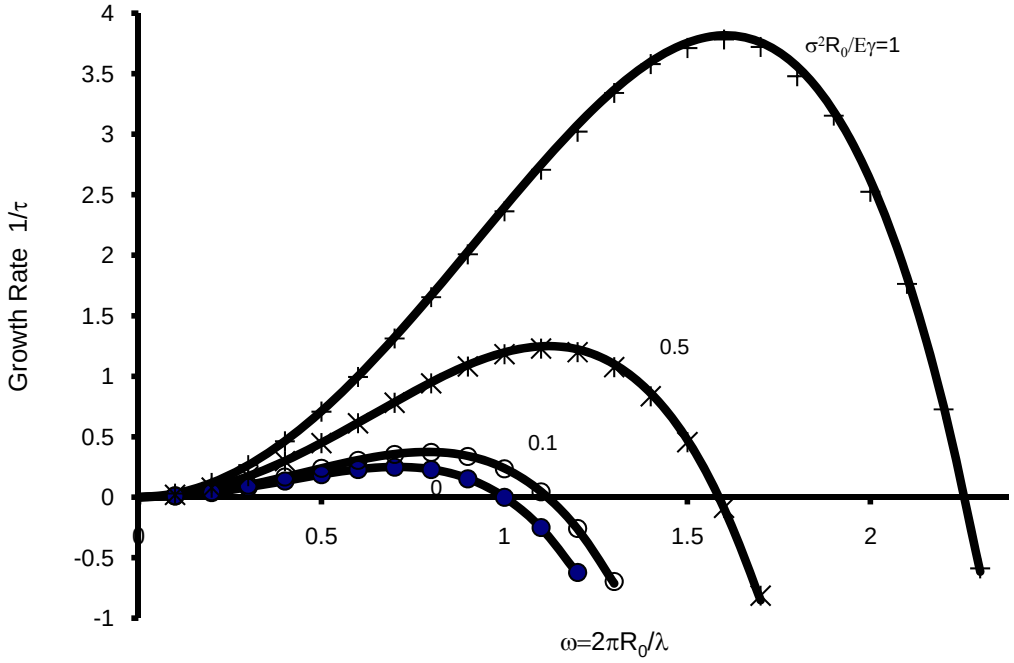

Figure 5-3: Perturbation growth rate of fiber under several different loading levels.

stress increases. In the mean time, the dot lines are the simulation results of linear instability of fiber with corresponding loading level.

5.2.2 Simulation Results

It is known that, from Equation (5.36), the amplitude of perturbation will grow when the growth rate $1/\tau > 0$ and it will reduce when $1/\tau < 0$. Figure 5-3 illustrates the tendency that the stress shifts the critical instability wavelength of stressed cylinder toward shorter values. On the other word, the critical condition for unstressed fiber does not hold for stressed fiber, which may be unstable even the wavelength of a sinusoidal perturbation λ is smaller than the cylinder

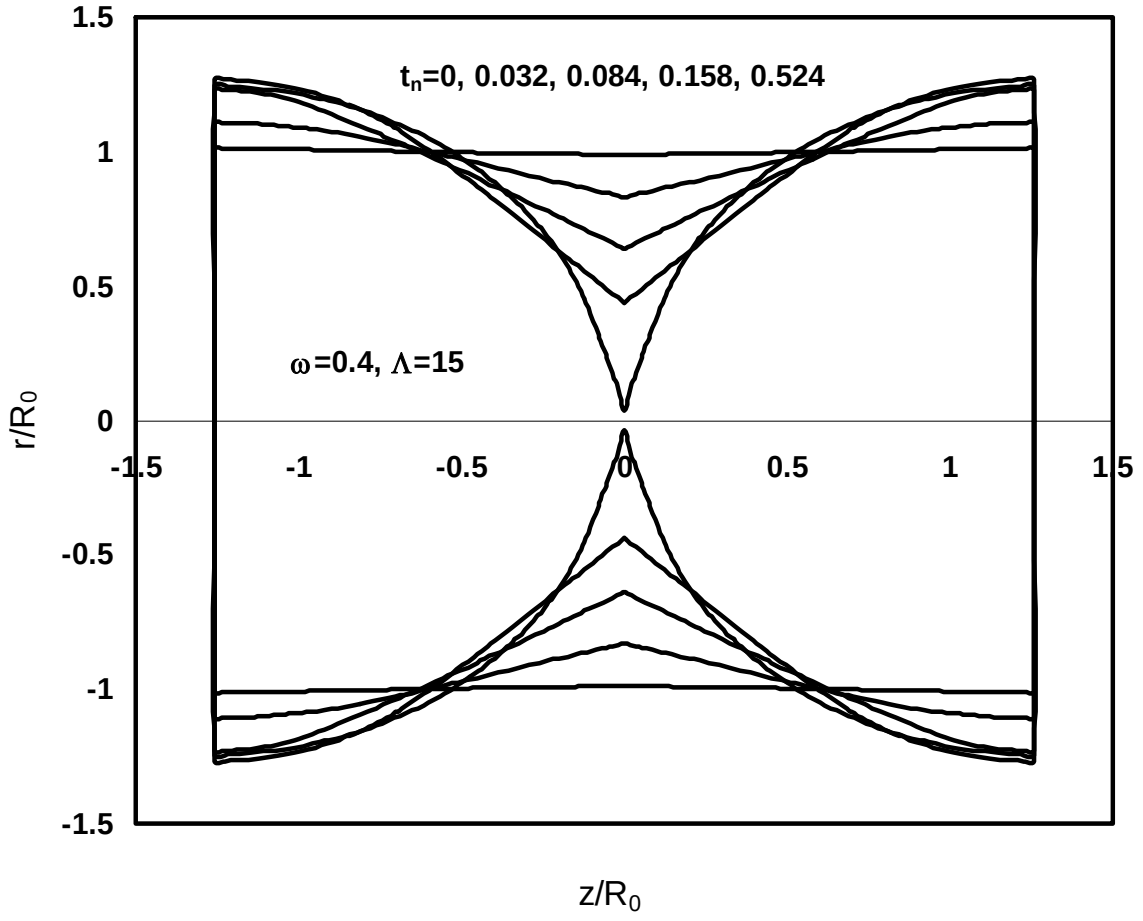

Figure 5-4: Surface Profile of Stressed Fiber. ω=0.4, Λ=15

circumference $2\pi R_0$. Figure 5-4 illustrates the surface profiles of stressed fiber at different times. It is shown that, the perturbation grows to groove and the fiber then breaks even when the wavelength $\lambda = 0.8\pi R_0$.

By setting growth rate $1/\tau = 0$ in equation (5.16), the critical normalized stress level Λ_c can be obtained as a function of the perturbation wavelength,

$$\Lambda_c = \frac{\omega^2 - 1}{f\left(\frac{2\pi}{w}\right)\frac{(1+\upsilon)\omega}{2\pi}}. \qquad \textbf{(5.42)}$$

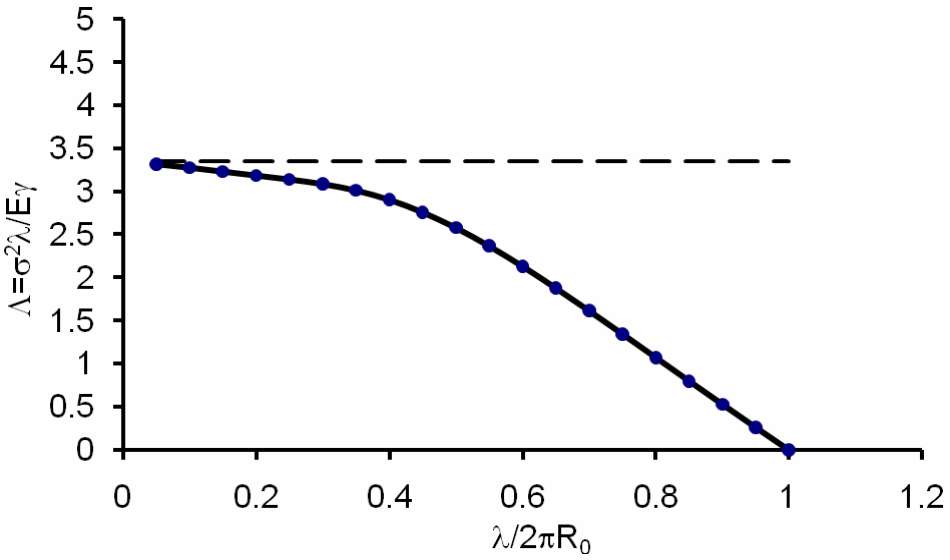

Figure 5-5: Stress criteria of Linear Instability at different perturbation wavelength

The results from Equation (5.42) are shown in Figure 5-5. The numerical result matches the theoretical value perfectly which approves the reliability of our numerical program.

The solid line in Figure 5-5 is from equation (5.42) and the data marks are from our simulation. The straight dash line is the critical value of two-dimensional case, which is $\Lambda_c = \pi$ for any perturbation wavelength. As Figure 5-5 indicates, when the wavelength of perturbation decreases, the critical loading level of cylinder approaches to the critical loading level of a plane.

The morphology evolution of the stressed fiber is simulated even after the instability occurs and found that the fiber would not always break when the loaded stress level is greater than the criteria value. Sometimes, the surface evolution forms a groove and then reaches to a steady state. Our numerical simulation obtains the second critical stress value from steady state to final state of breaking. Shown in Figure 5-6, when $\lambda/2\pi R_0$ is larger than 0.5, if the loading level is greater than the critical load level from linear instability analysis, the fiber will always break.

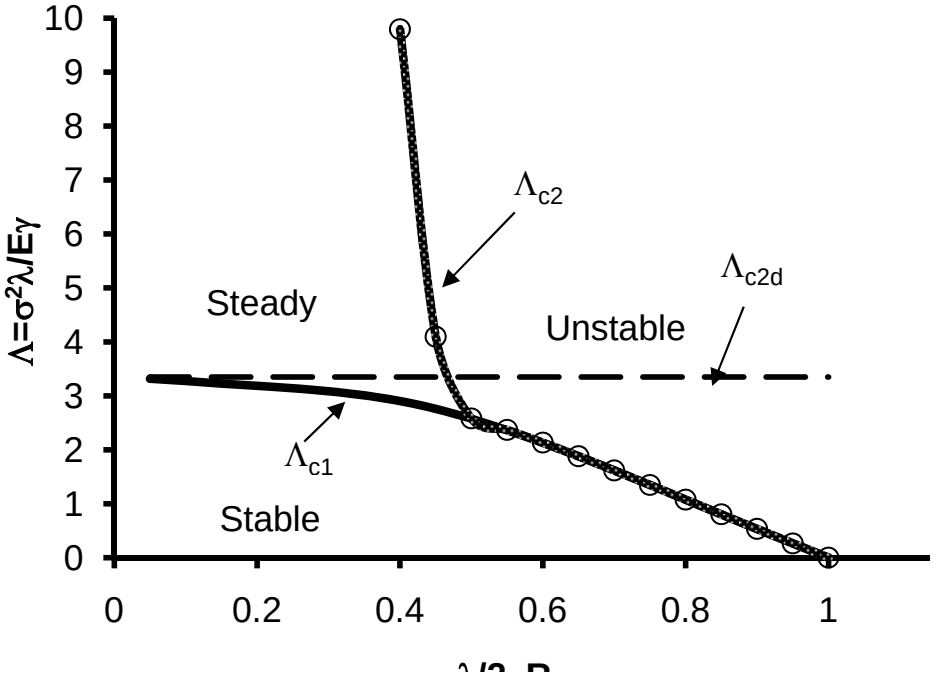

Figure 5-6: Stress criteria at different perturbation wavelength

When $\lambda/2\pi R_0$ is less than 0.5, if the loading level is under the first linear critical line, $\Lambda < \Lambda_{c1}$, the stressed fiber will keep stable; but when the stress level is greater than the second critical line, $\Lambda > \Lambda_{c2}$, the stressed fiber will keep evolving by surface diffusion and eventually break into particles; and when the stress level is between these two critical lines, $\Lambda_{c1} < \Lambda < \Lambda_{c1}$, the initial instability will occur, surface becomes wavy, but the stressed fiber will reach a steady profile finally.

Simulation curves in Figure 5-7 show the example of the surface profile evolution of stressed fiber which finally reaches its steady state. The stressed fiber has the same wavelength as what shown in Figure 5-4, but different stress level.

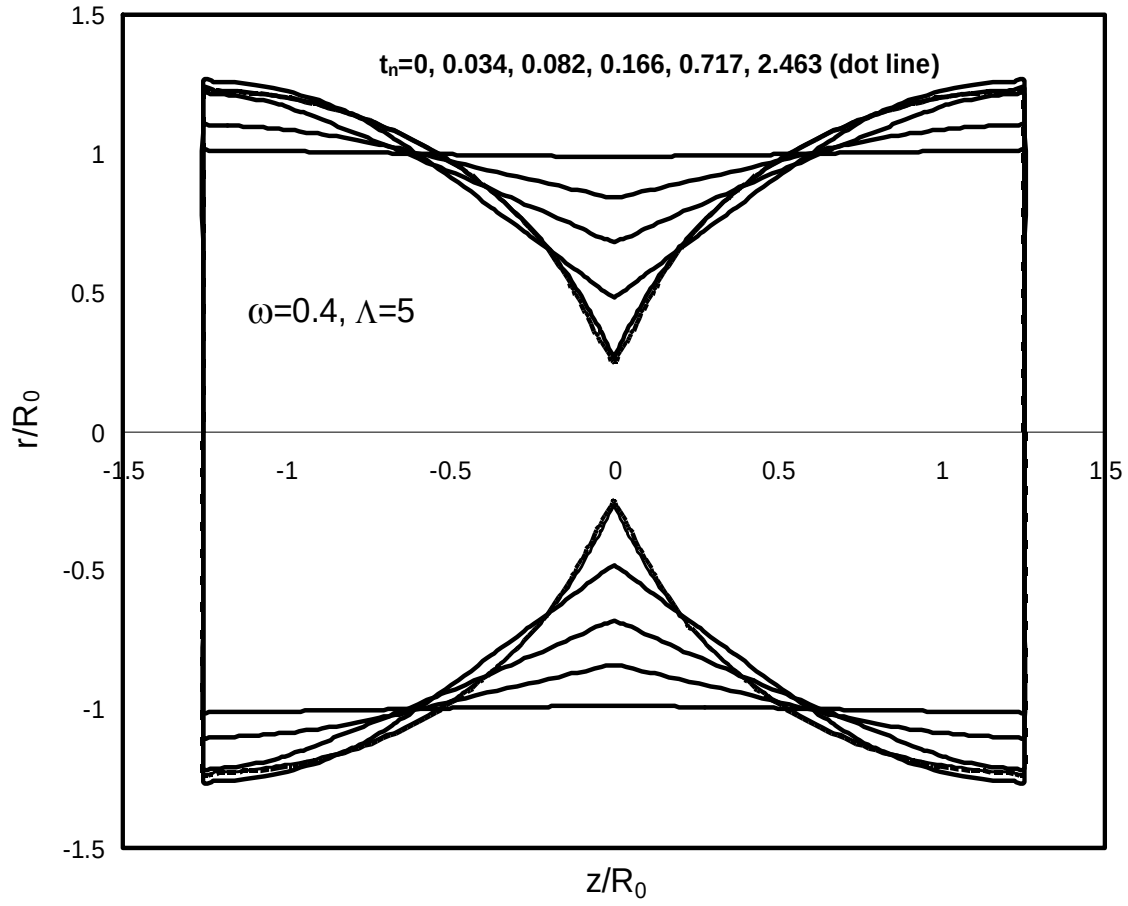

Figure 5-7: Surface Profile of Stressed Fiber. ω=0.4, Λ=5

In Figure 5-8, The normalized groove depth, R_t / R_{0t}, as a function of normalized time, t/τ, for four different values of loading parameter, Λ, is plotted. The wavelength is $\lambda = 0.3 \times (2\pi R_0)$ and the critical stress level from linear instability analysis is $\Lambda_{c1} = 3.1$. Our simulation results apparently show that the fiber may keep stable (Figure 5-8, $\Lambda = 2.8$); or develop grooves then approach to a steady state shape (Figure 5-8 $\Lambda = 9.4, 47$), or develop cusps and break into particles (Figure 5-8 $\Lambda = 53$).

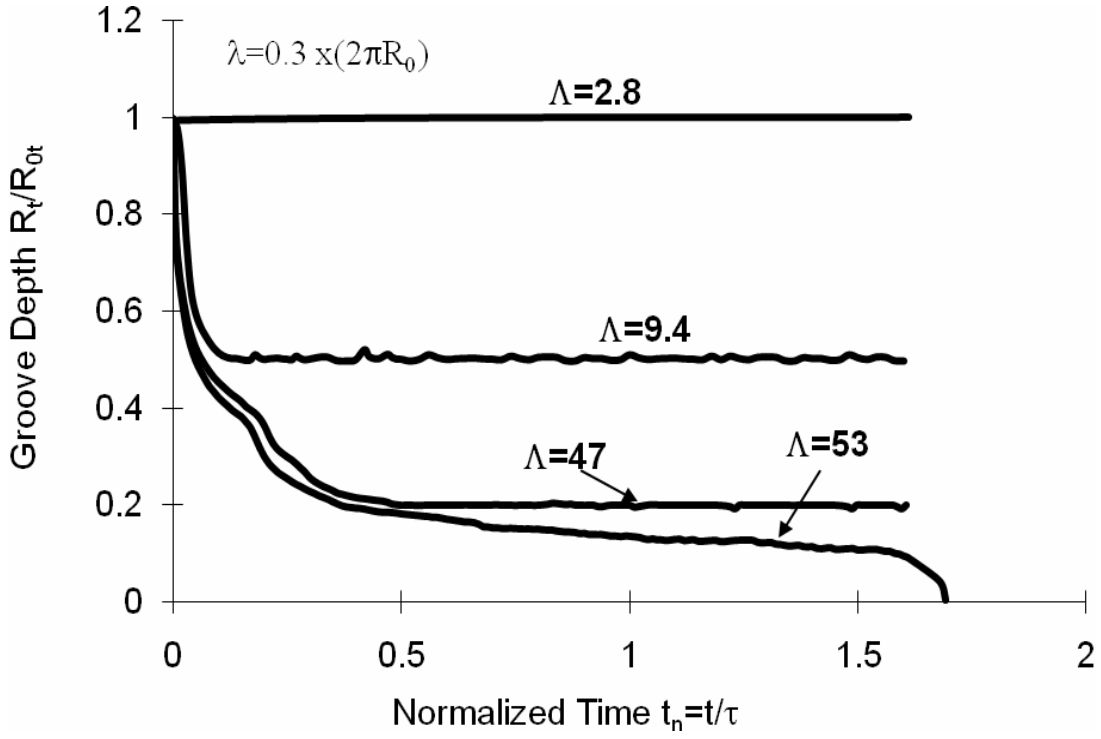

Figure 5-8: Groove depth grows at different stress level

Chapter 6

6 Conclusion

Residual stress in solid can significantly affect the way of mass transportation and then its properties. Thus, studying and then trying to control the stress is very important. A numerical approach based on the weak statement, a global view that regards interface motion as a mean to release the total free energy, has been developed to study morphology evolution of stressed solid due to interface motions. Boundary Element Method (BEM), which only requires discretization of surface instead of volume, is applied to solve the stress field with evolving boundary. On the basis of the numerical approach, a computer program is developed as a tool box to study the morphology evolution of stressed solid.

The problem of morphology instability and formation of surface cusp of stressed thin film is simulated. The program can reproduce the analytical results for surface under small sinusoidal perturbation, and can simulate surface morphology evolution under concurrent surface diffusion and evaporation-condensation processes. More interesting results are the dependence of surface morphology evolution path on the initial surface configuration. It is found that surfaces with initial surface cracks and notches can take much longer time to form sharp cusps. Localized surface defects or surface roughness, with local radius of curvature much smaller than the critical wavelength, could stabilize the surface and greatly delay the emergence of surface instability, due to the excessive surface area and longer diffusion path. The property might be used in some

specific practical applications. To make a thin film more stable, one may introduce some scratch or period notches on the nearly perfect surface. The results are based on the assumption that the remote stress doesn't do any work, for example, in the residually stressed surface.

Stress relaxation in thin film due to annealing is simulated. Surface diffusion and grain boundary diffusion are taken account into the mass transportation methods. The effect of surface profile has been studied. It is found that when the stress relaxation process is limited by surface diffusion, the ratio of surface energy over grain boundary, $\bar{\gamma} = \gamma_s / \gamma_{gb}$, plays a significant role in stress relaxation. Larger $\bar{\gamma}$ can slow down the stress relaxation process. The simulation results can be used to determine the diffusivity by being compared to experimental data. In the experiments by Gan *et al* [78], the stress relaxation process in thin film is limited by grain boundary diffusion. Using the experimental data and our simulation results, the activation energy and the pre-exponential factor of diffusivity of grain boundary diffusion in Cu and can be obtained. These two parameters are very sensitive to the slight change of experimental data while the final diffusivity $\delta_{gb} D_{gb}$ at certain temperature is relatively steady.

In the last section of our work, an axisymmetric version of the numerical approach has been developed, based on the three dimensional weak statement, to simulate the surface morphology evolution of a stressed fiber. Our simulation reproduces the Rayleigh instability and the critical wavelength λ_m at which the perturbation has maximum growth rate when the fiber is stress free. Consequently, for stressed fiber, the growth rate vs. wavelength under different stress levels is simulated. It is found that the stressed fiber may keep stable, develop grooves then approach to a steady state shape, or develop cusps and break into particles by surface diffusion. The two thresholds are roughly obtained (shown in Figure 5-6). The results might be used to make fibers with stable wavy surface.

Appendix

A. Weak Statement with Creep in the grains

For example, take a system of interfaces that move by diffusion on the interfaces and creep in the grains. The free energy consists of the external work and various interface tensions. The problem was first treated by Needleman and Rice [15]. Denote the virtual displacement field in the grains by δu_i, and the actual velocity field in the grains by v_i. Assume that the solid is incompressible, i.e.,

$$v_{i,i} = 0 \tag{A-1}$$

Define the stress tensor, σ_{ij}, and the diffusion driving force F_i on the same basis, namely, as the energy-conjugates of their respective kinematics quantities. Thus,

$$\int \sigma_{ij} \delta u_{i,j} \, dA + \int F_i \delta I_i dA = -\delta G \tag{A-2}$$

Interface diffusion obeys the kinetic law (2.26). For this demonstration, the grains deform according to a linear creep law:

$$\sigma_{ij} = \sigma_m \delta_{ij} + \eta(v_{i,j} + v_{j,i}) \tag{A-3}$$

Here, σ_m is the mean stress; η is the viscosity of the material; and $\delta_{ij} = 1$ when $i = j$, $\delta_{ij} = 0$ when $i \neq j$.

Replacing the diffusion driving force with the flux by equation (2.26) and the stress with the velocity gradient by equation (A-3), one can obtain

$$\int 2\eta v_{i,j}\delta u_{i,j}\, dA + \int \frac{J_i \delta I_i}{M} dA = -\delta G \qquad \textbf{(A-4)}$$

The actual velocity and flux satisfy this weak statement for arbitrary virtual motion.

B. Viscosity Matrix of Surface Element for 2-D Weak Statement

Recall the weak statement, equation (3.2). For one element (see Figure 3-5), the integral extends over one element, which becomes

$$\int_{-l/2}^{l/2}\left\{\frac{J\delta \mathrm{I}}{M}+\frac{\left(v_n+\partial J/\partial s\right)\left[\delta r_n+\partial\left(\delta \mathrm{I}\right)/\partial s\right]}{m}\right\}ds=-\delta G \qquad \textbf{(B-1)}$$

Substitute the virtual motion, δr_n, the actual velocity, v_n, the virtual mass displacement, $\delta \mathrm{I}$, and the mass flux, J, with the interpolation coefficients, equation (3.5), (3.8), (3.9) and (3.11), respectively. Each term in (B-1) then can be represented by the shape function and generalized coordinates. For the derivative of J with respective to s, since the shape function Q_i depends on the local coordinate, one can obtain

$$\partial J/\partial s=\frac{\partial Q_1}{\partial s}J_1+\frac{\partial Q_2}{\partial s}J_2+\frac{\partial Q_m}{\partial s}J_m \qquad \textbf{(B-2)}$$

Substitute shape function (3.10) into (B-2), giving

$$\frac{\partial J}{\partial s}=(\frac{4s}{l^2}-\frac{1}{l})J_1+(\frac{4s}{l^2}+\frac{1}{l})J_2-\frac{8s}{l^2}J_m \qquad \textbf{(B-3)}$$

Similarly, the derivative of $\delta \mathrm{I}$ with respective to s is

$$\frac{\partial(\delta \mathrm{I})}{\partial s}=(\frac{4s}{l^2}-\frac{1}{l})\delta \mathrm{I}_1+(\frac{4s}{l^2}+\frac{1}{l})\delta \mathrm{I}_2-\frac{8s}{l^2}\delta \mathrm{I}_m \qquad \textbf{(B-4)}$$

Integrate s over the element ($-l/2 \sim l/2$) for each term, giving the 7 x 7 symmetric matrix.

Let $C=\cos\theta$, $S=\sin\theta$. The components of the surface element viscosity matrix for 2-D elements, $\mathbf{H}^e$, is

$$\mathbf{H}^e = \frac{l}{6m} \times \begin{bmatrix} 2S^2 & -2SC & -5S/l & S^2 & -SC & S/l & 4S \\ -2SC & 2C^2 & 5C/l & -CS & C^2 & -C/l & -4C \\ -5S/l & 5C/l & 14/l^2+4W & -S/l & C/l & 2/l^2-W & -16/l^2+2W \\ S^2 & -CS & -S/l & 2S^2 & -2SC & 5S/l & -4S \\ -SC & C^2 & C/l & -2SC & 2C^2 & -5C/l & 4C \\ S/l & -C/l & 2/l^2-W & 5S/l & -5C/l & 14/l^2+4W & -16/l^2+2W \\ 4S & -4C & -16/l^2+2W & -4S & 4C & -16/l^2+2W & 32/l^2+16W \end{bmatrix} \quad \textbf{(B-5)}$$

where $W = \frac{m}{5M}$.

C. The Driving Force Components of Surface Element for 2-D Weak Statement

Recall the equation (3.4) and let the local coordinate s integrate over one element ($-l/2 \sim l/2$), giving, The force components acting on the two nodes due to the element surface tension and strain energy are

$$\delta G = \int_{-l/2}^{l/2} \gamma \delta(ds) + \int_{-l/2}^{l/2} w \delta r_n \, ds \qquad \textbf{(C-1)}$$

Assuming the strain energy density, w, is uniform in each element and taking the assumption of the isotropic of surface tension, γ, the free energy reduction associated with the virtual motion is

$$\delta G = \gamma \delta l + w \int_{-l/2}^{l/2} \delta r_n \, ds \qquad \textbf{(C-2)}$$

Replace δl and δr_n by equation (3.5) and (3.7), substitute shape function (3.6) into the equation and then integrate s over the element, giving the components of the driving force column

$$\begin{pmatrix} f_1 \\ f_2 \\ f_3 \\ f_4 \end{pmatrix} = \gamma_s \begin{pmatrix} \cos\theta \\ \sin\theta \\ -\cos\theta \\ -\sin\theta \end{pmatrix} + w \begin{pmatrix} -\sin\theta \\ \cos\theta \\ -\sin\theta \\ \cos\theta \end{pmatrix} \qquad \textbf{(C-3)}$$

D. Boundary Element Method (BEM) for 2-D Case

BEM is now well known for peoples, and there are many works to introduce and explain it [e.g. 100, 101]. Here it is outlined briefly.

Now start from the boundary integral formulation, and assume there is no initial stress (i.e. the stress caused by thermo-elastic) and body force,

$$u_l^i = \int_\Gamma u_{lk}^* p_k d\Gamma - \int_\Gamma p_{lk}^* u_k d\Gamma \qquad \textbf{(D-1)}$$

where Γ is the boundary of the domain, u_k the displacements on the boundary, p_k the tractions on the boundary, u_{lk}^* and p_{lk}^* the weight functions, which are the fundamental solutions of Navier's equations; and u_l^i are the displacements at any internal points and any *particular* point $'i'$ where the tractions or displacements are applied on the boundary. When $'i'$ is taken to the boundary, generally, the integrals have a singularity.

If the boundary is smooth at point $'i'$, it is easy to solve this problem and yields the following result

$$c_{lk}^i u_l^i = \int_\Gamma u_{lk}^* p_k d\Gamma - \int_\Gamma p_{lk}^* u_k d\Gamma \qquad \textbf{(D-2)}$$

where $c_{lk}^i = (1/2)\delta_{lk}$. When the point $'i'$ locates at the boundary which is not smooth, the results are different and difficult to obtain the general expression. Brebbia and Dominguez [100] gave the solution for elastostatic problem by using rigid body motions.

In order to solve the integral equation numerically, the boundary will be discretized into a series of elements over which displacements and tractions are written in terms of their values at a

series of nodal points. By using interpolation function Φ, the displacements and tractions can be express in terms of their each element's value as following

$$\mathbf{u} = \Phi \mathbf{u}^j \qquad \mathbf{p} = \Phi \mathbf{p}^j \tag{D-3}$$

where $\mathbf{u}^j$ and $\mathbf{p}^j$ are the element nodal displacements and tractions. Substituting this equation into equation (D-2), one can obtain

$$\mathbf{c}^i \mathbf{u}^i = \sum_{j=1}^{NE} \left\{ \int_{\Gamma_j} \mathbf{u}^* \mathbf{\Phi} \, d\Gamma \right\} \mathbf{p}^j - \sum_{j=1}^{NE} \left\{ \int_{\Gamma_j} \mathbf{p}^* \mathbf{\Phi} \, d\Gamma \right\} \mathbf{u}^j \tag{D-4}$$

NE here means number of elements, and Γ_j is the surface of a 'j' element. Now, adopting two matrixes

$$\begin{aligned} \mathbf{H}^{ij} &= \sum_t \int_{\Gamma_t} \mathbf{p}^* \mathbf{\Phi}_q \, d\Gamma + \mathbf{c}^i \delta_{ij} \\ \mathbf{G}^{ij} &= \sum_t \int_{\Gamma_t} \mathbf{u}^* \mathbf{\Phi}_q \, d\Gamma \end{aligned} \tag{D-5}$$

into equation (D-4), and then assembling all 'i' nodes into the global matrixes $\mathbf{H}$ and $\mathbf{G}$, then one can obtain the global system equations, i.e.

$$\mathbf{HU} = \mathbf{GP} \tag{D-6}$$

The vector $\mathbf{U}$ and $\mathbf{P}$ represent all the values of displacements and tractions before applying boundary conditions. By rearranging the two matrixes $\mathbf{H}$ and $\mathbf{G}$, passing all unknowns to a vector on the left hand side, and solving the equations, all the boundary values can be obtained.

E. Viscosity Matrix of Grain Boundary Element for 2-D Weak Statement

Recall the weak statement, equation (4.1). Consider only the grain boundary, for one element (see Figure 3-5), integral extends over one element, which becomes

$$\int_{-l/2}^{l/2} \left\{ \frac{J\delta \mathrm{I}}{M_{gb}} \right\} ds = -\delta G \qquad \textbf{(E-1)}$$

Substitute the virtual mass displacement, $\delta \mathrm{I}$, and the mass flux, J , with the interpolation coefficients, equation (3.9) and (3.11), respectively. Equation (E-1) becomes

$$\int_{-l/2}^{l/2} \left\{ \frac{\left(Q_1 J_1 + Q_m J_m + Q_2 J_2\right)\left(Q_1 \delta \mathrm{I}_1 + Q_m \delta I_m + Q_2 \delta I_2\right)}{M_{gb}} \right\} ds = -\delta G \qquad \textbf{(E-2)}$$

Replace Q_1 , Q_2 and Q_m by equation (3.10) and integrate the left hand side of equation (E-2), giving the components of the element viscosity matrix for grain boundary

$$H_{gb}^{e} = \frac{l}{30 M_{gb}} \times \begin{bmatrix} 4 & -1 & 2 \\ -1 & 4 & 2 \\ 2 & 2 & 16 \end{bmatrix} \qquad \textbf{(E-3)}$$

F. The components of Viscosity Matrix for axisymmetric elements

Denote $C = \cos\theta$, $S = \sin\theta$ and $m' = m\left(\frac{x_1 + x_2}{2}\right)^2$, giving the components of the element viscosity matrix

$$H_{11} = \frac{\pi l S^2 (10x_1^3 + 6x_1^2 x_2 + 3x_1 x_2^2 + x_2^3)}{30m'}$$

$$H_{12} = -\frac{\pi l C S (10x_1^3 + 6x_1^2 x_2 + 3x_1 x_2^2 + x_2^3)}{30m'}$$

$$H_{13} = -\frac{\pi S (4x_1 + x_2)(2Clx_1 + 7x_1^2 + 3x_1 x_2 + x_2^2)}{30m'}$$

$$H_{14} = \frac{\pi l S^2 (2x_1^3 + 3x_1^2 x_2 + 3x_1 x_2^2 + 2x_2^3)}{30m'}$$

$$H_{15} = -\frac{\pi l C S (2x_1^3 + 3x_1^2 x_2 + 3x_1 x_2^2 + 2x_2^3)}{30m'}$$

$$H_{16} = -\frac{\pi S (-Clx_1^2 + 4x_1^3 - 3x_1^2 x_2 + Clx_2^2 - 6x_1 x_2^2 - 5x_2^3)}{30m'}$$

$$H_{17} = -\frac{2\pi S (2Clx_1^2 - 8x_1^3 + 2Clx_1 x_2 - 3x_1^2 x_2 + Clx_2^2 + x_2^3)}{15m'}$$

$$H_{22} = \frac{\pi l C^2 (10x_1^3 + 6x_1^2 x_2 + 3x_1 x_2^2 + x_2^3)}{30m'}$$

$$H_{23} = -\frac{\pi C (4x_1 + x_2)(-2Clx_1 - 7x_1^2 - 2x_1 x_2 - x_2^2)}{30m'}$$

$$H_{24} = -\frac{\pi l C S (2x_1^3 + 3x_1^2 x_2 + 3x_1 x_2^2 + 2x_2^3)}{30m'}$$

$$H_{25} = \frac{\pi l C^2 (2x_1^3 + 3x_1^2 x_2 + 3x_1 x_2^2 + 2x_2^3)}{30m'}$$

$$H_{26} = \frac{\pi C(-Clx_1^2 + 4x_1^3 - 3x_1^2 x_2 + Clx_2^2 - 6x_1 x_2^2 - 5x_2^3)}{30m'}$$

$$H_{27} = \frac{2\pi C(2Clx_1^2 - 8x_1^3 + 2Clx_1 x_2 - 3x_1^2 x_2 + Clx_2^2 + x_2^3)}{15m'}$$

$$H_{33} = \frac{\pi l(7x_1 + x_2)}{30M}$$
$$+ \frac{\pi(7C^2 l^2 x_1 + 46Clx_1^2 + 79x_1^3 + C^2 l^2 x_2 + 12Clx_1 x_2 + 39x_1^2 x_2 + 2Clx_2^2 + 15x_x x_2^2 + 7x_2^3)}{30m'l}$$

$$H_{34} = -\frac{\pi S(Clx_1^2 + 5x_1^3 + 6x_1^2 x_2 - Clx_2^2 + 3x_1 x_2^2 - 4x_2^3)}{30m'}$$

$$H_{35} = \frac{\pi C(Clx_1^2 + 5x_1^3 + 6x_1^2 x_2 - Clx_2^2 + 3x_1 x_2^2 - 4x_2^3)}{30m'}$$

$$H_{36} = -\frac{\pi l(x_1 + x_2)}{30M} + \frac{\pi(x_1 + x_2)(-C^2 l^2 + 2Clx_1 + 13x_1^2 - 2Clx_2 - 16x_1 x_2 + 13x_2^2)}{30m'l}$$

$$H_{37} = \frac{2\pi l x_1}{15M} + \frac{2\pi(C^2 l^2 x_1 - 2Clx_1^2 - 23x_1^3 + 2Clx_1 x_2 - 9x_1^2 x_2 - 3x_x x_2^2 - 5x_2^3)}{15m'l}$$

$$H_{44} = \frac{\pi l S^2 (x_1^3 + 3x_1^2 x_2 + 6x_1 x_2^2 + 10x_2^3)}{30m'}$$

$$H_{45} = -\frac{\pi l CS(x_1^3 + 3x_1^2 x_2 + 6x_1 x_2^2 + 10x_2^3)}{30m'}$$

$$H_{46} = \frac{\pi S(x_1 + 4x_2)(x_1^2 - 2Clx_1 + 2x_1 x_2 + 7x_2^2)}{30m'}$$

$$H_{47} = -\frac{2\pi S(Clx_1^2 - x_1^3 + 2Clx_1 x_2 + 3x_1^2 x_2 + 2Clx_2^2 + 8x_2^3)}{15m'}$$

$$H_{55} = \frac{\pi l C^2 (x_1^3 + 3x_1^2 x_2 + 6x_1 x_2^2 + 10x_2^3)}{30m'}$$

$$H_{56} = -\frac{\pi C(x_1 + 4x_2)(x_1^2 - 2Clx_1 + 2x_1x_2 + 7x_2^2)}{30m'}$$

$$H_{57} = \frac{2\pi C(Clx_1^2 - x_1^3 + 2Clx_1x_2 + 3x_1x_2^2 + 2Clx_2^2 + 8x_2^3)}{15m'}$$

$$H_{66} = \frac{\pi l(x_1 + 7x_2)}{30M}$$
$$+ \frac{\pi(C^2l^2x_1 - 2Clx_1^2 + 7x_1^3 + 7C^2l^2x_2 - 12Clx_1x_2 + 15x_1^2x_2 - 46Clx_2^2 + 39x_xx_2^2 + 79x_2^3)}{30m'l}$$

$$H_{67} = \frac{2\pi lx_2}{15M} + \frac{2\pi(-5x_1^3 + C^2l^2x_2 - 2Clx_1x_2 - 3x_1^2x_2 + 2Clx_2^2 - 9x_xx_2^2 - 23x_2^3)}{15m'l}$$

$$H_{77} = \frac{8\pi l(x_1 + x_2)}{15M} + \frac{8\pi(x_1 + x_2)(C^2l^2 - 2Clx_1 + 7x_1^2 + 2Clx_2 - 4x_1x_2 + 7x_2^2)}{15m'l}$$

Bibliography

1. C. V. Thompson and J. R. Lloyd, "Electromigration and IC interconnects", *MRS Bull.*, (1993) 19-25
2. K. T. Miller and F. F. Lange, *Acta Metall.*, **37** (1989) 1343
3. M. R. Gungor, D. Maroudas, and S. J. Zhou, *Applied Physics Letters* **77** (2000) 343
4. A. J. Haslam, S. R. Phillpot, D. Wolf, D. Moldovan and H. Gleiter, *Mater. Sci. Eng. A*, 318 (2001) 293
5. S. Xiao and W. Hu, *Journal of Crystal Growth*, **286** (2006) 512
6. A. Roy, J. M. Rickman, J. D. Gunton and K. R. Elder, *Phy. Rev. E*, **57** (1998) 2610
7. M. T. Lusk, *Pro. R. Soc. Lond. A*, **455** (1999) 677
8. S. Y. Hu and L. Q. Chen, *Acta Mater.*, **49** (2001) 1879
9. D. J. Seol, S. Y. Hu, Y. L. Li, J. Shen, K. H. Oh and L. Q. Chen, *Metal and Materials International*, **9** (2003)
10. Y.W. Zhang, A.F. Bower, *Thin solid films* **257** (1999) 8.
11. Z. Suo, Motions of microstructural surfaces in materials, *Advances in applied mechanics* **33**, (1997) 193-294
12. A. C. F. Cocks, and S. P. A. Gill, *Advances in Applied Mechanics* **36**, (1999) 81-162
13. Herring, C., Surface tension as a motivation for sintering, The physics of powder metallurgy (W.D. Kingston Ed.) 143-179, McGraw-Hill, New York. 1951
14. B. Sun, Z. Suo and A. C. F. Cocks, *J. Mech. Phys. Solids*, **44** (1996) 559
15. A. Needleman and J. R. Rice, *Acta Metall.*, **28** (1980) 1315
16. A. C. F. Cocks and A. A. Searle, *Mech. Mater.*, **12** (1991) 279
17. A. C. F. Cocks and J. Pan, *Mech. Mater.*, **18** (1994) 269
18. A. C. F. Cocks and J. Pan, *Int. J. Fracture*, **60** (1993) 249
19. J. Pan and A. C. F. Cocks, *Int. J. Fracture*, **60** (1993) 121
20. J. Pan and A. C. F. Cocks, *Comp. Mater. Sci.*, **1** (1993) 95
21. P. Sofronis and R. M. McMeeking, *Mech. Mater.*, **18** (1994) 55
22. R. M. McMeeking, and L. T. Kuhn, *Mech. Mater.*, **40** (1992) 961
23. A. C. F. Cocks, *Acta Metall. Mater.*, **42** (1994) 2197

24. J. Svoboda and H. Riedel, *Acta Metall. Mater.*, **43**(1995) 1

25. A. F. Bower and L. B. Freund, Finite element analysis of electromigration and stress induced diffusion in deformable solids. Materials Reliability in Microelectronics V (ed. A. S. Oates, K. Gadepally, R. Rosenberg and W. F. Filter). Materials Research Society. 1995

26. J. Svoboda, and I. Turek, *Phil. Mag. B*, **64** (1991) 749

27. Z. Suo and W. Wang, *J. Appl. Phys.*, **76** (1994) 3410

28. B. Sun, Z. Suo and A. G. Evans, *J. Mech. Phys. Solids*, **42** (1994) 1653

29. Z. Suo, *Mater. Res. Sot. Symp. Proc.*, **338** (1994) 379

30. Z. Suo, *J. Mech. Phys. Solids*, **43** (1995) 829

31. R. E. Loge, and Z. Suo, *Acta Metall. Mater.*, **44** (1996) 3429

32. A. C. F. Cocks and S. P. A. Gill, *Acta Mater.*, **44** (1996) 4765

33. S. P. A. Gill and A. C. F. Cocks, *Acta Mater.*, **44** (1996) 4777

34. B. Sun, Z. Suo and W. Yang, *Acta Mater.*, **45** (1997) 1907.

35. B. Sun, Z. Suo, *Acta Mater.*, **45** (1997) 4953.

36. I. Prigogine, Introduction to Thermodynamics of Irreversible Processes. Wiley, New York, 1967.

37. T. Y. Tsui, A. J. McKerrow and J. J. Vlassak, *Journal of Mater. Res.*, **20**, 2266 (2005)

38. R. J. Asaro and W. A. Tiller, *Metall. Tran.*, **3** (1972) 1789

39. M. Grinfeld, Dokl. Akad. Nauk. SSSR, 290 (1986) 1358

40. D. J. Srolovitz, *Acta Metall*. **37** (1989) 621.

41. B. J. Spencer, P. W. Voorhees, S. H. Davis, *Phys. Rev. Lett.* **67** (1991) 3696.

42. H. J. Gao, *J. Mech. Phys. Solids*, **42** (1994) 741

43. L. B. Freund, *Int. J. Solids Structures* **32** (1995) 911.

44. R. V. Kukta and L.B. Freund, *J. Mech. Phys. Solids*, **45** (1997) 1835

45. J. Y. Yao, T. G. Anderson, G. L. Dunlop, *Applied Physics Letters* **53** (1988) 1420.

46. F. K. LeGoues, M. Copel, R. M. Tromp, *Phys Rev B* **42** (1990) 11690.

47. A. G. Cullis, D. J. Robbins, A. J. Pidduck, P.W. Smith, *J Cryst Growth* **123** (1992) 333.

48. C. H. Chiu, H. Gao, Inter. *J. solids structures* **30** (1993) 2983.

49. C. H. Chiu, H. Gao, *MRS Symp. Proc.*, **356** (1995) 33

50. C. Z. Ozkan, W.D. Nix, H. Gao, *J. Mater. Res.* **14** (1999) 3247.

51. W. H. Yang, D. J. Srolovitz, *J. Mech Phys Solids* **42** (1994) 1551.

52. D. E. Jesson, S. J. Pennycook, J. –M. Baribeau, D. C. Houghton, *Phys. Rev. Lett.*, **71** (1993) 1744

53. W. B. Hillig and R. J. Charles, Surface, stress-dependant surface reaction, and strength. In:

High strength materials. Wiley and Sons, NewYork, pp.682–703 1965

54. H. H. Yu, Z. Suo, *Acta Mater.*, **47** (1999) 77.
55. H. H. Yu, Z. Suo, *J. Appl. Phys.*, **87** (2000) 1211.
56. J. Liang, Z. Suo, *Interface Science*, **9** (2001) 93.
57. H. H. Yu, *Int. J. Solids and Structure*, **42** (2005) 3852
58. R. V. Kukta and D. Kouris, *J. Appl. Phys.*, **97** (2005) 033527
59. J. W. Hutchinson and Z. Suo, *Adv. Appl. Mech.* **29**(1992) 63
60. Th. Göbel, S. Menzela, M. Heckera, W. Brücknera, K. Wetziga and Ch. Genzelb, *Surface and Coatings Technology*, **142-144**(2001) 861
61. H. H. Yu, M. Y. He, and J. W. Hutchinson, *Acta Mater.*, **49**(2001) 93
62. Z. Suo, in *Comprehensive Structural Integrity*, edited by I. Milne, R. O. Ritchie, and B. Karihaloo, Vol. **8**: Interfacial and Nanoscale Failure (Elsevier, Amsterdam, 2003), pp. 265-324
63. L. Dong, J. Schnitker, R. W. Smith and D. J. Srolovitz, *J. of Applied Physics*, **83** (1998) 217
64. O. Kraft, L. B. Freund, R. Philips and E Arzt *MRS Bull*, **27** (2002) 30
65. D. Josell, T. P. Weihs and H. Gao *MRS Bull* **27**(2002) 39
66. R. M. Keller, S. P. Baker and E. Arzt *J. Matter. Res.*, **13** (1998) 1307
67. R. P. Vinci, E. M. Zielinski and J. C. Bravman,, *Thin Solid Flms*, **262** (1995) 142
68. M. D. Thouless, J. Gupta and J. M. E. Harper *J. Mater. Res.*, **8** (1993) 1845
69. Z. Liu and H. H. Yu, *Thin Solid Films*, **513**(2006) 391
70. J. H. Prevost, T. J. Baker, J. Liang, Z. Suo *Int. J. Solids Structures*, **38** (2001) 5185.
71. M. D. Thouless, *Acta Metall. Mater.*, **41** (1993) 1057
72. F. Y. Genin, W. W. Mullins and P. Wynblatt, *Acta Metall.Mater.*, **41** (1993) 3541
73. F. Y. Genin, *J. Appl. Phys.*, **77** (1995) 5130
74. F. Y. Genin, *Acta Metall.Mater.*, **43** (1995) 4289
75. H. Gao, L. Zhang, W. D. Nix, C. V. Thompson and E. Arzt, *Acta Mater.*, **47**(1999) 2865
76. L. Zhang and H. Gao, *Z. Metallkd.*, **93**(2002) 417
77. R. Huang, D. Gan and P.S. Ho, *J. of Appl. Phys.*, **97** (2005) 103532
78. D. Gan, P. S. Ho, R. Huang, J. Leu, J. Maiz and T. Scherban *J. of Appl. Phys.*, **97** (2005) 103531
79. M. J. Kobrinsky, C. V. Thompson and M. E. Gross, J. Appl. Phys., **89** (2001) 91
80. D. W. Gan, S. Yoon, P. S. Ho, P. Cresta, N. Singh, A. F. Bower, J. Leu and S. Shankar, *Proc. Int. Interconnect Technology Conference* (San Francisco, 2003)
81. Z. Liu and H. H. Yu, Stress relaxation of thin film due to coupled surface and grain-

boundary diffusion. Submitted.

82. W.W. Mullins, *J. Appl. Phys.* **28** (1957) 333.
83. F. A. Nichols and W. W. Mullins, *Trans. AIME* **233**, (1965) 1840
84. F. A. Nichols and W. W. Mullins, *Journal of Applied Physics*, **36**, (1965) 1826
85. T. K. Gupta, in *Advances in Ceramics*, Vol. 10, ed. W. D. Kingery. The American Ceramic Society, Columbus, OH, 1984, pp. 750-766.
86. J. D. Powers and A. M. Glaeser, *J. Am. Gram. SM.*, **76**, (1993) 225
87. J. D. Powers and A. M. Glaeser, *Journal of the American Ceramic Society*, **75**, (1992) 2547
88. S. A. Hackney, *Scripta Metallurgica*, **25**, (1991) 799
89. C. L. Briant, *Metallurgical and Materials Transactions A*, **24**, (1993) 1073
90. J. H. Choy, S. A. Hackney and J. K. Lee, *Journal of Applied Physics*, **77**, (1995) 5647
91. H. H. Yu and Z. Suo, *Journal of Mechanics and Physics of Solids*, **47**, (1999) 1131
92. J. Colin, J. Grilhe and N. Junqua, *Acta Mater*, **45**, (1997) 3835
93. J. Colin, J. Grilhe and N. Junqua, *Europhysics Letters*, **38**, (1997) 307
94. D. J. Kirill, S. H. Divis, M. J. Miksis and P. W. Voorhees, *Proceedings of the Royal Society A*, **455**, (1999) 3825
95. J. Colin, *Acta Mater*, **52**, (2004) 4985
96. Z. Liu and H. H. Yu, Evolution of Stressed Fiber due to Surface Diffusion. In Progress
97. D. Turnbull, *Solid State Physics*, 3(1956) 225
98. W. W. Mullins, *J. Appl. Phys*., 27(1956) 900
99. M. A. Biot, "Variational Principles in Heat Transfer." Oxford Univ. Press, Oxford
100. C. A. Brebbia, J. Dominguez, Boundary Elements: An Introductory Course, Computational Mechanics Publications, McGraw-Hill, New York NY, 1989
101. F. Hartmann, Introduction to Boundary Elements: Theory and Applications, Springer-Verlag, New York NY, 1989.
102. H. Tada, P. C. Paris, G. R. Irwin, The Stress Analysis of Cracks, Handbook (2nd Edition), Paris Productions, Inc., St. Louis, 1985.
103. J. Horvath, R. Birringer and H. Gleiter, *Sol. Stat. Commun*., **62**(1987) 319
104. W. Dickenscheid, R. Birringer, H. Gleiter, O. Kanert, B. Michel and B. Gunther, *Sol. Stat. Commun*., **79**(1991) 683
105. C. W. Park and R. W. Vook, *Appl. Phys. Lett.*, **59**(1991) 175
106. T. Nitta, T. Ohhmi, M. Otsuki, T. Takewaki and T. Shibata, *J. Electrochem. Soc.*, **139**(1992) 922
107. C. W. Park and R. W. Vook, *Thin Solid Films*, **226**(1993) 238
108. K. L. Lee, C.K. Hu and K.N. Tu, *J. Appl. Phys.*, **78**(1995) 4428
109. R. Frankovic and G.H. Bernstein, *IEEE Trans. Electron Devices*, **43**(1996) 2233
110. D. Gupta, C.K. Hu and K.L. Lee, *Deffect Diffus. Forum*, **143-147**(1997) 1397

111.T. Surholt and C. Herzig, *Acta Mater.*, **45**(1997) 3817

112.D. Save, F. Braud, J. Torres, F. Binder, C. Muller, J.Q. Weidnert and W. Hasse, *Microelectron. Eng.*, **33**(1997) 75

113.A. Gladkikh, M. Karpovski, A. Palevski and Y.S. Kaganovskii, *J. Phys. D: Appl. Phys.*, **31**(1998)1626

114.B. Cai, Q. P. Kong, L. Lu and K. Lu, *Scripta Materialia*, **41**(1999) 755

115.S. K. Donthu, M. M. Vora, S. K. Lahiri, C. V. Thompson and S. Yi, *J. of Electron. Materials*, **32**(2003) 531

116.C. K. Hu, R. Rosenberg and K.Y. Lee, *Appl. Phys. Lett.*, **74**(1999) 2945

117.C. K. Hu, L. Gignac, R. Rosenberg, E. Liniger, J. Rubino, C. Sambucetti, A. Stamper, A. Domenicucci and X. Chen, *Microelectronic Engineering*, **70**(2003) 406

118.C. K. Hu, L. M. Gignac, E. Liniger and C. Detavernier, *Journal of Applied Physcis*, **98**(2005) 124501

119.J. C. Lin, S. K. Park, K. Pfeifer, R. Auger, V. Blaschke, S.L. Shue and M.S. Liang, *Proceedings of Advanced Metallization Conference 2002*, AMC XVIII (Materials Research Society, Warrendale, PA, 2003) 233

120.S. Demuynck, Z. S.Tokei, C. Bruynseraede, J. Michelon and K. Max, *Proceedings of Advanced Metallization Conference 2003*, AMC XIX (Materials Research Society, Warrendale, PA, 2004) 35

121.Lord Rayleigh, "On the Instability of Jets", *Proceedings of the London Mathematical Society*, **10**, (1878) 4

122.J. M. Heintz, O. Sudre and F. F. Lange, *J. Am. Ceram. Soc.*, **77** (1994) 787

123.O. Sudre and F. F. Lange, *J. Am. Ceram. Soc.*, **75** (1992) 3241

124.http://cms.mse.berkeley.edu/research/rayleigh.htm